



**This electronic thesis or dissertation has been
downloaded from Explore Bristol Research,
<http://research-information.bristol.ac.uk>**

Author:

Nantanoi, Sirawitch

Title:

The Reservoir Characterisation and Fault Investigation of the Bowland Shale Formation: The Applications of Seismic Attributes and Inversion to Identify Reactivated Faults and Sweet Spots

General rights

Access to the thesis is subject to the Creative Commons Attribution - NonCommercial-No Derivatives 4.0 International Public License. A copy of this may be found at <https://creativecommons.org/licenses/by-nc-nd/4.0/legalcode> This license sets out your rights and the restrictions that apply to your access to the thesis so it is important you read this before proceeding.

Take down policy

Some pages of this thesis may have been removed for copyright restrictions prior to having it been deposited in Explore Bristol Research. However, if you have discovered material within the thesis that you consider to be unlawful e.g. breaches of copyright (either yours or that of a third party) or any other law, including but not limited to those relating to patent, trademark, confidentiality, data protection, obscenity, defamation, libel, then please contact collections-metadata@bristol.ac.uk and include the following information in your message:

- Your contact details
- Bibliographic details for the item, including a URL
- An outline nature of the complaint

Your claim will be investigated and, where appropriate, the item in question will be removed from public view as soon as possible.



**The Reservoir Characterisation and Fault Investigation of the Bowland Shale
Formation: The Applications of Seismic Attributes and Inversion to Identify
Reactivated Faults and Sweet Spots**

Sirawitch Nantanoi

A dissertation submitted to the University of Bristol in accordance with the requirements of the
degree of master by research in the Faculty of Science.

School of Earth Sciences

July 2021

Word count: 23,456

Abstract

Unconventional explorations of gas-bearing shales have become an important resource as conventional gas fields have declined. The Bowland Shale Formation is among the most promising unconventional resources in the UK, with its high organic content and brittleness. However, the recent hydraulic fracturing of the Bowland Shale generated problematic felt seismicity. The first objective of this study is to examine the faults that caused felt seismicity at the Preston New Road (PNR) site in 2018 and 2019 using seismic attributes. The second goal is to identify sweet spots, the most promising drilling targets, in the Bowland Shale using seismic inversion.

Firstly, I investigated whether the faults responsible for the induced seismicity could be seen in the reflection seismic data acquired from Lancashire, UK. While many faults were visible on the 3D seismic data, the responsible faults were not. I compound seismic attributes, revealing potential evidence of the causative faults. Nonetheless, these observations were ambiguous since any anomalies were not significantly above background noise levels. This might be because they are subtle strike-slip faults, according to the recorded focal mechanisms, which do not cause vertical offsets. Secondly, I characterised the spatial variability of physical properties within the Bowland Shale. Statistical analysis of well logs from two wells indicates that vertical variations are dominated by changes in the natural gamma ray log. I applied a seismic inversion algorithm to the 3D seismic data, yielding Acoustic Impedance (AI), Shear Impedance (SI), and $\lambda\rho$ and $\mu\rho$ volumes. Sweet spots are indicated by low $\lambda\rho$ and $\mu\rho$ values. Many sweet spots identified by our analysis have already been targeted by existing wells, except spots between the Preese Hall-1 (PH-1) and Preston New Road (PNR) and between PH-1 and Thistleton-1 (TH-1) wells. These areas have more ductile shale content, which might be promising prospective locations in the

future since they are less likely to generate induced seismicity, but may still have potential for high production.

Acknowledgements

I would like to thank the University of Bristol and Dr. James Verdon for giving me the opportunity to come to this country and work on this project. Working on this project really puts me out of my comfort zone and makes me challenges myself, which is a good thing as it helps me grow and learn to adapt to unexpected circumstances. I really appreciate your valuable supports, which guide me to overcome obstacles and finally finish the project. As an international student, I am sure that you must have put more time and efforts to understand or revise my reports due to language mistakes. Thus, I thank you very much for everything you have done for me.

I also would like to thank my fellow G10a office mates for various recommendations, which help me adapt to the new environment quickly. Special thanks to Joao, German, and Tan for the suggestions and discussion on the topics I was not familiar with. I could not finish this project this quick without you guys. Thanks to all of my friends and Thai communities in Hodgkin House and Giggling Squid for being so kind to me. With your hospitality and generosity, I feel right at home throughout my stay in Bristol. Thanks to Nim for all the encouragement you gave me especially during the lockdown. I sincerely hope that everything works out well for you, too.

Finally, I could not make it this far without the supports of my family. I would like to thank them for the never-ending supports I received throughout my whole life. Without the push from my parents, I would not have made it outside of the country in the first place. I truly am glad that I went abroad, and it is you who gave me this experience. I hope I have made you proud.

Author's Declaration

I declare that the work in this dissertation was carried out in accordance with the requirements of the University's *Regulations and Code of Practice for Research Degree Programmes* and that it has not been submitted for any other academic award. Except where indicated by specific reference in the text, the work is the candidate's own work. Work done in collaboration with, or with the assistance of, others, is indicated as such. Any views expressed in the dissertation are those of the author.

SIGNED: DATE:.....

Table of Contents

Abstract.....	1
Acknowledgement.....	3
Author’s declaration.....	4
Table of contents.....	5
List of figures.....	9
Chapter 1: General introduction.....	15
1.1 Thesis description and goals.....	15
1.2 Structure of the thesis.....	16
Chapter 2: Background Information.....	18
2.1 Shale and unconventional shale for exploration.....	18
2.2 Global shale gas development.....	20
2.2.1 The beginning of unconventional shale gas exploration.....	20
2.2.2 Global shale gas exploration.....	22
2.2.3 Unconventional exploration in the UK.....	24
2.3 Hydraulic fracturing.....	24
2.4 Sweet spots.....	26
2.4.1 TOC.....	26

2.4.2 Brittleness.....	27
2.4.3 Young’s modulus and Poisson’s ratio.....	27
2.4.4 $\lambda\rho$ and $\mu\rho$	28
2.5 Geographical settings of the Bowland Shale.....	30
2.6 Stratigraphy.....	34
2.7 Bowland Shale Formation.....	36
2.7.1 Lower Bowland Shale Formation.....	36
2.7.2 Upper Bowland Shale Formation.....	37
2.8 Induced seismicity.....	38
2.9 Hydraulic fracturing in Bowland Shale.....	40
2.9.1 The first case of felt seismicity in Bowland Shale.....	40
2.9.2 Felt seismicity in Bowland Shale in 2018-2019.....	42
2.10 Application of seismic attributes on fault investigation at the PNR site.....	43
2.10.1 Similarity.....	44
2.10.2 Curvature.....	44
2.10.3 Spectral decomposition.....	45
Chapter 3: Seismic data.....	47
3.1 3D reflection seismic data.....	47

3.2 Investigation of the reactivated faults during the hydraulic fracturing at the PNR site.....	50
3.3 PH-1 and PNR-1 Well logs.....	53
Chapter 4: Seismic interpretation.....	58
4.1 Fault investigation method.....	58
4.2 The key horizons tracking.....	59
4.3 Fault mapping results and observations.....	65
4.4 Regional seismic interpretation.....	69
Chapter 5: The reactivated fault investigation using the seismic attributes.....	76
5.1 The results and observations of the fault investigation using the seismic attributes	76
5.1.1 Similarity.....	76
5.1.2 Spectral decomposition.....	84
5.1.3 Curvature.....	93
5.2 The comparison between the fault investigation using the seismic attributes and the investigation using only the 3D seismic data.....	98
5.3 Discussion.....	100
Chapter 6: Well log analysis.....	103
6.1 PCC and PCA of PH-1 and PNR-1 wells.....	103

6.2 Cross-plot analysis of PH-1 and PNR-1 well logs.....	111
6.3 Well log analysis conclusions.....	120
Chapter 7: Seismic inversion and sweet-spot identification of the Bowland Shale Formation.....	121
7.1 Seismic inversion of Bowland Shale Formation.....	121
7.2 Seismic inversion results.....	124
7.3 Cross-plot analysis and sweet-spot identification.....	128
7.4 Conclusions	137
Chapter 8: Discussion.....	138
Chapter 9: Conclusions.....	141
References.....	145

List of Figures

Figure 2-1: Outcrop of shale and calcareous mudstone of the Bowland Shale Formation, UK.....	19
Figure 2-2: Major unconventional plays in the US and the number of wells that have been drilled, and might be drilled in the future, in each of these plays.....	20
Figure 2-3: locations of major unconventional oil and gas exploration worldwide and estimated technically recoverable reserves.	22
Figure 2-4: Shale gas production by play in the US from 2007 to 2018.....	23
Figure 2-5: Basic hydraulic fracturing process utilizing horizon well drilling.....	25
Figure 2-6: Trends in the $\lambda\rho - \mu\rho$ cross-plot	29
Figure 2-7: The location of the Bowland Shale in the central UK.....	31
Figure 2-8: Geographical settings and structures of the study area and surroundings.....	33
Figure 2-9: Stratigraphy of the Bowland Basin.	35
Figure 2-10: The location of the PNR wells.	43
Figure 2-11: Explanations of the curvature values.....	45
Figure 3-1: The geographical position of the 3D reflection seismic survey in the central UK.....	49
Figure 3-2: Identification of the reactivated fault at the PNR-1z well.....	52

Figure 3-3: Identification of the reactivated fault at the PNR-2 well.....	53
Figure 3-4: PH-1 well logs.....	55
Figure 3-5: PH-1 well logs (only for the Bowland Shale Formation)	56
Figure 3-6: PNR-1 well logs.....	57
Figure 4-1: The fault tracking process.....	59
Figure 4-2: Well-to-seismic calibration.	61
Figure 4-3: The wavelet used to create the synthetic data in well-to-seismic calibration.....	61
Figure 4-4: Process of tracking horizons.	62
Figure 4-5: Key horizons that were picked in this study.	63
Figure 4-6: An example of the “complete a four” technique for verifying the picking of the Manchester Marl horizon.....	64
Figure 4-7: The locations of the faults tracked in this study in map-view (time slice at 1,340 ms or 2.54 km depth).....	66
Figure 4-8: polar histogram (rose-diagram) of strike directions of the picked faults in azimuthal system.....	68
Figure 4-9: 3D reflection seismic data in map-view in OpendTect program.....	70
Figure 4-10: cross-section of the 3D reflection seismic data from PH-1 well to PNR-1z well.....	71

Figure 4-11: cross-section of the 3D reflection seismic data from PH-1 well to TH-1 well.....	72
Figure 4-12: cross-section of the 3D reflection seismic data from PNR-1z well to TH-1 well.....	73
Figure 4-13: cross-section of the 3D reflection seismic data across PNR-1z well in the E-W direction.....	74
Figure 4-14: The causative faults in the 3D seismic data.....	75
Figure 5-1: Similarity attribute applied on the time slice at 1,270 ms.....	77
Figure 5-2: Similarity attribute applied on the time slice at 1,260 ms.....	78
Figure 5-3: Similarity attribute applied on the time slice at 1,180 ms.....	79
Figure 5-4: Additional horizons picked near the PNR-1z and PNR-2 events.....	81
Figure 5-5: Similarity attribute applied on the picked horizon near PNR-1z events.....	82
Figure 5-6: Similarity attribute applied on the picked horizon near PNR-2 events.....	83
Figure 5-7: RGB colour-blended spectral decomposition attributes on picked horizons near PNR-1z events.....	85
Figure 5-8: RGB color-blended spectral decomposition attributes on picked horizons near PNR-2 events.....	86

Figure 5-9: High-frequency (70 Hz) spectral decomposition attributes on picked horizons near PNR-1z events.....	88
Figure 5-10: Zoomed-in high-frequency (70 Hz) spectral decomposition attributes on picked horizons near PNR-1z events.....	89
Figure 5-11: The identified fault is picked and tracked.....	90
Figure 5-12: High-frequency (50 Hz) spectral decomposition attributes on picked horizons near PNR-2 events.....	91
Figure 5-13: Zoomed-in high-frequency (50 Hz) spectral decomposition attributes on picked horizons near PNR-2 events.....	92
Figure 5-14: Most-positive curvature attribute applied on the picked horizon near the PNR-1z events.....	94
Figure 5-15: Most-positive curvature attribute applied on the picked horizon near the PNR-1z events.....	95
Figure 5-16: Most-negative curvature attribute applied on the picked horizon near the PNR-1z events.....	96
Figure 5-17: Most-negative curvature attribute applied on the picked horizon near the PNR-1z events.....	97
Figure 5-18: The efficiency of the fault investigation using the seismic attributes, compared to the investigation using only the 3D seismic data.....	99
Figure 6-1: PH-1 well logs and PCA score logs.....	107

Figure 6-2: PH-1 well logs and PCA score logs (only for the Bowland Shale Formation).....	108
Figure 6-3: PNR-1 well logs and PCA score logs.....	109
Figure 6-4: The cross-plot analysis between DTS and DT from the PH-1 well logs.....	113
Figure 6-5: The cross-plot analysis of the well log data from PH-1 well within the Bowland Shale Formation range.....	114
Figure 6-6: $\lambda\rho - \mu\rho$ cross-plot of well log data from the PH-1.....	117
Figure 6-7: $\lambda\rho - \mu\rho$ cross-plot of well log data from the PNR-1 well.....	118
Figure 6-8: $\lambda\rho - \mu\rho$ cross-plot of PH-1 well log data of the Bowland Shale in comparison with the West Canadian shale play and the Barnett Shale of the US.....	119
Figure 7-1: The detailed model-based seismic inversion workflow.....	122
Figure 7-2: The comparison of the real and synthetic seismic data.....	123
Figure 7-3: The zero-phased wavelet used for the seismic inversion process.....	124
Figure 7-4: The AI, SI, $\lambda\rho$, and $\mu\rho$ volumes from the seismic inversion applied on the top of the Upper Bowland Shale Formation.....	125
Figure 7-5: The AI, SI, $\lambda\rho$, and $\mu\rho$ volumes from the seismic inversion applied on the top of the Lower Bowland Shale Formation.....	126
Figure 7-6: The AI and SI volumes applied on a vertical slice with PH-1 well logs.....	127

Figure 7-7: The $\lambda\rho - \mu\rho$ cross-plot of the top of the Upper and Lower Bowland Shale Formations..... **130**

Figure 7-8: The classified first group of the data from the Upper Bowland Shale Formation projected on the top of the Upper Bowland Shale horizon.....**131**

Figure 7-9: The second group of the data from the Upper Bowland Shale Formation projected on the top of the Upper Bowland Shale horizon.....**132**

Figure 7-10: The third group of the data from the Upper Bowland Shale Formation projected on the top of the Upper Bowland Shale horizon.....**133**

Figure 7-11: The first group of the data from the Lower Bowland Shale Formation projected on the top of the Lower Bowland Shale horizon..... **134**

Figure 7-12: The second group of the data from the Lower Bowland Shale Formation projected on the top of the Lower Bowland Shale horizon..... **135**

Figure 7-13: The third group of the data from the Lower Bowland Shale Formation projected on the top of the Lower Bowland Shale horizon..... **136**

Chapter 1: General Introduction

1.1 Thesis Description and Goals

The 3D reflection seismic data analysis plays a significant role in unconventional explorations because it can provide geological details which can be beneficial for not only the production, but also the risk assessments (Anderson et al., 2020). In this thesis, I study the 3D reflection seismic data of the Bowland Shale, which is located in Lancashire, central UK. The main objectives of this thesis are investigating the faults that caused felt seismicity near the Preston New Road (PNR) site and identifying sweet spots, or the most productive drilling locations. The first goal has been achieved by investigating the 3D reflection seismic data by applying seismic attributes to detect potential faults near the PNR drilling site. I have applied seismic attributes including similarity, curvature and spectral decomposition to the seismic volume since they are commonly used in fault investigations. This is to assess whether or not reactivated faults at the PNR site can be detected in advance in 3D reflection seismic data. If it is possible to detect these faults before the operation, the risks of induced seismicity can be substantially minimized or avoided. For example, the fault locations can be used with the stress field data to calculate the fault slip potential of each fault detected on the seismic data (Walsh et al., 2017). However, the fault slip potential calculation is beyond the scope of this thesis. As a result, this would benefit the unconventional exploration of the Bowland Shale as it would improve operation plans and reduce the cost (Anderson et al., 2020).

In order to optimize extraction, choices of drilling locations are a key factor. Areas that have good conditions for hydrocarbon productivity are defined as “sweet spots” as they have high Total Organic Content (TOC), brittleness, and porosity. These sweet spots can be identified

by analysing reflection seismic data and well logs to calculate elastic moduli, which can directly indicate physical properties of rock formations (Alzate & Devegowda, 2013). To achieve this second objective, seismic inversion has been performed in order to obtain the elastic moduli necessary for assessing TOC and brittleness of Bowland Shale. Then, the data have been cross-plotted to classify localities based on their productivity and brittleness according to the $\lambda\rho - \mu\rho$ cross-plot by Goodway et al. (2010). This allows us to detect sweet spots on the picked horizons, or even spots with high TOC but less brittle to avoid felt seismicity. The result from this study would improve the exploration of the Bowland Shale since it can reveal suitable targeting spots in the Bowland Shale itself with fewer chances for triggering induced seismicity. Additionally, the location of the PNR wells was decided based on only the geological and structural conditions of the region, and the ground condition to minimise the chances of triggering felt seismicity (Cuadrilla Bowland Ltd, 2014). By not taking the brittleness of the targeting spots into the consideration, the chance for the hydraulic fracturing at the PNR wells to produce felt seismicity might be higher than at other spots.

1.2 Structure of the Thesis

In this thesis, Chapter 2 discusses the background information regarding the unconventional explorations, Bowland Shale, hydraulic fracturing in the Bowland Shale, and the seismic attributes used in this study. Chapter 3 contains the information about the 3D seismic data and well data, which are fundamental for the seismic interpretation, fault investigation, and seismic inversion. In Chapter 4, the results of the seismic interpretation and fault investigation in the Bowland Shale are shown and discussed. Chapter 5 contains the investigation of the reactivated faults at the PNR site by using the seismic attributes. Chapter 6 analyses the data from well logs, which can provide insight about general physical properties and their statistical

relationships of the formations in the study area. Chapter 7 contains a seismic inversion, including the results of the inversion of the 3D reflection seismic data of the Bowland Shale. It also explains the application of the data acquired from the inversion for identifying sweet spots in the Bowland Shale. Chapter 8 contains a discussion of every discovery in this thesis. Finally, Chapter 9 is the overall conclusion of this thesis.

Chapter 2: Background Information

2.1 Shale and Unconventional Shale for Exploration

Shale is one of the most common types of sedimentary rock found on Earth. Shale is a fine-grained siliciclastic (silica-bearing) sedimentary rock composed of mostly clay-size particles ($< 3.9 \mu\text{m}$, Wentworth, 1922) that have been compacted and lithified. The main mineral components of shale include quartz, clay minerals, carbonate, organic matters, mica, and feldspar. Shale is typically red, brown, grey, or dark grey in colour depending on mineral composition and the nature of weathering (Figure 2-1). Shale is deposited in marine systems with low energy, where small-sized particles cannot be transported further and begin to settle down and deposit due to the low-energy environment. Shales are commonly laminated with alternation of lighter and darker bands, typically controlled by oxygen levels and the amount of organic matter in the rock. Shales of interest in hydrocarbon prospecting usually have dark colour due to the high proportion of organic content in the matrix as a result of deposition in anoxic environments.



Figure 2-1: Outcrop of shale and calcareous mudstone of the Bowland Shale Formation. From Shale Gas by BGS Research, n.d. (<https://www.bgs.ac.uk/geology-projects/shale-gas/>).

Dark shale rocks with high organic content are very important in conventional oil and gas exploration as the source rocks. When an organic rich shale rock is buried to sufficient temperatures and pressures, the organic material is converted into oil and gas, which then migrates out from the source and accumulates in a reservoir with higher porosity.

Shale plays an even more significant role in an unconventional hydrocarbon exploration. Shale rocks have extremely low permeabilities. Because of this, the much of oil and gas generated during the maturation remained trapped inside the shale formation and does not migrate out. Thus, a shale rock in unconventional explorations is considered both the source rock and the reservoir.

2.2 Global Shale Gas Development

2.2.1 The Beginning of Unconventional Shale Gas Exploration

The history of unconventional shale gas development started from the 1930s, when Wilson (1934) classified an unconventional deposit as one of his petroleum deposit classification genres (Zou, 2013). However, it was not considered to be commercially exploitable at that time because of its poor reservoir quality. In the 1990s, unconventional exploration gathered more attention due to the improvement of geological and engineering technologies, allowing extraction from unconventional resources to become possible. This has sparked the study of unconventional deposits as a new energy resource.

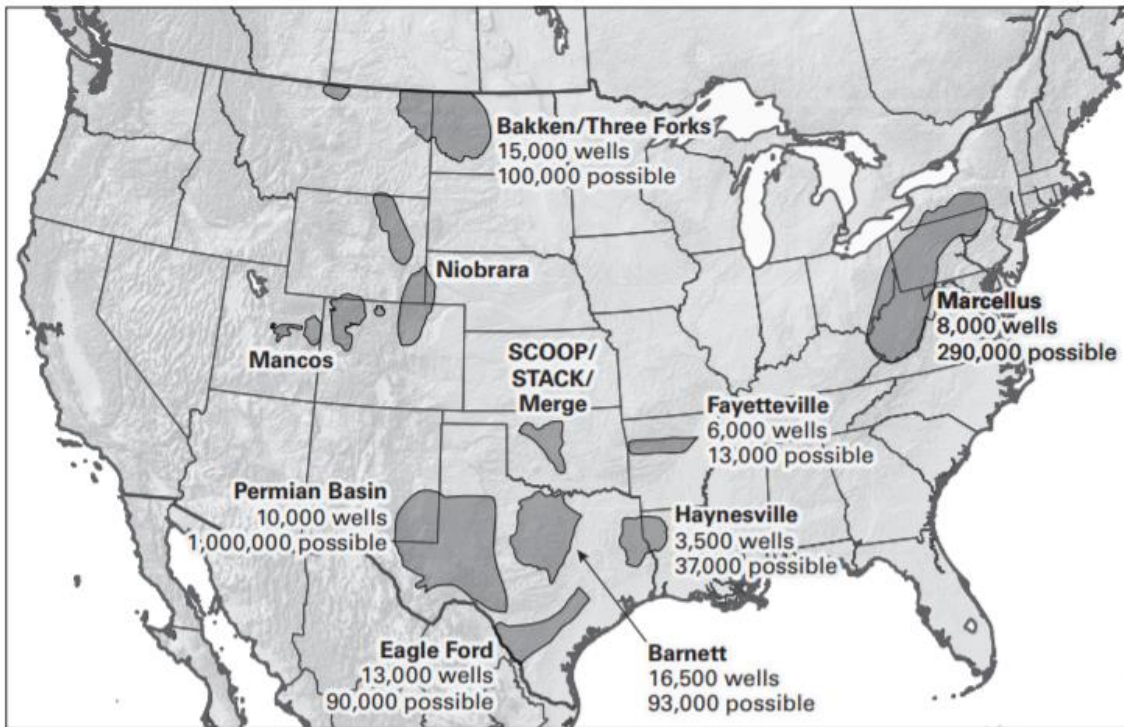


Figure 2-2: Major unconventional plays in the US and the number of wells that have been drilled, and might be drilled in the future, in each of these plays. From “Introduction

*in Unconventional Reservoir Geomechanics: Shale Gas, Tight Oil, and Induced Seismicity” by
Zoback, M., and Kohli, A, 2019, Cambridge University Press, p.8.*

As conventional hydrocarbon exploration starts to decline, unconventional shale gas exploration is thought to be a promising alternative source of hydrocarbons. The development of horizontal drilling techniques, when combined with hydraulic fracturing, allows shale gas exploitation to become commercially viable. The first applications of hydraulic fracturing were in conventional reservoirs in the late 1940s in Texas and Oklahoma, US (Montgomery & Smith, 2010; Zendehboudi & Bahadori, 2016). However, the technique was not applied commercially to shale formations until the 1990s. The Barnett Shale formation in Texas represents the first successful exploitation of unconventional gas resources. It encouraged other explorations of unconventional resources in the US such as the Bakken, Marcellus, and the Texas Permian Basin (Figure 2-2). In 2010, approximately 85% of the energy consumed in the US came from natural gas, oil, and coal. Of this, 22% came from natural gas, and this level of supply is predicted to remain stable for the next 20 years (Nash, 2010).

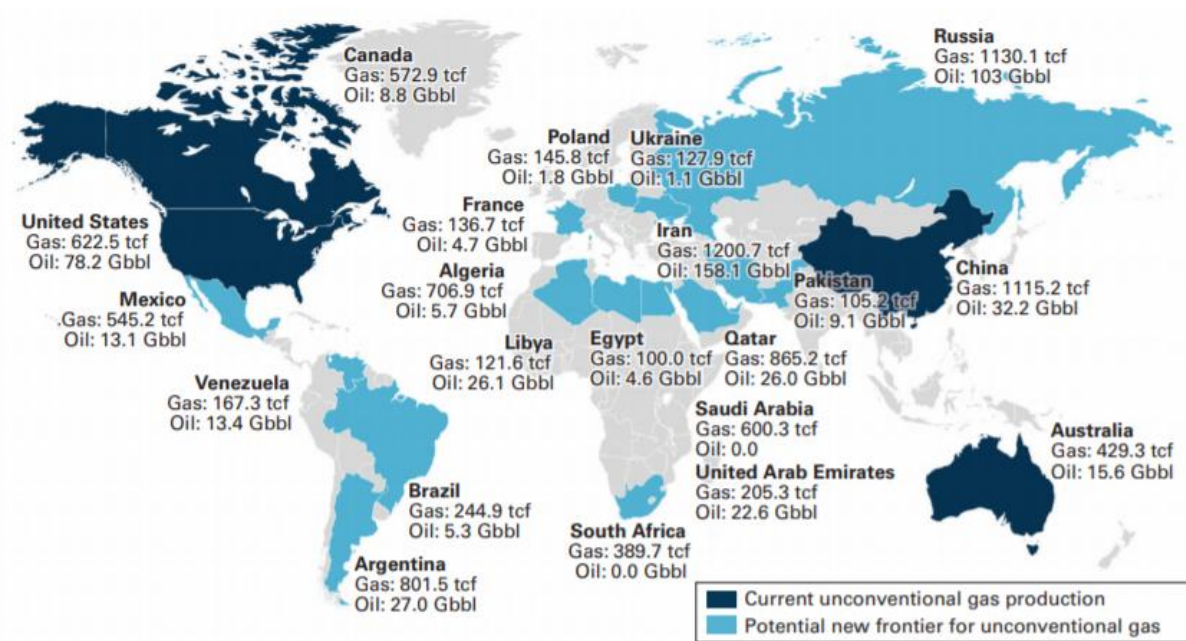


Figure 2-3: locations of major unconventional oil and gas exploration worldwide and estimated technically recoverable reserves. From “Introduction in Unconventional Reservoir Geomechanics: Shale Gas, Tight Oil, and Induced Seismicity” by Zoback, M., and Kohli, A, 2019, Cambridge University Press, p.9.

2.2.2 Global Shale Gas exploration

The success of unconventional shale explorations in Northern America has catalysed shale gas explorations around the world. Figure 2-3 shows locations of unconventional oil and gas exploration worldwide and their estimated technically recoverable reserves. The biggest plays are in China and North America, and there are many large potential unconventional reservoirs elsewhere such as Russia, Iran, and Argentina (Zoback et al., 2019). The United States Geological Survey (USGS) and the Department of Energy (DOE) of the US have estimated the total global recoverable resources from unconventional sources to be roughly equal to those from

conventional oil and gas (Zou, 2013). The estimated total volume of natural gas from unconventional sources around the world is $3,922 \times 10^{12} \text{ m}^3$, which is considered 8.3 times the total gas from conventional sources (including gas hydrate, shale gas, coalbed methane (CBM), and tight-sandstone gas) (Zou, 2013).

The growth of unconventional exploitations has been significant. Figure 2-4 illustrates total production of unconventional gas in the US overtime. The unconventional gas production in the US has increased approximately 5-fold from 2007 to 2017.

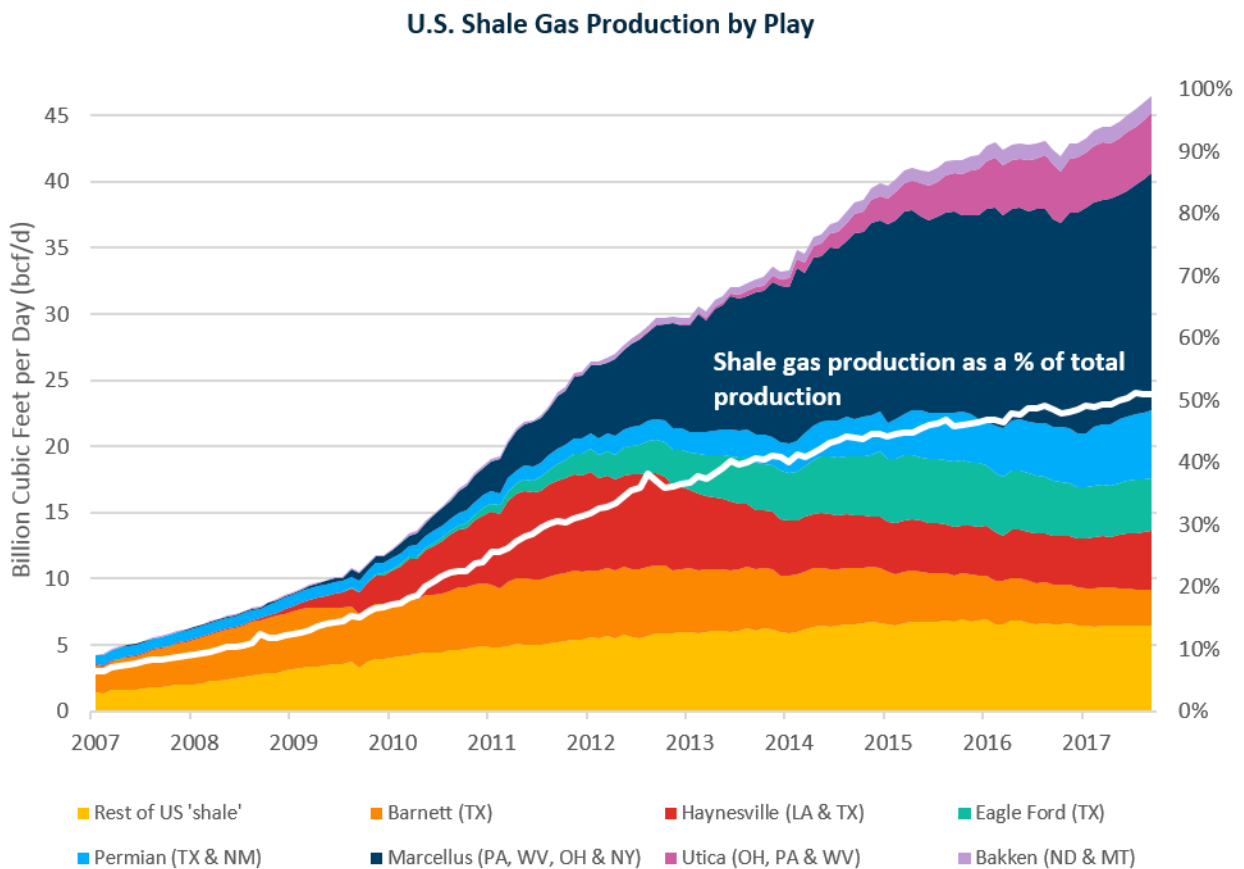


Figure 2-4: Shale gas production by play in the US from 2007 to 2018. From “U.S. Natural Gas in the Global Economy” by Ladislav et al., 2017, Center for Strategic and International Studies,

2.2.3 The Unconventional Exploration in the UK

In the UK, exploration of unconventional resources is still in its early stages. By analogy with the USA, Selley et al. (2005) argued that the UK has the potential for significant shale gas resources with shale formations identified in northern England, southern England, and Scotland (Selley et al., 2005, Smith et al., 2010). Among the Carboniferous shales, the Bowland Shale (or Bowland-Hodder Shale) is considered one of the most promising gas-bearing shales due to its high total organic content (TOC), high brittleness, and optimal maturity (Smith et al., 2010). It has been estimated by British Geological Survey (BGS) that the potential resource yield is 822 – 1,329 – 2,281 trillion cubic feet (tcf) (23.3 – 37.6 – 64.6 trillion cubic meters (tcm)) (P90 – P50 – P10) of natural (Andrews, 2013). This means that there is a 50% chance that the actual value is higher than the central value (1,329 tcf) and 10% chance that the true value lies above the high estimation (2,281 tcf). The UK's annual gas consumption is approximately 3 tcf per year, so 10% recovery rate of the P50 value corresponds to the total UK consumption for almost 50 years.

2.3 Hydraulic Fracturing

Since shales have very low permeability, hydraulic fracturing, commonly known as “fracking”, is required to generate commercial production from shale plays. Hydraulic fracturing is used to open pathways in the shale rock, thus increasing permeability and allowing trapped gas to escape from the rock matrix. This process allows natural gas to be extracted efficiently from a low-permeability reservoir like shale.

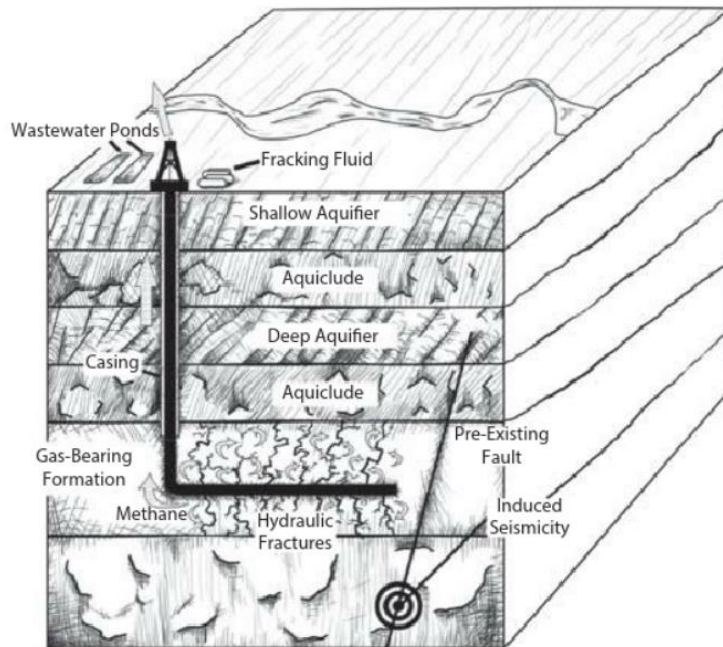


Figure 2-5: Basic hydraulic fracturing process utilizing horizon well drilling. Figure from Cheremisinoff et al. (2015).

Hydraulic fracturing is performed on a horizontal well to maximize the contact area between the well and the reservoir (Figure 2-5). The direction of well drilling is usually in the direction of minimum horizontal stress since hydraulic fractures will propagate in the maximum horizontal stress direction, and fractures orthogonal to the well track will maximize the contact area with the rock.

Zoback et al. (2019) show a typical workflow of hydraulic fracturing in multiple steps in detail starting from isolating sections of the well to be fractured, initially pumping fluid with low viscosity at low rate, increasing the rate, pumping a slurry (mixture of hydraulic fracturing fluid and proppant), and cleaning the wellbore with a “tail” fluid. After checking the result of hydraulic fracturing, hydrocarbons are then extracted from the opened flow paths.

A key element in shale gas development is the application of reflection seismic surveys (eg. Alzate & Devegowda, 2013; Perez & Marfurt, 2013). The imaging of geological structures within shale formations facilitates the development of shale plays as it directly influences the assessment of the productivity, operation cost, and risk.**2.4 Sweet Spots**

In order to maximize shale gas production, optimal placement of well sites must be considered. Areas that have good conditions for hydrocarbon productivity - high TOC, brittleness and porosity - are referred to as “sweet spots”. These sweet spots can be identified by analysing reflection seismic data and well logs to calculate elastic moduli, which can be used as proxies for petro-physical properties of rock formations.

2.4.1 TOC

TOC is one of the key variables that define a sweet spot. Chopra et al. (2012) states that acoustic impedance, density, velocity, and anisotropy can be indicators of TOC since the presence of organic matters in shale matrix influences these variables directly. Thus, determining TOC values of Bowland Shale by deriving these variables from the surface reflection seismic responses should be plausible. One of my aims in this study is to use acoustic impedance as a TOC indicator in the Bowland Shale. Low acoustic impedance values usually translate to high TOC, and thus, high organic matter content in shale matrix (Chopra et al., 2012). Acoustic impedance can be obtained through seismic inversion by applying a specific algorithm on angle gathers to estimate P-impedance, S-impedance, and bulk density (Ronald et al., 2018). The seismic inversion produces an impedance volume, which can be converted to TOC volume for further analysis. The results from the seismic inversion not only benefit the TOC measurement, but also brittleness assessment and, ultimately, sweet-spot identification.

2.4.2 Brittleness

Brittleness is very important in shale plays as it significantly affects the hydraulic fracturing capability, and thus, the productivity. Brittle rocks are much preferred in shale plays since they tend to produce more extensive fracture networks during the hydraulic fracturing. Poisson's ratio (ν) can be used as a proxy for siliceous mineral content and carbonate mineral content, which directly relate to the brittleness of rocks (Norton et al., 2011). More ductile rocks tend to exhibit higher values of Poisson's ratio.

2.4.3 Young's Modulus and Poisson's Ratio

Another variable that can be used to represent the physical properties of a rock is Young's modulus (E). Young's modulus can be utilized as an indicator of brittleness, recovery factor (RF), and more importantly, porosity, which can provide the information about the gas-in-place or the richness of rocks (Alzate & Devegowda, 2013). Young's modulus is directly correlated to the recovery factor (Goodway et al., 2010; Chopra et al., 2012; Perez & Marfurt, 2013), but it also has an inverse relationship with the porosity (Alzate & Devegowda, 2013). The combination of Young's modulus and Poisson's ratio has proved to be more efficient in sweet spot detection than either parameter on its own (Goodway et al., 2010; Chopra et al., 2012; Perez & Marfurt, 2013). Conveniently, both Young's modulus (E) and Poisson's ratio (ν) are products of the seismic inversion. E and ν can be defined as

$$E = 2I_S^2 \times \frac{(1+\nu)}{\rho} \quad (1)$$

$$\nu = \frac{0.5\left(\frac{V_P}{V_S}\right)^2 - 1}{\left(\frac{V_P}{V_S}\right)^2 - 1} \quad (2)$$

where E is the Young's modulus, ν is the Poisson's ratio, I_S is the acoustic impedance of S-wave, ρ is the bulk density, V_P is the velocity of P-wave, and V_S is the velocity of S-wave.

Areas that have large E and small ν have a tendency to be more brittle and have higher recovery factor; therefore, they are more favourable for drilling (Goodway et al., 2010; Chopra et al., 2012; Perez & Marfurt, 2013). However, Perez & Marfurt (2013) indicate that this combination cannot distinguish ductile limestone from brittle shale.

2.4.4 $\lambda\rho$ and $\mu\rho$

Goodway et al. (2010) propose a method to classify reservoirs based on their quality. Young's modulus and Poisson's ratio can be converted into Lamé's parameters rigidity (μ) and incompressibility (λ), which are more intuitive for seismic analysis and interpretation. The cross-plot between E , ν , and λ can separate brittle rocks from ductile ones better than the $E - \nu$ cross-plot. However, these Lamé's parameters fail to distinguish gas-bearing shales from calcareous shales. Therefore, a technique introduced by Goodway et al. (1997), the $\lambda\rho - \mu\rho$ cross-plot is preferred. This technique is very powerful as it can classify most of the facies in shale plays, and the variables $\lambda\rho$ and $\mu\rho$ are also indirect products of seismic inversion. $\lambda\rho$ and $\mu\rho$ can be calculated by using the following equations:

$$\lambda\rho = I_P^2 - 2I_S^2 \quad (3)$$

$$\mu\rho = I_S^2 \quad (4)$$

Where λ is the incompressibility, μ is the rigidity, ρ is the density, I_P is the acoustic impedance of P-wave, and I_S is the acoustic impedance of S-wave.

Additionally, the $\lambda\rho - \mu\rho$ cross-plot has been used to show various trends including Original Gas In Place (OGIP), pore pressure, fracture density and recovery factor (Alzate & Devegowda, 2013). Not only that, it can classify the quality of localities based their productivity and brittleness, which is very advantageous for identifying sweet spots, as shown in Figure 2-6 (Alzate & Devegowda, 2013).

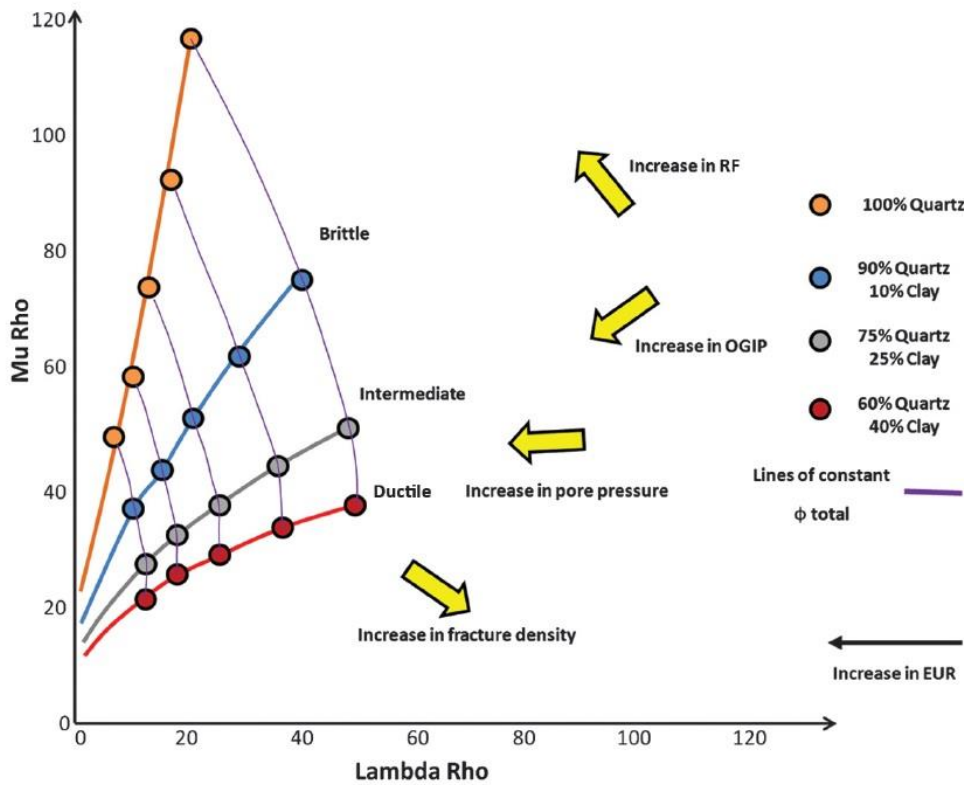


Figure 2-6: Trends in the $\lambda\rho - \mu\rho$ cross-plot. From “Integration of surface seismic, microseismic, and production logs for shale gas characterization: Methodology and field application” by Alzate, J. H., & Devegowda, D., 2013, Interpretation, 1(2).

2.5 Geographical Settings of the Bowland Shale

This study analyses the 3D seismic data volume acquired on the Fylde Peninsula in western Lancashire between Preston and Blackpool (Figure 2-7 and 2-8). Unlike many shale plays in North America, where the shale formations are relatively flat and undeformed, there is a significant amount of deformation in this area (Andrews, 2013). The rocks have experienced a series of geological events, creating faulting and unconformities, which are clearly visible in the 3D seismic volume. The study area is a part of the Bowland Basin (sometimes referred to as the Craven Basin), which is bounded by faults striking in the NE-SW direction. The basin was developed during the late Paleozoic (Devonian-Carboniferous) by extensional forces in the approximately N-S to NW-SE direction rifting the region (Anderson et al., 2020). It is a part of a large basin network consisting of numerous grabens and half grabens, which extends from England across Ireland towards the Maritimes in Canada as a result of the opening of Palaeotethys (Clarke et al., 2018). In this study area, the Craven Fault System lies to the north, separating the Bowland Basin from the Lancaster High, while the Pendle Lineament is the boundary between the Bowland Basin and the Western Lancaster High to the south and east. The rifting was followed by a thermal subsidence during the Namurian and Westphalian (Pennsylvanian) (Anderson et al., 2020; Clarke et al., 2018).

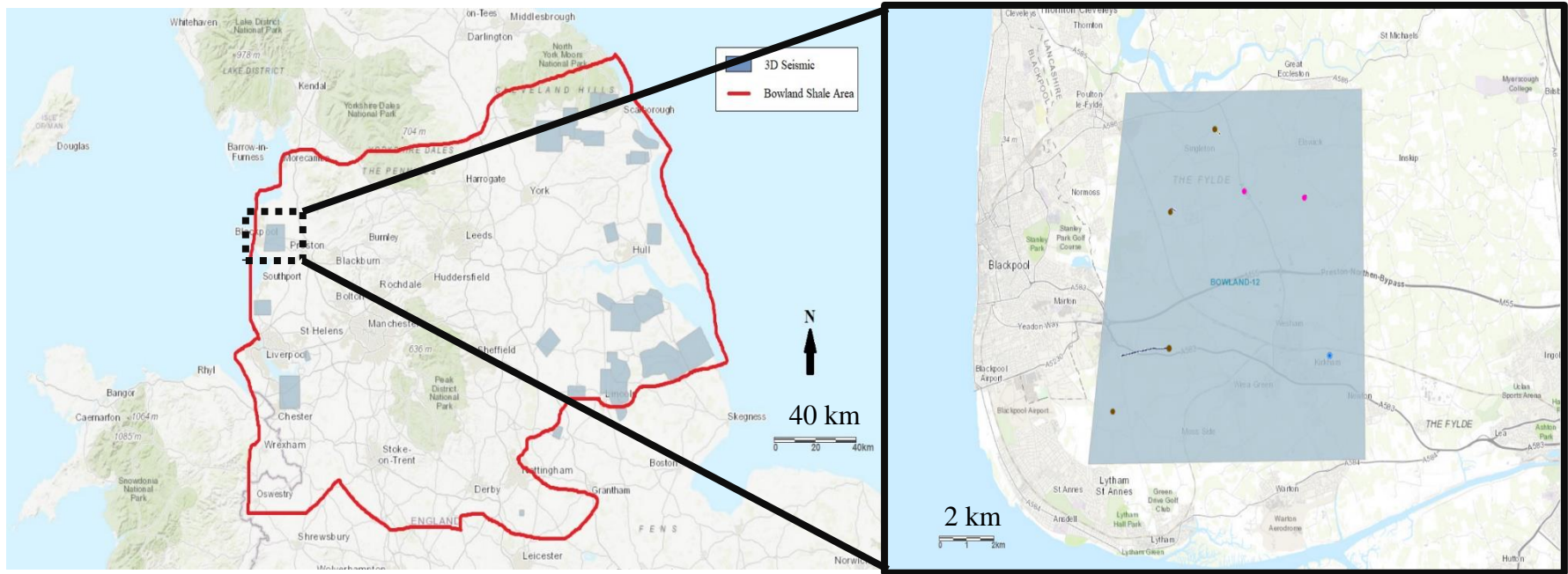


Figure 2-7: The location of the Bowland Shale in the central UK. The blue trapezoid located between Blackpool and Preston in the right figure shows the area of the 3D seismic data used in this study.

During the late Carboniferous and Permian, the Collision between Laurussia and Gondwana generated the Variscan Orogeny creating significant deformation in the region. Exhumation and erosion caused the disappearance of some parts of Carboniferous sequences before the sedimentation resumed in Permian-Triassic. The results of these processes can be observed in the 3D reflection seismic data.

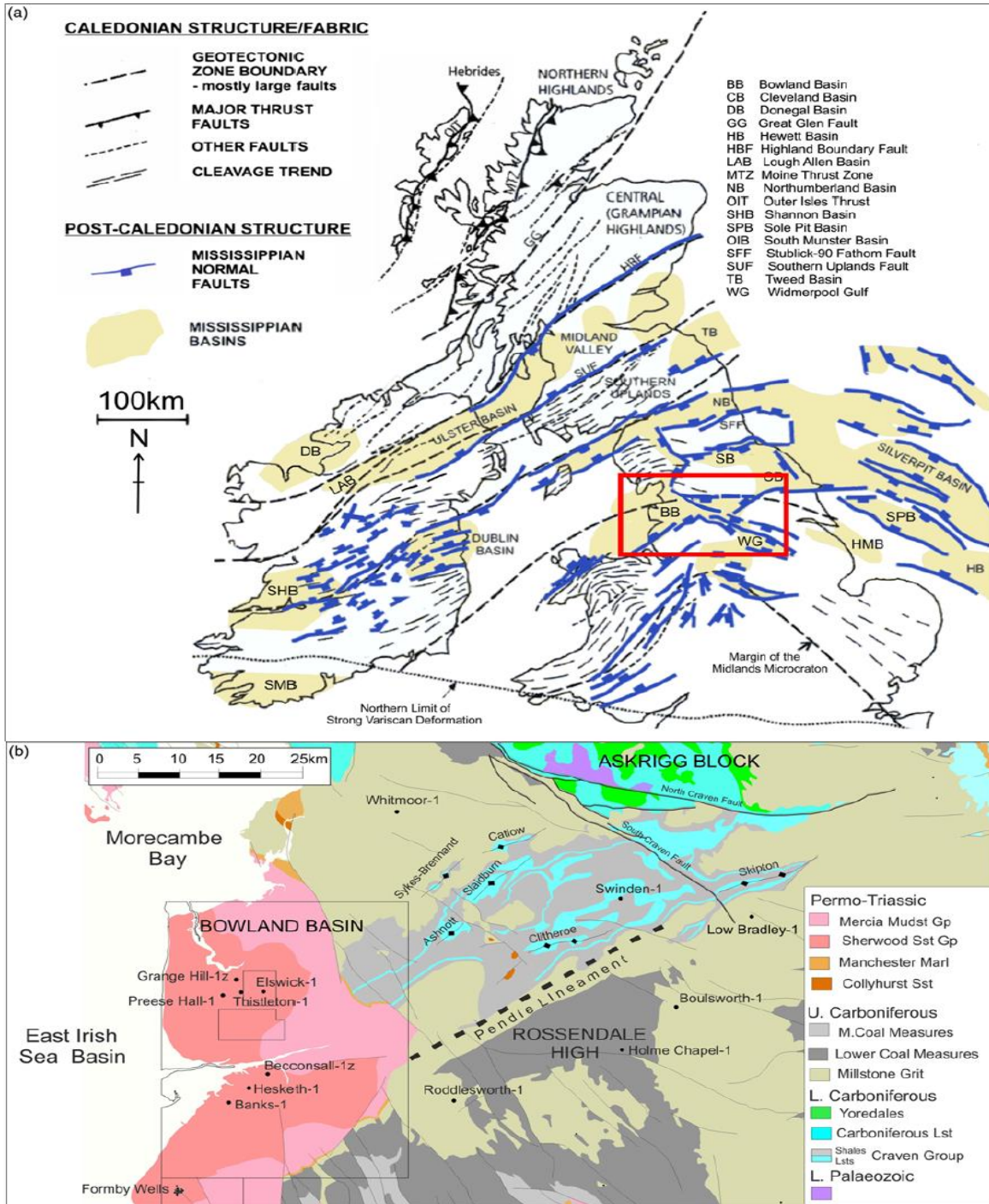


Figure 2-8: Geographical settings and structures of the study area and surroundings. From “Felt seismicity associated with shale gas hydraulic fracturing: The first documented example in Europe” by Clarke et al., 2014, *Geophysical Research Letters*, 41(23), 8308–8314.

2.6 Stratigraphy

The stratigraphy of Carboniferous rocks in the Bowland Basin starts with the Chatburn Limestone Formation, deposited in the early Mississippian (Anderson et al., 2020). After that, the Craven Group or Worston Shale Group was deposited on top of the Chatburn Limestone Formation. This group includes Clitheroe Limestone Formation, Hodder Mudstone Formation, Hodderense Limestone Formation, and Pendleside Limestone Formation. The lower and upper Bowland Shale Formations were deposited after that as a part of Bowland Shale Group during the late Viséan to early Namurian. It is overlain by the Milstone Grit Group, which represents coarser clastic deposition. These formations are overlain by the Variscan Unconformity, represented the period of uplift and erosion discussed above. Deposited in Permian, the Collyhurst Sandstone Group lies above the Variscan Unconformity. It is followed by the Manchester Marl Formation (late Permian), Sherwood Sandstone Group (early Triassic), and Mercia Mudstone Group (Triassic), which is the youngest group in the sequence (Anderson et al., 2020). The stratigraphy of the Bowland Basin is shown in Figure 2-9.

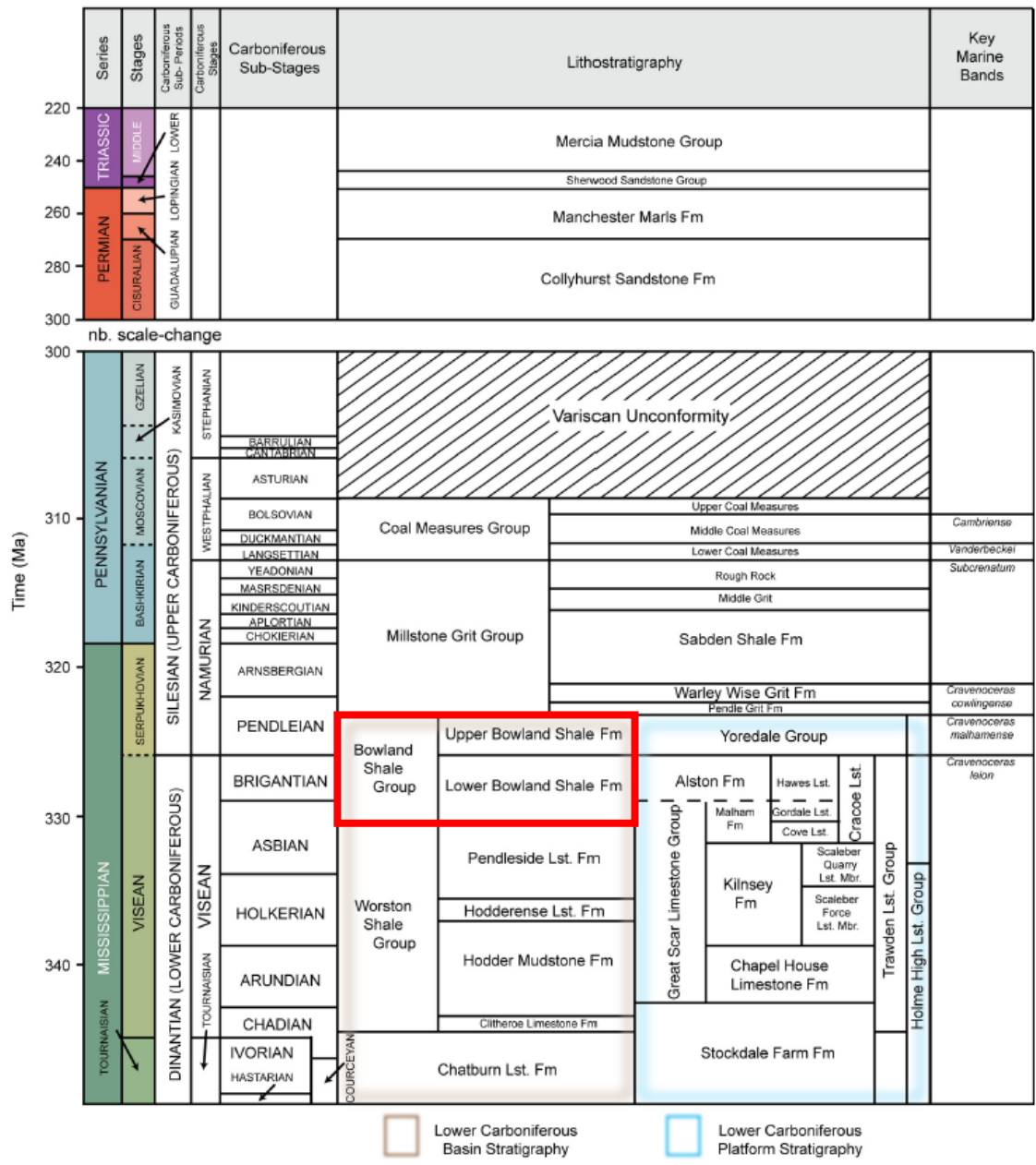


Figure 2-9: Stratigraphy of the Bowland Basin. The red rectangular represents the Bowland Shale Formation. The stratigraphy is separated into basin stratigraphy (eg. Bowland Basin) and platform stratigraphy (eg. Lancaster High), though they were developed at the same time. From “Structural Constraints on Lower Carboniferous Shale Gas Exploration in the Craven Basin, NW England” by Anderson & Underhill, 2020, *Petroleum Geoscience*, 26(2):303.

2.7 Bowland Shale Formation

Among the various shale formations in UK, the Bowland Shale Formation is considered to be the most promising in terms of hydrocarbon productivity because it has high TOC, brittleness, and porosity (Smith et al., 2010). It is an organic-rich dark grey-to-black shale with limestone, calcareous mudstone, siltstone, and fine-grained sandstone interbedded. The suggested depositional environment of this formation is a marine environment with relative sea level fluctuations changing and alternating the environment from a deep marine to a deltaic facies (Andrew, 2013). The Bowland Shale Formation is relatively thick in comparison to many shale plays in North America, reaching up to 5 km in fault-bounded areas, though its usual thickness is around 1 km. Bowland Shale has a clay content of 56-59%, with 45% quartz, and 10% carbonate content (Smith et al., 2010). The core and log data from the Preese Hall-1 (PH-1) well suggest that the gas density and the TOC of Bowland Shale are comparable to those of North American shale plays (Clarke et al., 2019; Andrews, 2013).

2.7.1 Lower Bowland Shale Formation

The Bowland Shale Formation is divided into the upper and lower sub-units. The Lower Bowland Shale (including Pendleside Sandstone and its associated shales) was deposited during the late Viséan. It is a syn-rift formation, deposited in grabens and half-grabens. The thickness of this sub-unit is relatively thicker than the Upper Bowland Shale, as it can reach 3,000 m (10,000 ft) in the depocenter (Andrews, 2013). In the seismic sections, the Lower Bowland Shale has strong internal reflections, which implies the substantial lithological variations in this sub-unit. The Pendleside Sandstone is a highly variable sandstone turbidite that lies in the middle part of the Lower Bowland Shale with an approximate maximum thickness of 300 m. The sources of these turbidites are from the basin edges and the erosion of Askrigg Block and Central

Lancashire High limestones during palaeokarst formation (Clarke et al., 2018). While few wells have been drilled into the Lower Bowland Shale, the limited available data suggest that it has a good chance to yield more resources than the upper Bowland Shale. The total in-place gas estimation of this sub-unit is 658 – 1,065 – 1,834 tcf (18.7 – 31.2 – 51.9 tcm) (Andrews, 2013).

2.7.2 Upper Bowland Shale Formation

The Upper Bowland Shale was deposited during the post-rift phase. Unlike the Lower Bowland Shale, it has relatively weak reflections in the seismic data, indicating that it is a more homogenous unit. The lower part of the Upper Bowland Shale is represented by a marine transgressive system tract as the sea level was rising. This promoted the growth of carbonate platforms, which then, cut off the supply of coarse clastic materials into the basin (Clarke et al., 2018). This results in the lack of lithologic variation as represented by weak seismic reflections and high values of gamma ray. The boundary between the two sub-units is the marine flooding surface that marks the beginning of the Namurian. Clarke et al. (2018) use the ammonoid *Emstite leion* as a biomarker, as it is found above the marine flooding surface (Upper Bowland Shale) and not below (Lower Bowland Shale). The Upper Bowland Shale has better well control, providing more numerous and accurate data for this sub-unit. The depth to the top of this sub-unit can reach up to 4,750 m (16,000 ft) across the central UK. The usual thickness of this unit is around 150 m (500 ft), but it can locally reach up to 890 m (2,900 ft). It has been estimated by British Geological Survey (BGS) that there is 164 – 264 – 447 tcf (4.6 – 7.5 – 12.7 tcm) of total in-place gas in this sub-unit (Andrews, 2013).

2.8 Induced Seismicity

An earthquake, or seismicity, is a ground vibration produced by a sudden release of tectonic stress on a fault (National Research Council (U.S.), 2013). Sizes of earthquakes vary by many orders of magnitude, from a devastating ground shaking to a small vibration that cannot be perceived by humans. An earthquake can be generated by both natural causes and human activities. Natural earthquakes occur along faults that rupture due to the accumulation of tectonic stress. Induced seismicity, or anthropogenic seismicity, is a phenomenon where human activities such as fluid injection, fluid withdrawal, or mining cause changes in subsurface stress, which then trigger a rupture generating an earthquake (Keranen & Weingarten, 2018).

Hydraulic fracturing generates microseismic events since it involves fluid injection to fracture rock formations. These microseismic events usually are too small even to be perceived by humans; however, hydraulic fracturing can occasionally generate events large enough to be felt at the surface. These rare cases can create public concerns, and has the potential to cause hazards and damage to lives and buildings. Keranen and Weingarten (2018) pointed out that there were several cases of induced seismicity by fluid injection that caused notable damages to buildings such as the series of large induced earthquakes including the M_w 5.8, M_w 5.7, and M_w 5.0 earthquakes in Oklahoma, USA in 2016, and the M 3.6 event in the Groningen field, Netherland in 2012. Felt seismicity does not trouble offshore exploration as much as it does to onshore ones since onshore wells are closer to human habitats.

Felt seismicity has become a significant issue for onshore unconventional explorations. There have been reports of felt seismicity since the utilization of hydraulic fracturing in unconventional resources extraction. Shale plays in Western Canadian Sedimentary Basin (WCSB), for example, produced felt seismicity during the injection phases of hydraulic fracturing. In some cases, the faults that ruptured and caused the felt seismicity have been

detected on the 3D reflection seismic data (eg. Eyre et al., 2019), but some have not been (eg. Eaton et al., 2018; Kettlety et al., 2019). Kettlety et al. (2019) investigated a reactivated fault that caused induced seismicity in the Horn River Basin in British Columbia, Canada, and found that the fault is not visible on 3D seismic data. Similarly, in the ToC2ME dataset from Fox Creek, Canada studied by Eaton et al., 2018, faults near the felt seismic event locations (maximum magnitude of M_w 3.2) were mapped on the 3D seismic data, but the fault that actually reactivated during the hydraulic fracturing was not visible (Eaton et al., 2018). Eyre et al. (2019), on the other hand, was able to identify the reactivated fault that caused M_w 4.1 induced earthquake at an adjacent site. The inconsistency in identifying the causative faults might be because of the difference in size of each faults and the quality of 3D seismic data, which can produce noises and interferences.

The first case of felt seismicity from shale gas hydraulic fracturing in Europe was reported at the PH-1 well in Lancashire, UK in 2011 (Clarke et al., 2014). The PH-1 well was drilled as a part of an unconventional gas prospect in the Bowland Shale Formation. This operation generated 2 felt seismic events of magnitudes M_L 2.3 and M_L 1.5, causing the operation to be temporarily stopped (Clarke et al., 2014). The 3D reflection seismic data from the seismic survey in 2012 was able to identify the causative fault. This might be because the causative fault is slightly oblique, allowing the similarity attribute to pick up the fault.

The inconsistency of identifying causative faults poses a challenge for mitigating induced seismicity at future sites. It also suggests that our geological technology and knowledge can improved. A key objective of this thesis is therefore to investigate the ability of seismic attribute analysis to identify the presence of the causative faults. However, successful identification of faults does not necessarily translate to the avoidance of drilling in those locations. This is

because each location has different pore pressure and stress field magnitude and orientation, which contributes to the chances of slipping of each fault, according to the Coulomb faulting theory (Walsh et al., 2018). Thus, these variables, combining with fault location and orientation data from this study, should be taken into consideration for risk assessments and operation planning.

2.9 Hydraulic Fracturing in the Bowland Shale

2.9.1 The First Case of Felt seismicity in the Bowland Shale

The potential for hydrocarbon extraction from the Bowland Shale was first identified by Selley (1983). However, Cuadrilla Resources Ltd (CRL)'s operations to exploit the resources from Bowland Shale Formation in Lancashire, UK, have been active since the early 2010s. The first hydraulic fracturing of this formation took place in 2011 at the PH-1 well on the Fylde Peninsula, Lancashire (Clarke et al., 2014). On 1 April 2011, a magnitude M_L 2.3 earthquake was detected by the BGS near PH-1 well after several stages of fluid injection had been performed. The event was felt by the public in nearby villages. It was the first reported felt-seismic event induced by unconventional gas exploration in Europe.

Initially, the event only raised slight concerns since the location of the event had large uncertainties because of the lack of nearby monitoring stations. The operation was temporarily stopped for further assessment, and then resumed after local seismometer stations had been installed (Clarke et al., 2014).

Another felt seismic event associated with the hydraulic fracturing (M_L 1.5) was detected the day after the injection had resumed, causing the suspension of the operation. A total of 52 events were identified using a matched filter based on the two largest events, ranging from M_L -2

to M_L 2.3 (Clarke et al., 2014). These events tended to occur during the fluid injection phases, with lower seismic activity during the flowback phases between and post injection. Most of the induced seismic events were recorded on only a few of the regional seismic stations, and thus did not provide the reliable data regarding the hypocenter location. Only the M_L 0.2 event on 2 August 2011 was usable to reliably calculate a source mechanism and find the hypocenter, which was 300 – 400 m (with uncertainties of ± 150 m) east of the injection location, with a depth of 330 – 360 m below the well (Clarke et al., 2014).

The 3D seismic data was acquired after these events, which revealed the potentially reactivated fault which is located near the PH-1 well, where the events had occurred. Clarke et al. (2014) used cross-correlation and curvature attributes to map the fault that reactivated to cause the felt seismicity.

After a brief moratorium imposed by the UK government, the Traffic Light Scheme (TLS) was introduced to regulate induced seismicity. The TLS requires a pause in operations of any seismic event with a magnitude over a certain threshold occurs. In the UK, the “red light” was set at magnitude M_L 0.5. However, TLSs are retroactive, meaning that the actions are taken after an event had already taken place, so the debate continues with respect to the effectiveness of TLSs for preventing induced seismicity (e.g., Clarke et al., 2019).

2.9.2 Felt seismicity in the Bowland Shale in 2018-2019

CRL performed further hydraulic stimulation in the Bowland Shale at the Preston New Road (PNR) site in 2018 and 2019, as shown in Figure 2-10. Two horizontal wells were drilled to extract resources from the Bowland Shale Formation. The PNR-1z well targeted the Lower Bowland Shale (~2.2 km depth), while the PNR-2 well aimed at the Upper Bowland Shale (~2.0 km depth). Hydraulic fracturing in the PNR-1z well in 2018 was paused several times after the triggering of “red light” events with magnitudes larger than M_L 0.5, including an M_L 1.5 event that was felt by a few local residents (Clarke et al., 2019). In 2019, hydraulic fracturing of the PNR-2 well triggered an M_L 2.9 event. This event was widely felt in the nearby towns of Preston and Blackpool, and led to the government imposing a further moratorium on hydraulic fracturing for shale gas. The faults that caused these events were not identified by the operating company in the hydraulic fracturing plan submitted to the regulator prior to the operation (Clarke et al., 2019). A key objective of this thesis is therefore to investigate whether seismic attribute analysis can reveal the presence of these features.

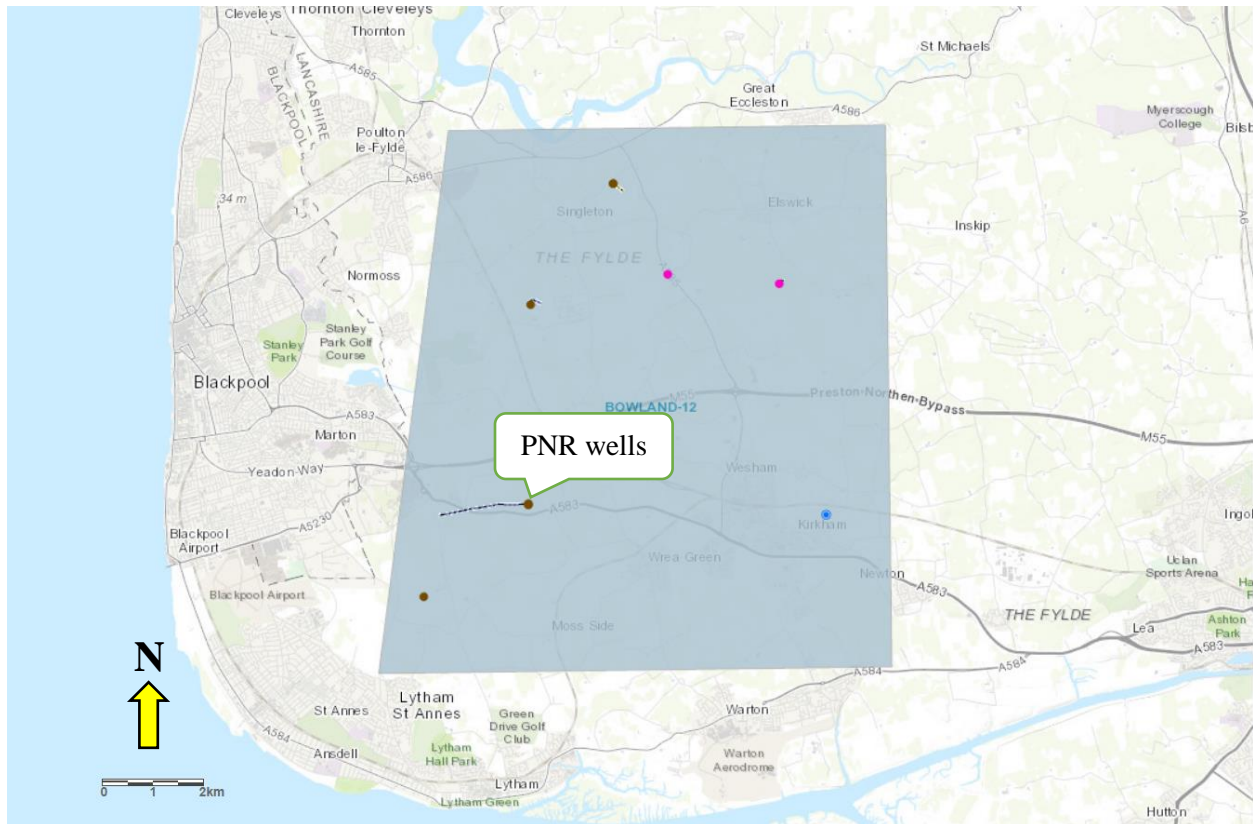


Figure 2-10: The location of the PNR wells. The blue trapezoid is the area of the 3D seismic data used in this study. The small circles represent the well locations, with black well tracks.

2.10 Application of Seismic Attributes on Fault Investigation at the PNR Site

Computing attributes from 3D reflection seismic data can potentially facilitate the detection of the causative faults that are not immediately visible in raw seismic data. Similarly, curvature, and spectral decomposition are common attributes used for fault investigation as they are sensitive to changes in seismic signals and seismic textures, facilitating the fault investigation (Chopra & Marfurt, 2008).

2.10.1 Similarity

The similarity attribute measures coherence, comparing signals between adjacent gathers, typically using cross-correlation (Bahorich & Farmer, 1995). To calculate the similarity attribute, sample traces are considered as coordinates of vectors in hyperspace, and then, Euclidean distances between vectors are calculated and normalized over the vector lengths (Tingdahl & De Groot, 2003). A fault may create a difference in the signals between those locations; thus, the similarity attribute would highlight faults as regions with low similarity, making them easier to be detected. The similarity attribute can be applied on time slices and horizon slices to produce different outcomes. Horizon slices track the topography of surfaces; therefore, the discontinuities caused by features such as faults that offset the surfaces can be mitigated. Features that cause small changes on the surfaces such as channels or levees would be more likely to show up on horizontal slices than on time slices.

2.10.2 Curvature

The curvature attribute indicates the rate of change of dip of a surface. In other words, it is a measure of how deformed or bent a particular point of a surface is. In two dimensions, the curvature is the reciprocal of the radius of a circle tangent to the surface (Figure 2-11). The larger the curvature is, the more the surface is bent. Positive curvature values represent antiform features, while negative values represent synform features. Thus, the curvature attribute can be used to detect channels and faults that offsets a surface, or enhance relief of geological features. In three dimensions, the curvature is calculated from 2 perpendicular vertical planes by using the same method. They are referred to as normal curvatures, composing of maximum and minimum curvatures. The maximum curvature is a measure of the maximum bending of a surface at the given point, while the minimum curvature measures the curve perpendicular to the maximum

curvature. The maximum curvature is typically utilized in fault detection. There are various types of curvature, including mean curvature, Gaussian curvature, most-positive curvature most-negative curvature, dip curvature, and strike curvature, though most-positive and most-negative curvatures are the most convenient to use to detect geological features (Chopra & Marfurt, 2007). Most-positive and most-negative curvature attributes calculate the most positive and most negative values from the normal curvature.

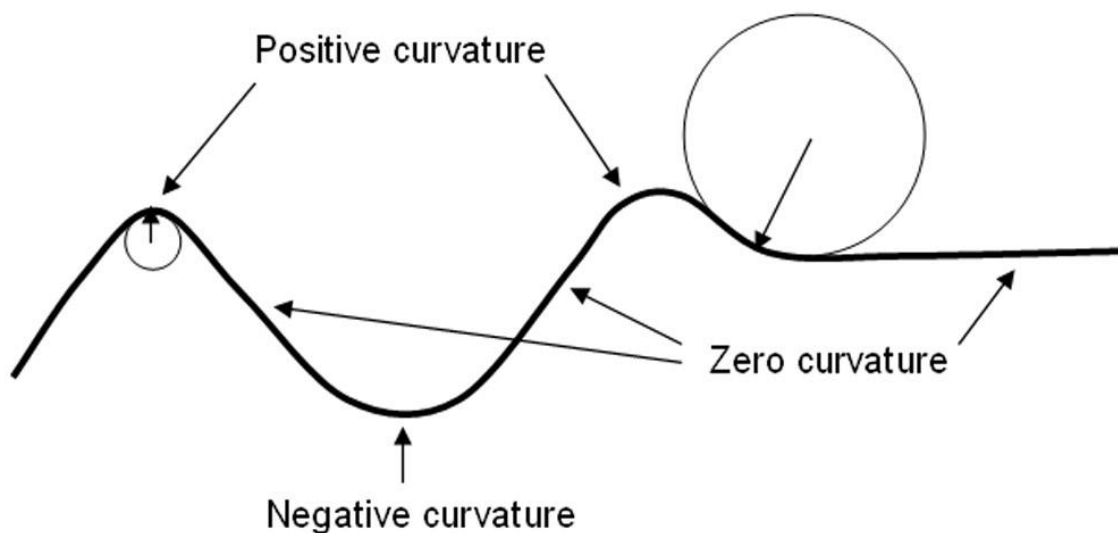


Figure 2-11: Explanations of the curvature values. The curvature is positive at antiforms, negative at synforms, and zero at flat lines or places with no curviness. From “Seismic curvature attributes for mapping faults/fractures, and other stratigraphic features” by Chopra & Marfurt, 2007, Recorder, 32(9).

2.10.3 Spectral Decomposition

Spectral decomposition is a method of converting seismic signals from time domain to frequency domain using certain algorithms such as the Discrete Fourier Transform (DFT) or

Continuous Wavelet Transform (CWT). The data in the frequency domain, can then be tuned to a specific frequency value to manipulate the interference of signals for highlighting geological features. Different geological features have different tuning behaviours since the interference is influenced by local distribution of the impedance contrasts and the wavelet. For example, faults with different sizes and locations would tune in or tune out at different frequencies. Therefore, it is commonly utilized for identifying lateral changes or discontinuities on a surface such as channels and faults. In practice, the spectral decomposition attribute is commonly used with RGB-colour blending. The attribute volumes are computed using 3 different ranges of tuning frequency (low, mid, and high), represent by different colour schemes (red, green, and blue). Then, they can be overlapped and displayed together as one attribute, which can improve the accuracy of the results and interpretations.

Chapter 3: Seismic Data

This chapter covers the data used in the further analysis including the 3D reflection seismic data and the well data in more detail. Chapter 3 also explores the studies of Kettlety et al. (2020) and Clarke et al. (2019), which are the attempts to locate the reactivated fault planes by using the microseismic data and event catalogues.

3.1 3D Reflection Seismic Data

The 3D reflection seismic survey that I study in this thesis was acquired in Lancashire, UK, in June 2012 with the main objective of imaging the Bowland Shale Formation. The data acquisition was performed by CGGVeritas company (CGGV) for CRL. According to the CGGV report by Sayers (2012), the survey covers about 125 km² of mostly flat farmlands with small villages to the east of Blackpool (Figure 3-1). The data is in the seismic line system, where inline is the direction of the receiver cable (East-West) and the crossline is the direction perpendicular to the inline (North-South). The inline and crossline ranges in this survey are 4,989 to 5,430 and 2,000 to 2,450 with the bin size of 25.0 m × 25.0 m. The data acquisition process was done by utilizing explosive sources (90.95%) with a few applications of vibroseis (9.05%), which can generate compressive wave in places where explosive sources were not feasible from logistical perspective. Single component vertical geophones (10 Hz) were used as the recording instrument. The receiver line spacing is 250 m, spreading East-West symmetrically ± 3,000 m from the source. Each of the 24 receiver lines consists of 120 live stations with the total of 2,880 live channels, with the receiver interval of 50 m. The shot lines are in the North-South direction with 250 m of the line spacing and 50 m of the shot interval. The record length of each shot is

6,000 ms long with 2 ms of the sample rate. A high-cut filter (200 Hz) was applied to improve the quality of the data.

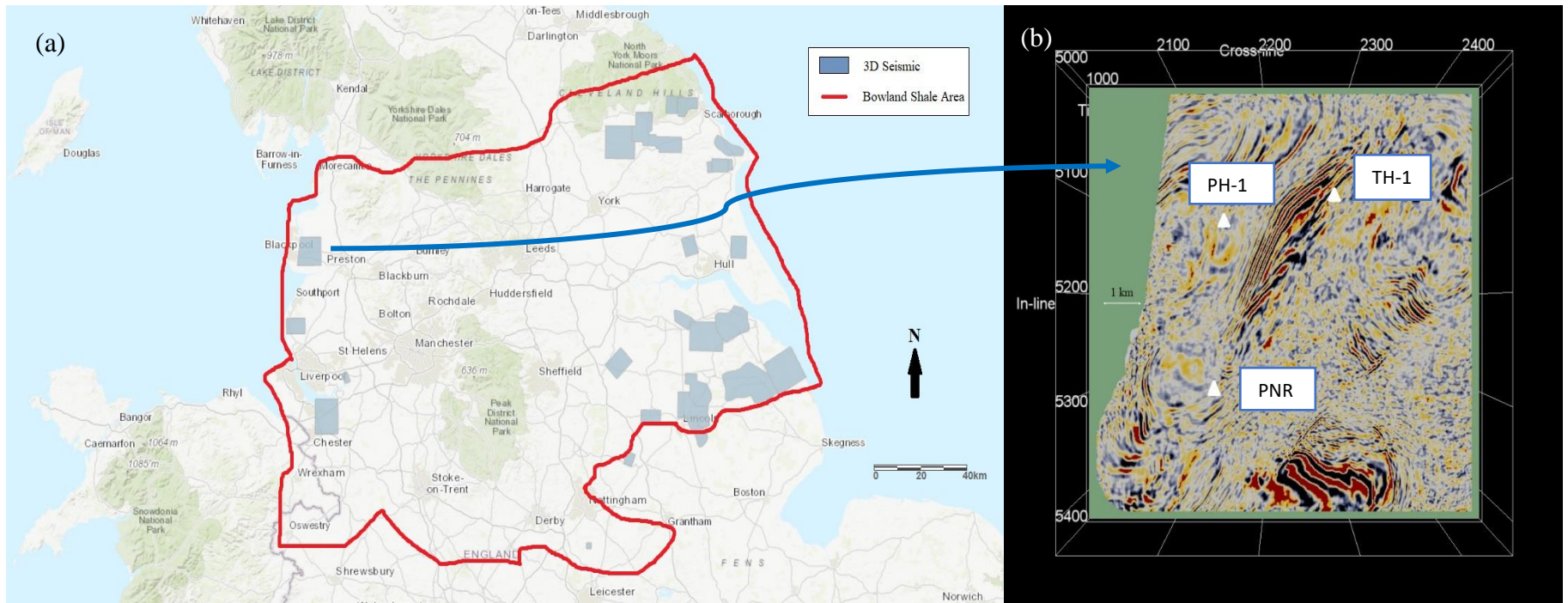


Figure 3-1: (a) The geographical position of the 3D reflection seismic survey in the central UK. (b) The time slice of the 3D seismic data at 1,120 ms (2.02 km depth) with well locations.

Several geophysical processing steps were performed on this data set by a contractor to reduce noise and improve image quality. These processes include resampling the data by applying tomographic inversion statics, applying time correction, noise attenuation, amplitude recovery, time migration, normal moveout correction, and common depth point stack. The final result is a post-stack 3D reflection seismic data in SEG-Y format, which is used as the foundation for this study. Further analysis such as fault and horizon interpretations have been done by CRL, BGS, and Anderson and Underhill (2019). However, due to the high geological complexity of this area, more interpretations are necessary for more accuracy.

3.2 The Investigation of Reactivated Faults During the Hydraulic Fracturing at the PNR Site

After the induced seismicity in 2018 and 2019, the microseismic event catalogues from the PNR wells have been studied to identify the faults that caused the felt seismic events (Clarke et al., 2019; Kettlety et al., 2020). Microseismic event populations from both the PNR-1z and PNR-2 wells display clear patterns. The events propagated from the injection sleeves in the direction parallel to the maximum horizontal stress (azimuth of $\sim 170^\circ$), as shown in Figure 3-2 (Clarke et al., 2019; Kettlety et al., 2020). Clarke et al. (2019) observed a relationship between the rate of seismicity and the injection volume, and the event distribution follows the Gutenberg-Richter distribution (GR distribution).

To identify faulting associated with the PNR-1z induced seismicity, Clarke et al. (2019) mapped larger events ($M > 0$), with the focal mechanism nodal planes as an additional constraining factor. The microseismic event locations during an injection hiatus provided additional constraints, since the events during this hiatus were inferred to have occurred along

the reactivated fault plane. The fault plane of the event near the PNR-1z well is shown in Figure 3-2 with the strike of $\sim 237^\circ$ and dip of $\sim 70^\circ$ towards the northwest.

Kettlety et al. (2020) used the aftershocks of the M_L 2.9 event to identify the rupture plane at the PNR-2 well. Since the event occurred 3 days after the pumping operation had ceased, the downhole array was not acquiring data at the time the event occurred. Instead of using the surface array, which is less precise for the fault identification, Kettlety et al. (2020) utilized the locations of the aftershock events, which were recorded by the downhole system, to delineate the location of the fault plane (Figure 3-3). The plane has the strike of $\sim 130^\circ$ and dip of $\sim 80^\circ$ towards the southwest with the approximated dimension of $350 \text{ m} \times 250 \text{ m}$, which was consistent with the fault area derived from the seismic moment, shear modulus and slip length (Kettlety et al., 2020).

Even though the fault planes were identified at both PNR-1z and PNR-2 wells, they are not visible on the 3D reflection seismic data (Clarke et al., 2019; Kettlety et al., 2020). Therefore, the one of the main objectives of this study is to investigate whether these faults can be identified using seismic attributes.

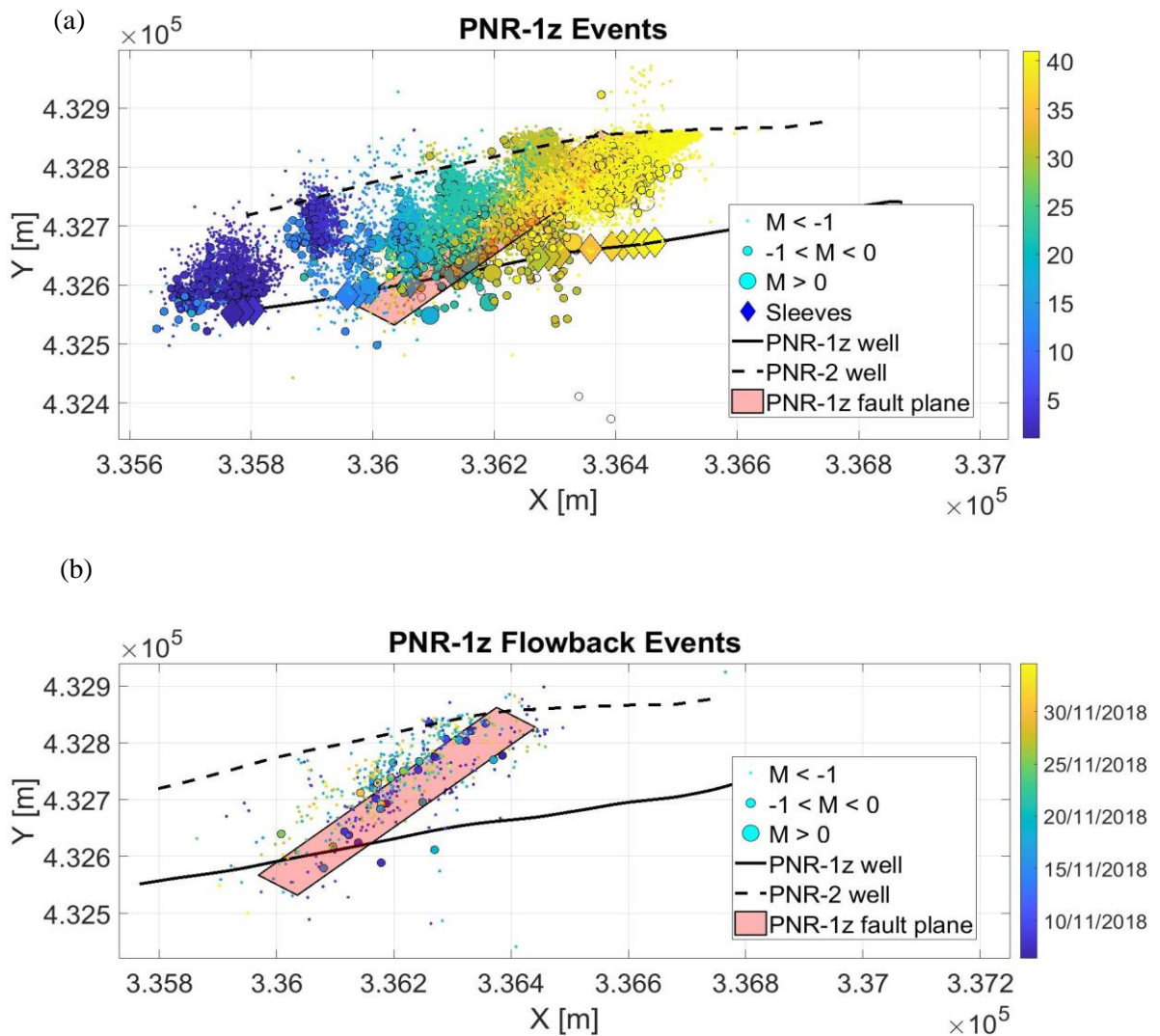


Figure 3-2: Identification of the reactivated fault at the PNR-1z well. (a) Events that occurred during the stimulation in map-view, coloured by stage number. (b) Events that occurred during the injection hiatus. Clarke et al. (2019) established a fault plane from the larger ($M > 0$) events that occurred during the hiatus. Circles represent the locations of the events with their sizes based on the sizes of the events. Diamonds show the locations of the injection sleeves. The solid black line is the PNR-1z well track, while the dashed black line is the PNR-2 well track. The pale red plane is the PNR-1z fault plane established by Clarke et al. (2019).

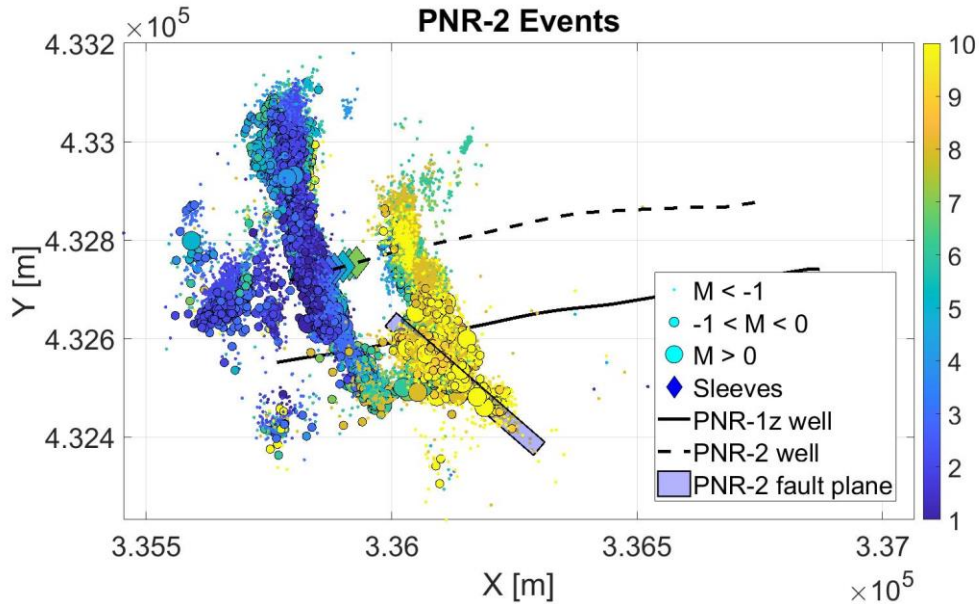


Figure 3-3: Identification of the reactivated fault at the PNR-2 well. The figure shows the events that occurred during the stimulation in map-view, coloured by stage number. Kettlety et al. (2020) established a fault plane from the aftershock events. Circles represent the locations of the events with their sizes based on the sizes of the events. Diamonds show the locations of the injection sleeves. The solid black line is the PNR-1z well track, while the dashed black line is the PNR-2 well track. The blue plane is the PNR-2 fault plane established by Kettlety et al. (2020).

3.3 PH-1 and PNR-1 Well logs

Figure 3-4 shows the PH-1 well logs including P-wave sonic log (DT), S-wave sonic log (DTS), bulk density (RHOB), natural gamma ray (GR), neutron porosity (NPHI), and P/S-wave velocity ratio (V_p/V_s). The sonic logs are presented as compressional and shear-wave slowness. The gamma-ray data is typically considered to be a proxy for the percentage of clay and shale content within a rock.

The boundaries of the rock formations are clearly delineated by the abrupt changes in the parameters as displayed in Figure 3-4, as well as Figure 3-5, which displays the PH-1 well logs

within the range of Bowland Shale Formation. The abrupt changes in the log parameters at around 2,500 m mark the contact between the Upper Bowland Shale and the Lower Bowland Shale. Figure 3-4 shows that the V_p/V_s ratios in the Bowland Shale Formation are lower than other units. The cause of this phenomenon might be the presence of gas in the Bowland Shale since the presence of gas within the pore space will act to lower V_p and increase V_s due to the decreases of bulk modulus and density (Hamada, 2004). The Lower Bowland Shale Formation well logs appear to have significantly more variability than in the Upper Bowland Shale, suggesting that the Lower Bowland Shale is more heterogenous than the Upper Bowland Shale. Similarly, Figure 3-6 shows the DT, DTS, and GR logs for the PNR-1 well from 1,800 – 2,650 m depth. The PNR-1 well logs contain data from the Lower Bowland Shale Formation and a small portion of the Upper Bowland Shale Formation.

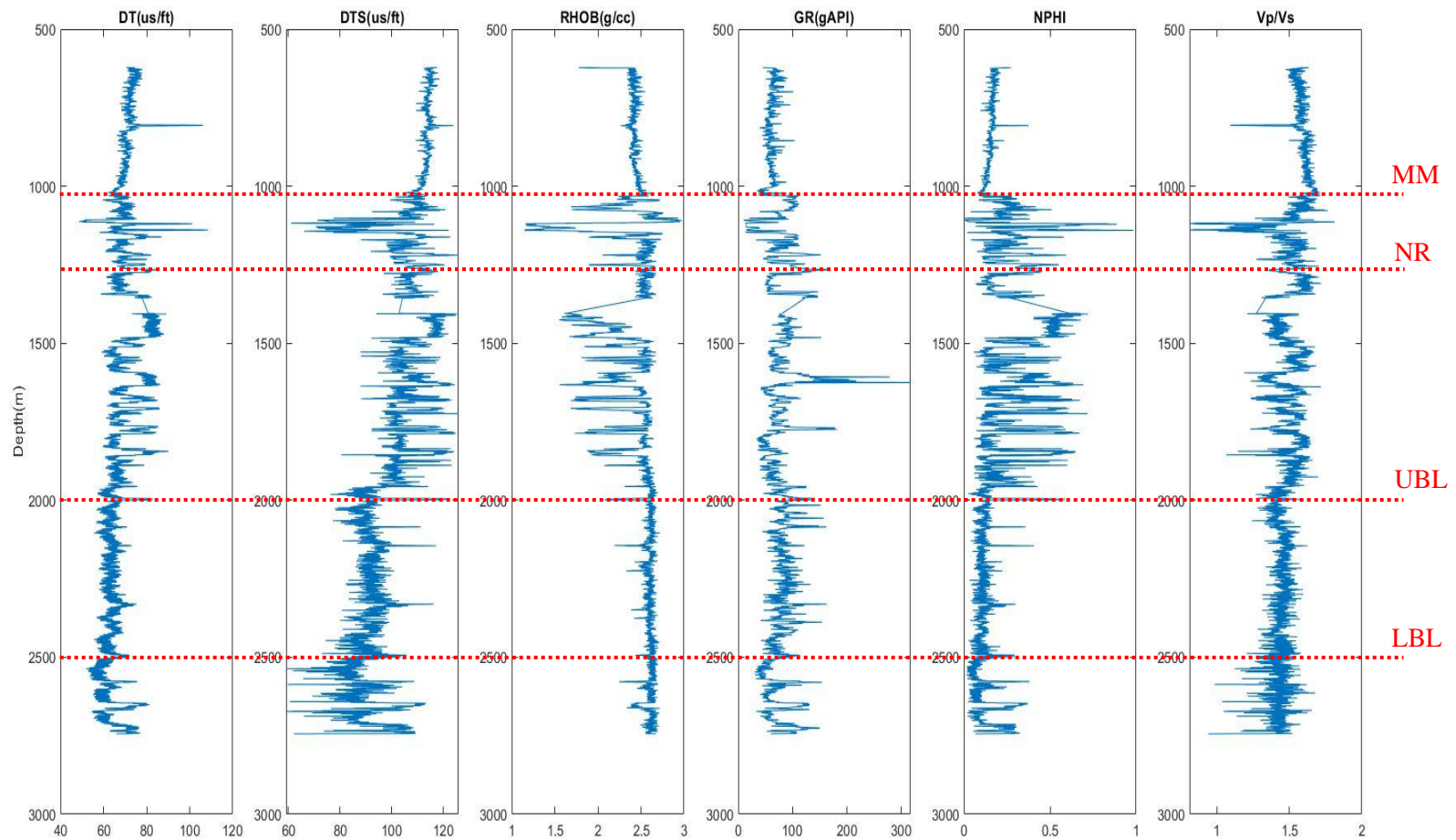


Figure 3-4: PH-1 well logs. The formation tops' markers are represented by the red, dashed lines labeled with the abbreviated formation names. MM stands for the Manchester Marl Formation, NR is the Namurian Rough Rock, UBL is the Upper Bowland Shale Formation, and LBL represents the Lower Bowland Formation.

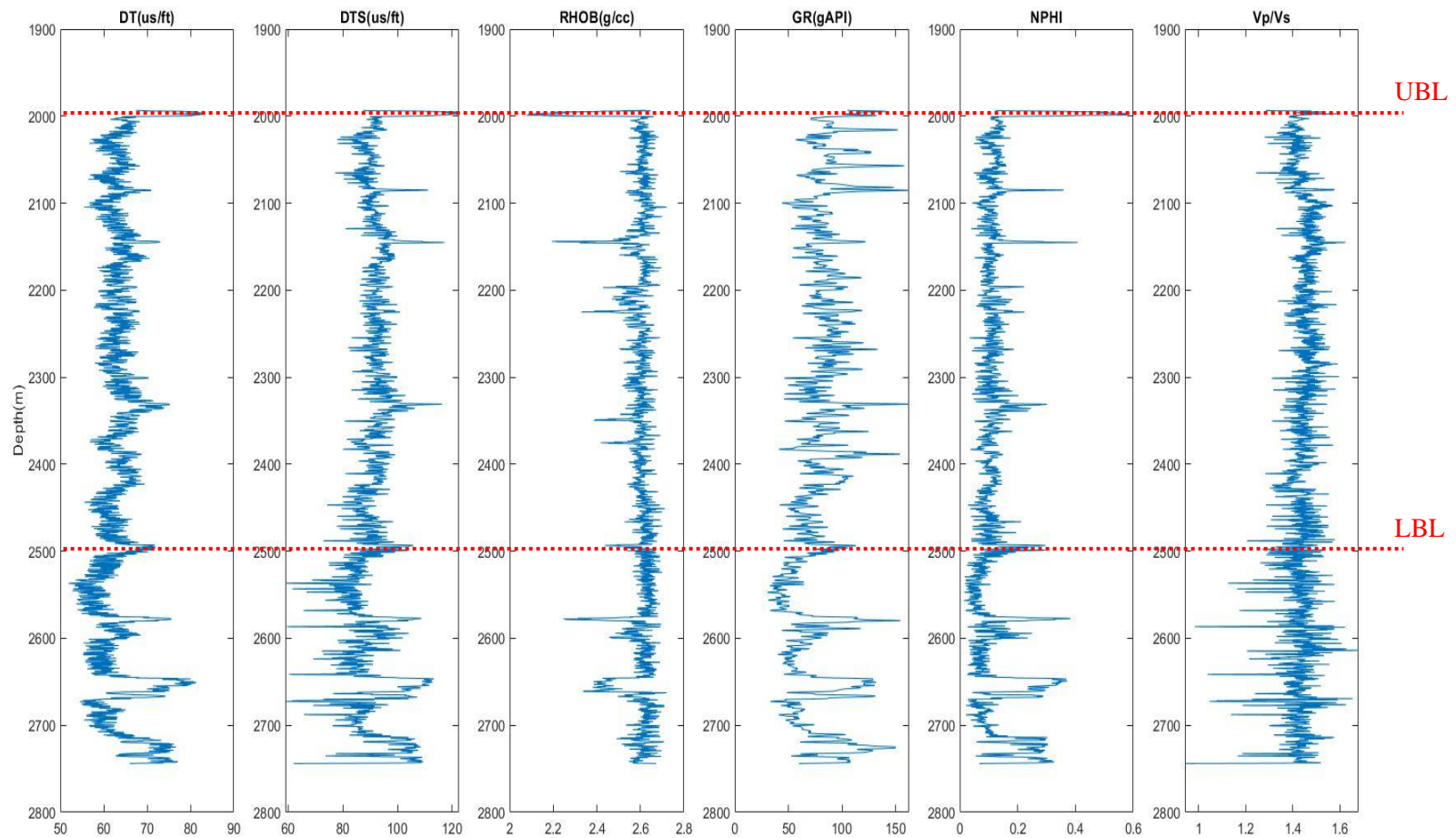


Figure 3-5: PH-1 well logs (only for the Bowland Shale Formation). The formation tops' markers are represented by the red, dashed lines labeled with the abbreviated formation names. UBL is the Upper Bowland Shale Formation, and LBL represents the Lower Bowland Formation.

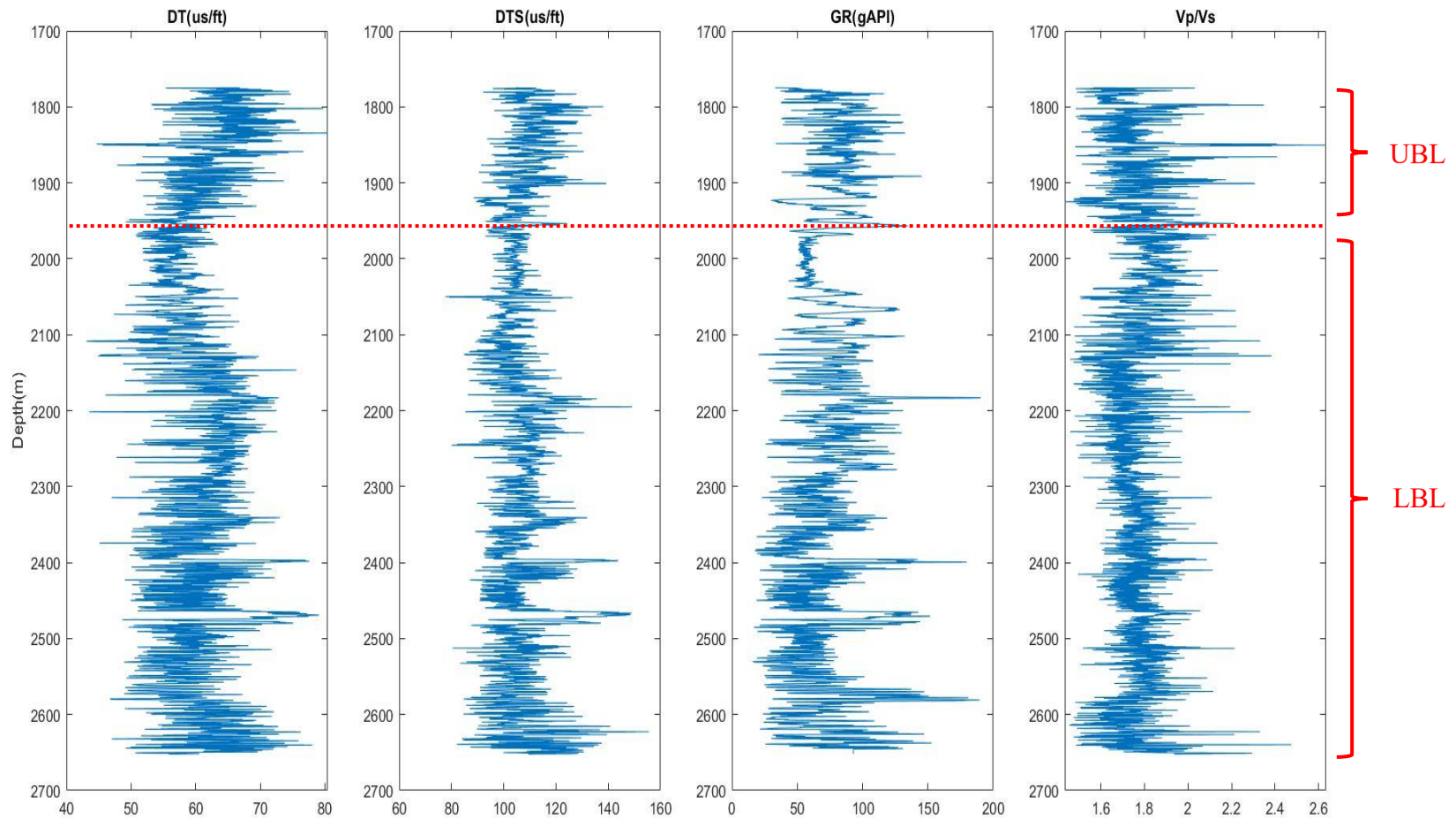


Figure 3-6: PNR-1 well logs. The formation tops' markers are represented by the red, dashed lines labeled with the abbreviated formation names. UBL is the Upper Bowland Shale Formation, and LBL represents the Lower Bowland Formation.

Chapter 4: Seismic Interpretation

This chapter explains the seismic interpretation method and show the result of the fault investigation and regional investigation. This includes the explanations of the fault and horizon picking method, the verification technique, the results and observations of the fault mapping, and the regional interpretations.

4.1 Fault Investigation Method

The seismic interpretation of the Bowland Shale in this study started by investigating faults in this region. In this study, faults that cause obvious offsets in the 3D reflections seismic data are tracked using the fault tracking feature in the OpendTect program. Not every fault is tracked in this study, especially, smaller ones that cause little offsets since it would take too much time to track them all. Figure 4-1 explains the fault mapping process used in this study. I identified offsets caused by faults on the 2D cross-sections of the seismic cube. These offsets were tracked by manually picking tracking seeds on the offset. Then, the same offset was tracked on different 2D cross-sections. The spatial spacing of the 2D cross-sections is 10 m but can decrease to 5 m if the fault has complicated shapes and orientations. These seed points were connected, mapping the faults. For each fault plane, I calculated the strike, dip angle, length of the fault plane, and the depth extent (Table 4-1). These calculations were done by solving the three-point problem on MATLAB. Firstly, coordinates of seeding points of each fault were converted from time to depth using the velocity of each layer calculated from the formation tops information from the PH-1 well log. Then, the average fault plane was calculated for each fault using the linear regression algorithm. After that, the coordinates of 3 points on the average fault plane are used to calculate strike and dip using the 3D geometry.

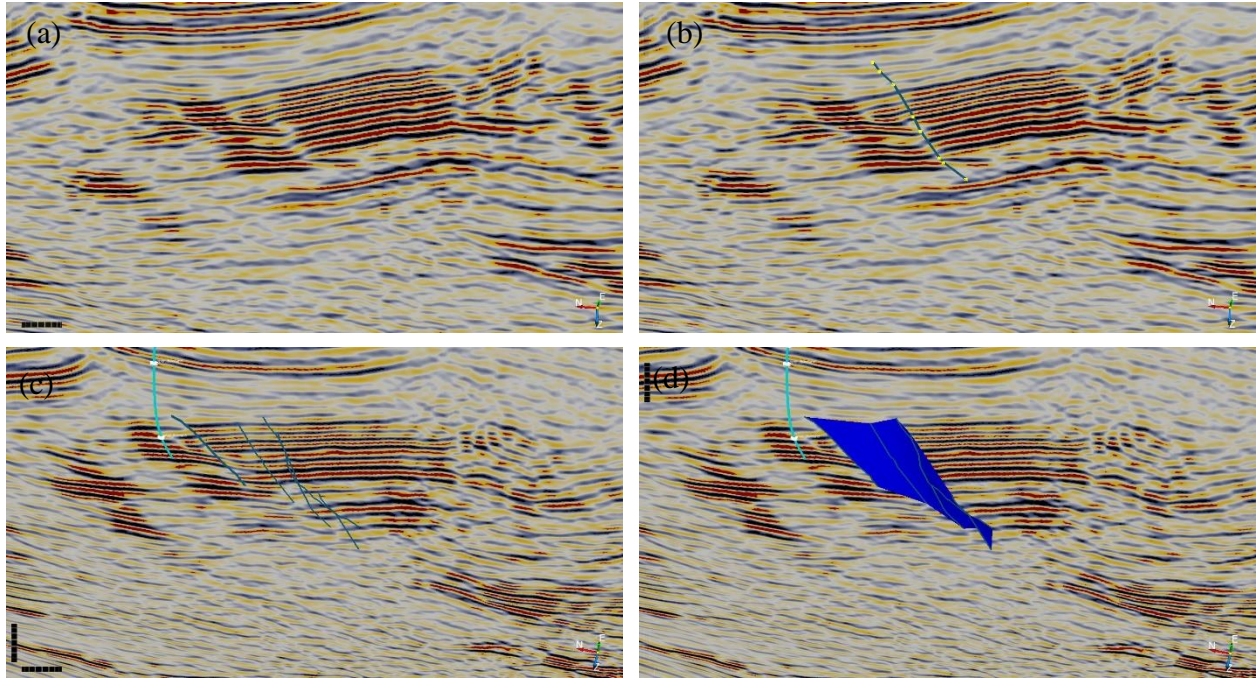


Figure 4-1: The fault tracking process. (a) The vertical cross-section of the 3D reflection seismic data cube was used to observe the offsets (horizon discontinuity) created by the faults. (b) Tracking seeds were picked on one of the offsets. (c) The same fault was tracked on different vertical slices. (d) The tracking seeds were connected into a modelled fault, represented by the blue object.

4.2 The Key Horizons Tracking

The key horizons were mapped by using well log data and other calibration information available from the PH-1 well. A synthetic seismic trace was generated from the PH-1 sonic log and bulk density data (Figure 4-2) with a zero-phase wavelet (Figure 4-3) as the source. This enabled the identification of key horizons to be tracked within the seismic cube, including the Manchester Marl, Namurian Rough Rock, and Upper and Lower Bowland Shale (Figure 4-5). The Manchester Marl was picked because it has strong reflections and it is located right above the Variscan Unconformity. The Namurian Rough Rock marks the upper boundary of the

Millstone Grit Group. The Upper and Lower Bowland Shale are the target zones for production and fault interpretation.

The tracking process is shown in Figure 4-4. Seeding points were manually picked on the key horizons on a 2D cross-section, starting from a well track with formation tops' locations such as the PH-1 well track. By the application of the semi-auto tracking feature of the OpendTect program, the signals at the seeding locations were compared with signals of the surrounding area by using the cross-correlation method with the compare window of -40 to 40 ms and the correlation threshold of 80%. The program, then, automatically track the horizons across the volume. However, if there are regions where cross-correlation coefficients dropped below the specific threshold, additional seeding points were manually picked on different 2D cross-sections, allowing the program to automatically track further. This process continued until the horizons had been mapped across the 3D reflection seismic data. In addition, other well tracks (Thistleton-1 (TH-1) and Grange Hill (GH-1)) were used to verify the picked horizons since they also contain the locations of horizon tops. The other verification method applied to each picked horizon is the “completing a four” technique. This was achieved by tracking the same horizon in a square-shaped loop using 4 cross-sections to see if the beginning and the end seeding points are the same, as shown in Figure 4-6.

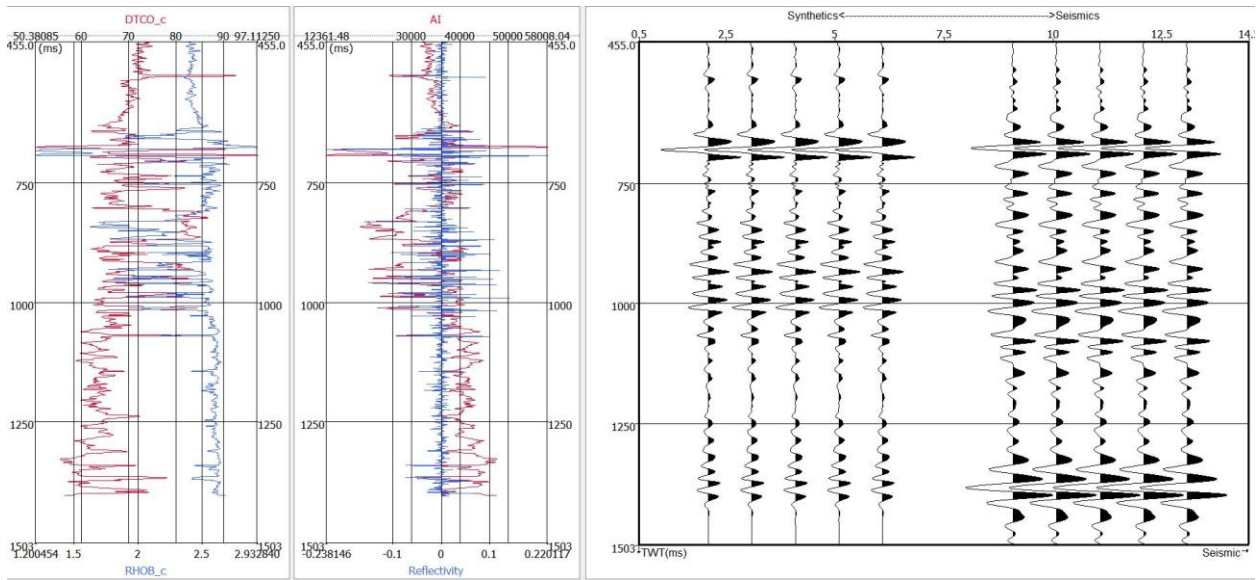


Figure 4-2: Well-to-seismic calibration. The left log shows the sonic (red) and bulk density (blue) data. The middle log shows the acoustic impedance (red) and reflectivity (blue) data. The right log was used to compare the synthetic reflections to the actual seismic data for the calibration.

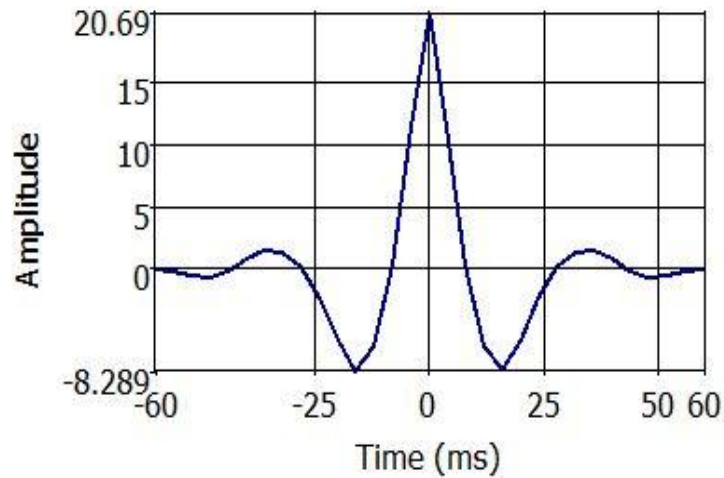


Figure 4-3: The wavelet used to create the synthetic data in well-to-seismic calibration.

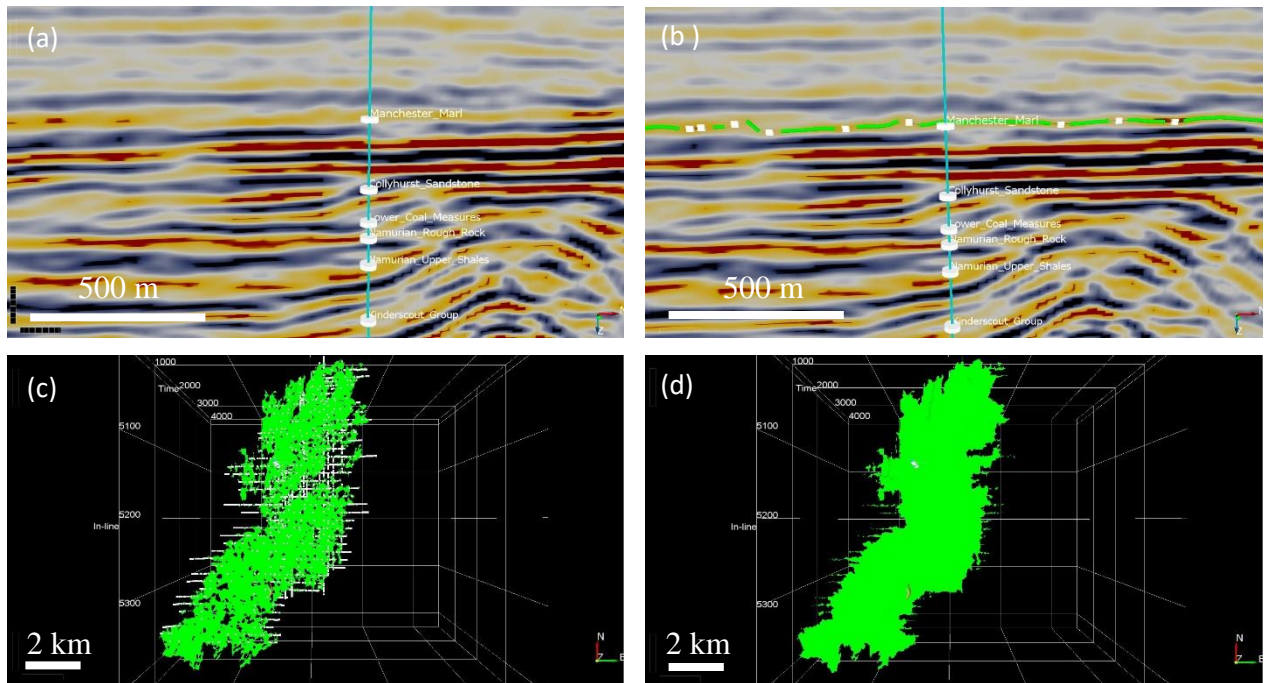


Figure 4-4: Process of tracking horizons. (a) A vertical cross-section of the 3D seismic data was taken. (b) Tracking seeds (white dots) were manually picked on the Manchester Marl horizon. (c) The map-view figure showing the auto-tracking feature of OpendTect which was used to track the horizon (green area) using the information at the seed locations. (d) The gridding technique was applied to the tracked horizon, filling the holes and making the horizon smoother.

The gridding feature of the OpendTect program was utilized to interpolate and fill the holes, or areas that the semi-automatic horizon tracking tool cannot track, on the picked horizons, and to smoothen these surfaces. In this study, I used the Continuous Curvature algorithm which interpolates the data with the continuous second derivatives of the surface's topography. This results in smooth horizons, which can be utilized as the foundation of the further analysis.

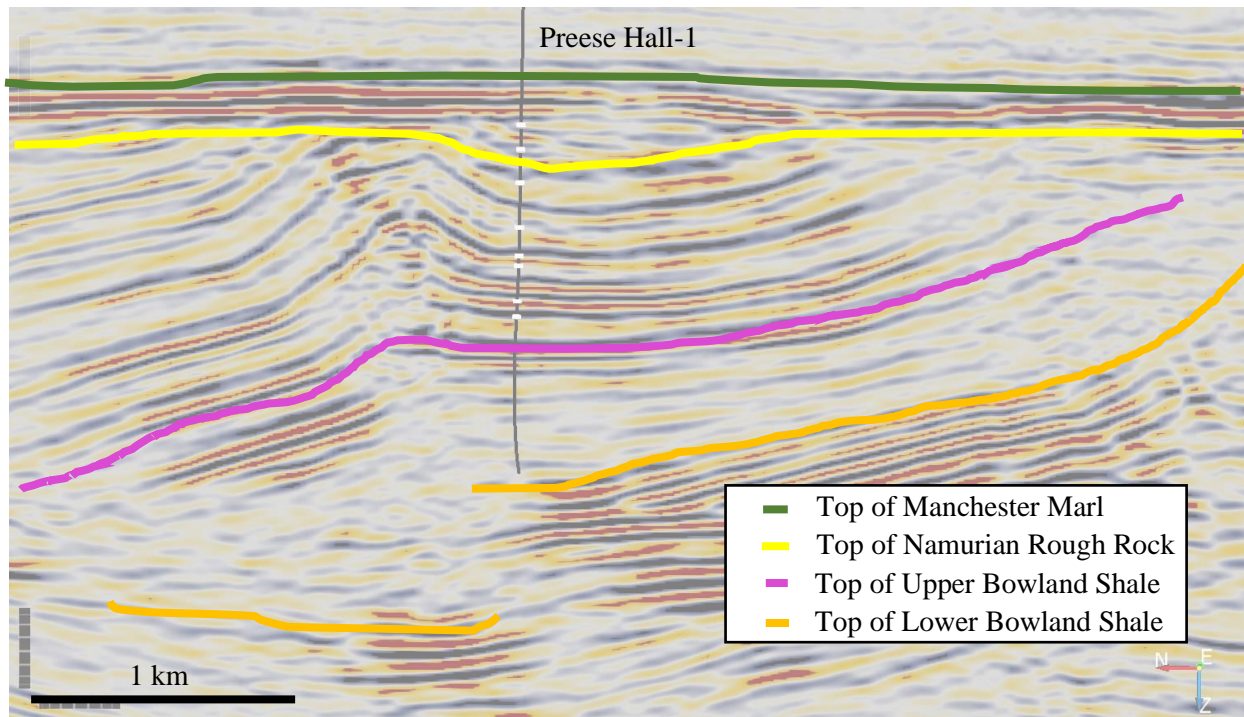


Figure 4-5: Key horizons that were picked in this study. These include the top of the Manchester Marl, top of the Namurian Rough Rock (top of the Milstone Grit Group), top of the Upper Bowland Shale and top of the Lower Bowland Shale.

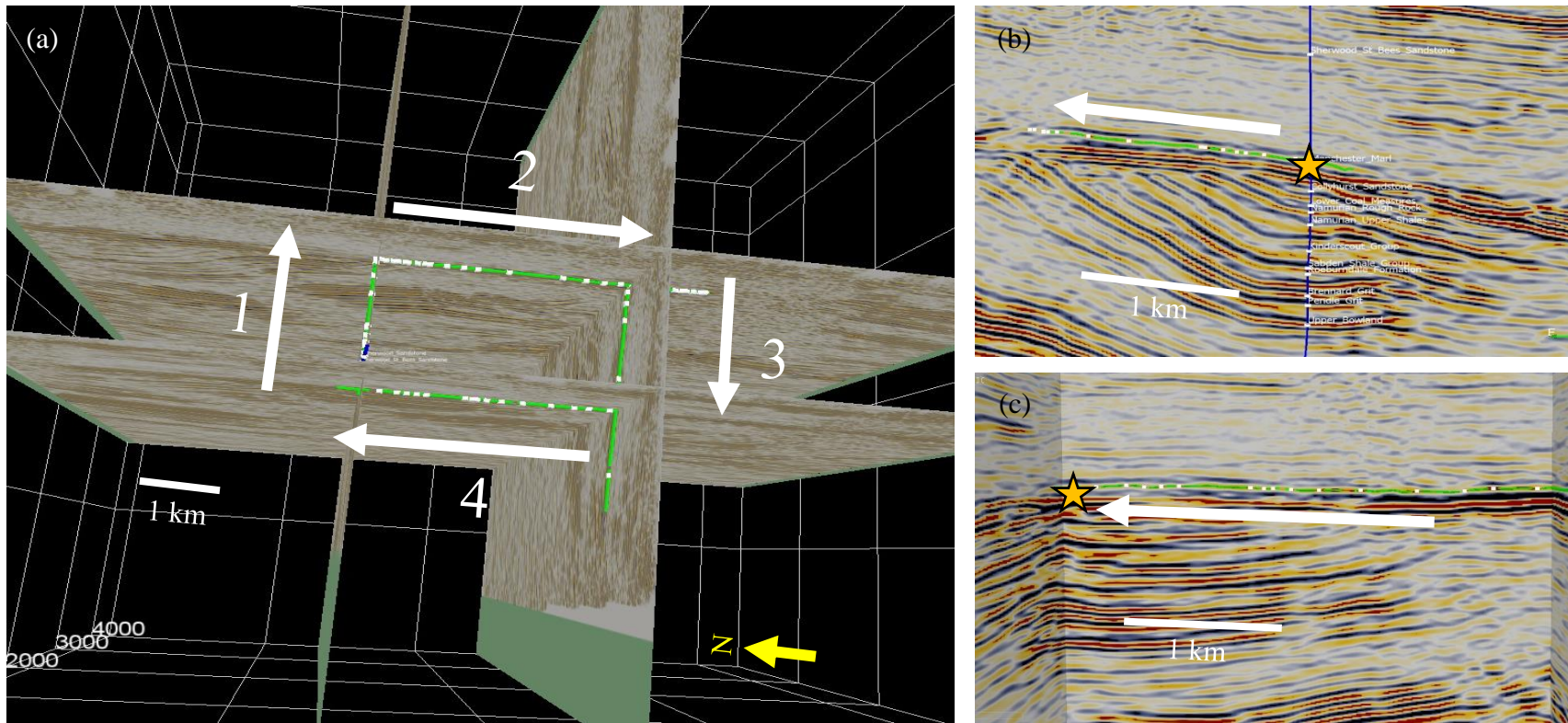


Figure 4-6: An example of the “completing a four” technique for verifying the picking of the Manchester Marl horizon. (a) the Manchester Marl Formation was tracked in a rectangular loop, starting at the PH-1 well (blue line) and following the arrows in order (1 to 4). (b) the horizon tracking across the cross-section 1. (c) the horizon tracking across the cross-section 4. (c) shows that the starting point (marked by the yellow star) is the same as the ending point. Thus, this verifies the Manchester Marl horizon tracking. The white arrows represent the direction of the tracking. The green lines are the tracking of the Manchester Marl. The white dots are the seeding points.

4.3 Fault Mapping Results and Observations

As a result, the total of 41 faults were mapped and studied in this thesis (Figure 4-7, 4-8, and Table 4-1). Most of the faults strike in the NE-SW direction, indicating a maximum horizontal stress acting mostly in the NW-SE direction at the time of formation. This indicates the change in the maximum horizontal stress direction later in the geological history since the present direction is almost N-S (Clarke et al., 2014). I have divided them into 2 groups based on their senses of motion. The first group consists of thrust faults with the typical length of 1-2 km, and depth extent of around 1-3 km. They are found from the Lower Bowland Shale to the Manchester Marl, but generally do not cut through the Variscan unconformity. This suggests that they are relatively older faults that were generated before or during the Variscan Orogeny in the Late Devonian-Carboniferous (Mississippian). The second group consists normal faults that were generated by Carboniferous rifting, thermal subsidence during the Pennsylvanian, and basin subsidence in Permian-Triassic (Anderson et al., 2020). They can reach up through the Variscan unconformity (~1.2 km depth near the PNR site), as well as below the base of Lower Bowland Shale (~2.2-3.0 km depth near the PNR site). They can reach 6-7 km in terms of the depth and 6-7 km in length.

Furthermore, there are several larger fracture zones oriented NE-SW and ENE-WSW as displayed in Figure 4-7. These are larger than the previous groups of faults, with length and depth extent of around 3-8 km and 4-8 km. The presence of these fault networks complicates the reflection seismic data as they are the chaotic areas with weak reflections. These faulting zones consist of smaller pieces and chunks of broken or heavily deformed horizons, which generate both constructive and destructive interferences of signals. This results in the inconsistency of the

signal strength of the data in these zones. Most of the fracture zones are located in the south-eastern part of the data cube, though there are a few in the north-western part as well.

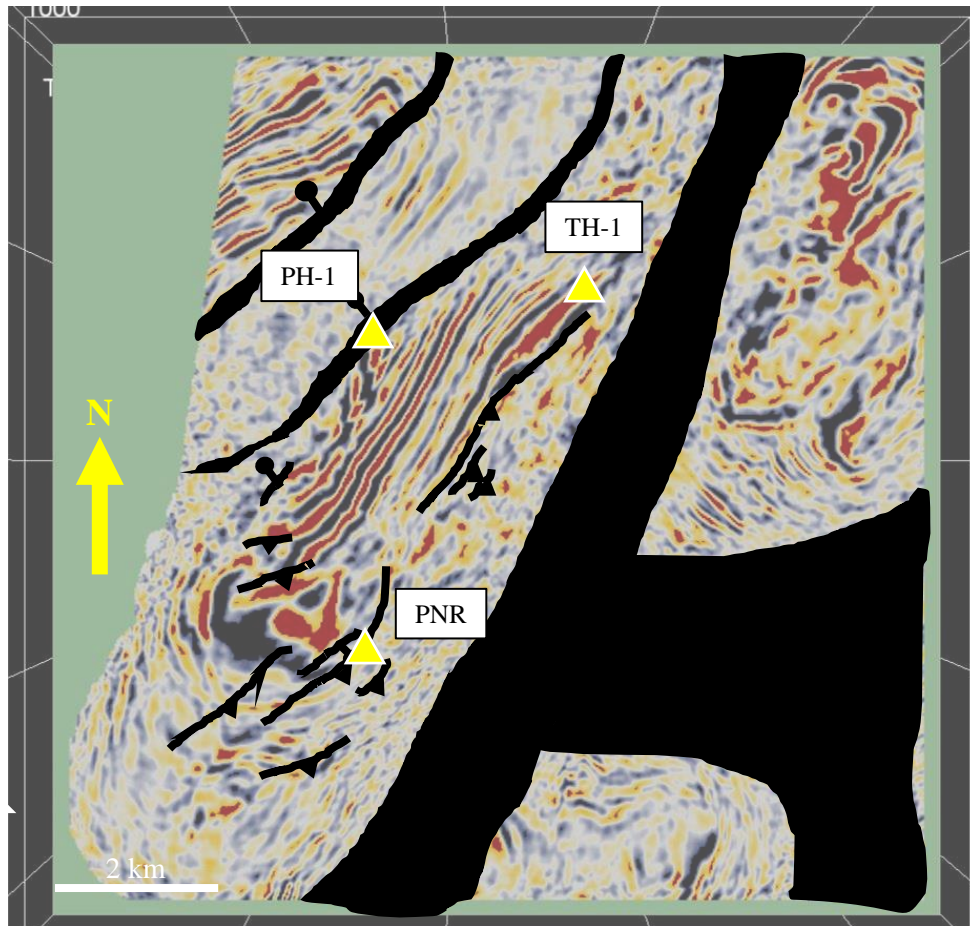


Figure 4-7: The locations of the faults tracked in this study in map-view (time slice at 1,340 ms or 2.54 km depth). The dark lines represent the picked faults, while the dark bands are the large fault systems. The yellow triangles represent the well locations.

Table 4-1: the strike, dip, size, and sense of motion of faults identified in the 3D reflection seismic data. Fault number 1-9 are the borders of the fault networks.

Fault number	Strike (deg)	Dip (deg)	Length in map-view (m)	Depth Extent (m)	Sense of motion
1	34.0	74.0	6865.5	8620.9	thrust
2	34.1	62.7	5644.4	6069.8	thrust
3	40.7	68.0	4233.9	6979.5	thrust
4	29.7	65.4	3246.5	4773.8	thrust
5	48.2	57.4	5756.4	5299.5	thrust
6	18.8	40.4	7961.9	4766.6	thrust
7	34.2	50.2	8223.1	4319.4	thrust
8	184.0	60.2	1892.0	3632.8	normal
9	196.1	71.9	1591.0	4053.9	normal
10	202.9	78.1	368.8	1131.6	thrust
11	30.7	57.6	1003.0	1234.9	thrust
12	38.3	69.6	748.0	1037.3	thrust
13	42.9	71.6	1588.1	1037.5	normal
14	28.8	62.4	1210.8	1013.7	thrust
15	9.4	83.8	318.8	2373.8	normal
16	40.1	79.8	1091.8	2911.3	normal
17	41.6	74.3	695.6	1073.4	normal
18	231.9	47.3	7396.9	7665.4	normal
19	234.1	61.2	6828.1	6775.8	normal
20	206.8	55.0	1956.3	1835.3	thrust
21	176.2	60.6	849.6	1768.5	thrust
22	221.3	64.4	1582.5	2395.1	normal
23	41.5	73.2	1024.7	1638.8	normal
24	29.1	65.2	1504.0	1712.3	normal
25	54.3	69.6	1440.3	1861.8	thrust
26	56.0	72.0	1027.3	1528.1	thrust
27	34.8	77.9	1988.6	2774.5	thrust
28	31.6	61.8	1574.4	935.6	thrust
29	26.6	75.4	1095.1	2367.7	normal
30	3.2	66.6	938.6	2107.7	normal
31	214.4	80.0	1615.4	3980.2	normal
32	68.9	69.9	1180.4	3015.9	normal
33	69.7	74.1	1597.1	3816.6	thrust
34	235.2	61.3	770.2	962.6	normal
35	300.3	65.9	1294.4	2694.7	normal
36	75.2	39.9	3402.9	4091.8	thrust
37	60.5	55.1	2529.3	3539.6	thrust
38	66.7	42.0	2240.4	2630.9	thrust
39	52.0	73.8	1893.8	3691.0	thrust
40	66.8	60.9	1686.4	2669.7	thrust

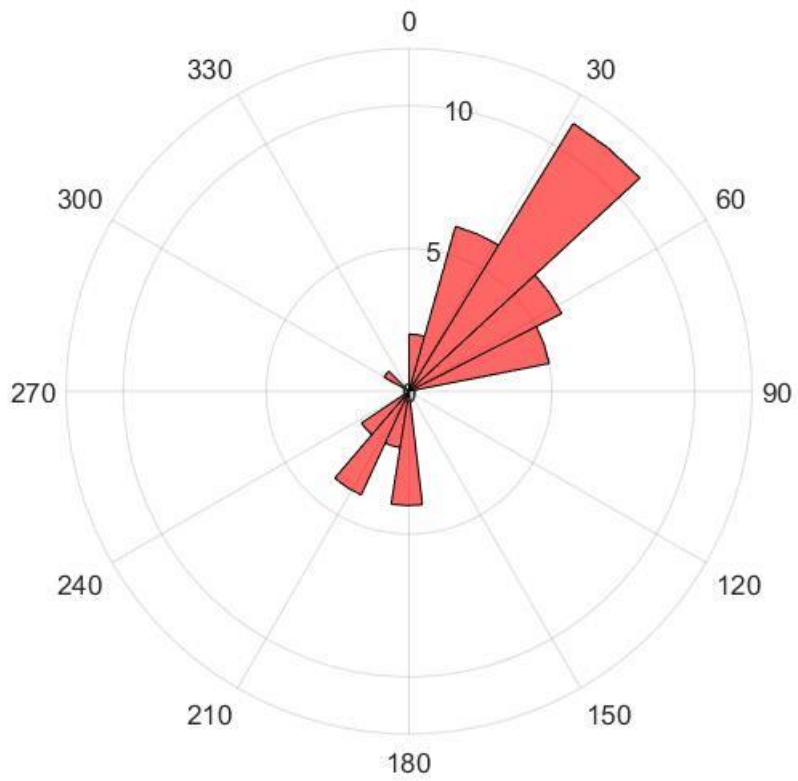


Figure 4-8: Polar histogram (rose-diagram) of strike directions of the picked faults in azimuthal system.

4.4 Regional Seismic Interpretation

The fault investigation process started with the generation of cross-sections across the 3D reflection seismic data cube. Figure 4-10 to 4-13 show cross-sections through the 3D reflection seismic data cube with Figure 4-9 as the locations of the cross-sections in map-view. The locations of the cross-sections A, B, and C were obtained by connecting the PH-1, GH-1, and PNR wells to each other since they contain the formation top locations. The location of the cross-section D was selected in order to provide the data of the southern areas where the cross-sections A, B, and C do not reach. As described in Chapter 2, there are numerous features associated with deformation from the rifting during Devonian and Carboniferous and compression during the Variscan Orogeny. The Variscan unconformity can be observed in the figures as a relatively flat boundary against which formations such as the Upper Bowland Shale, Lower Bowland Shale, Worston Shale Group, and many deformational features within these formations, are truncated. Figure 4-14 shows that the reactivated faults are not visible in the 3D reflection seismic data, as there is no offset near the estimated fault planes by Clarke et al. (2019) and Kettlety et al. (2020). The lack of any signs of the reactivated faults motivates the applications of the seismic attributes.

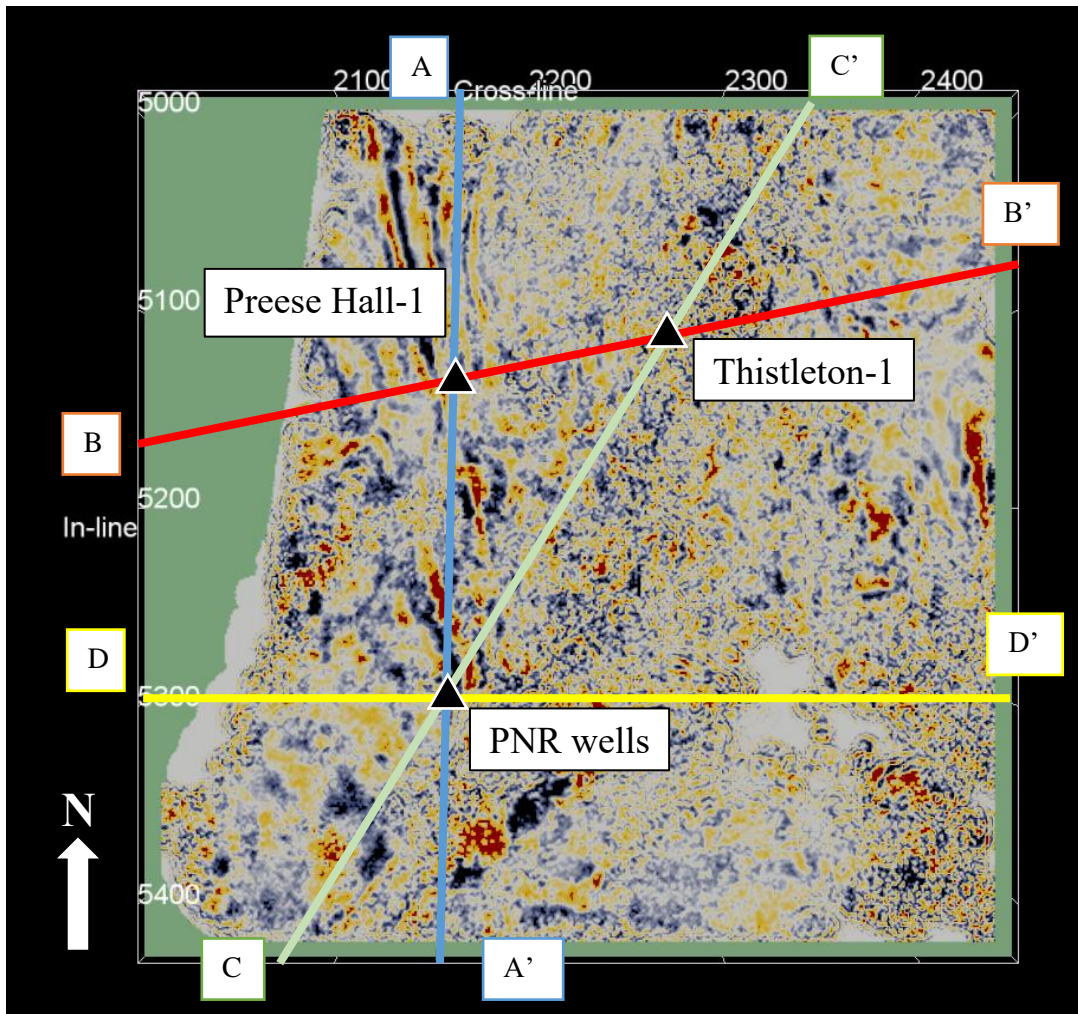
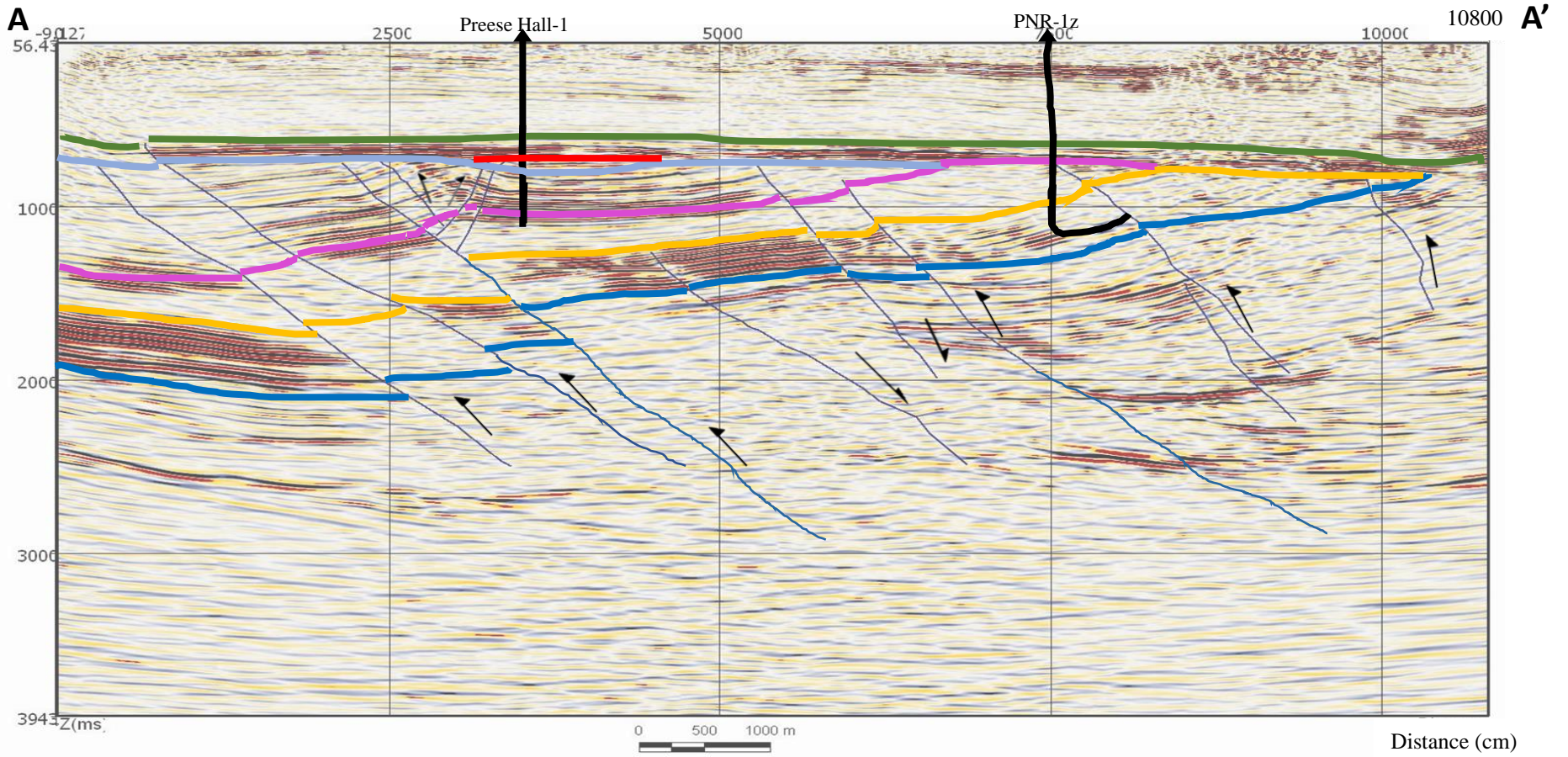


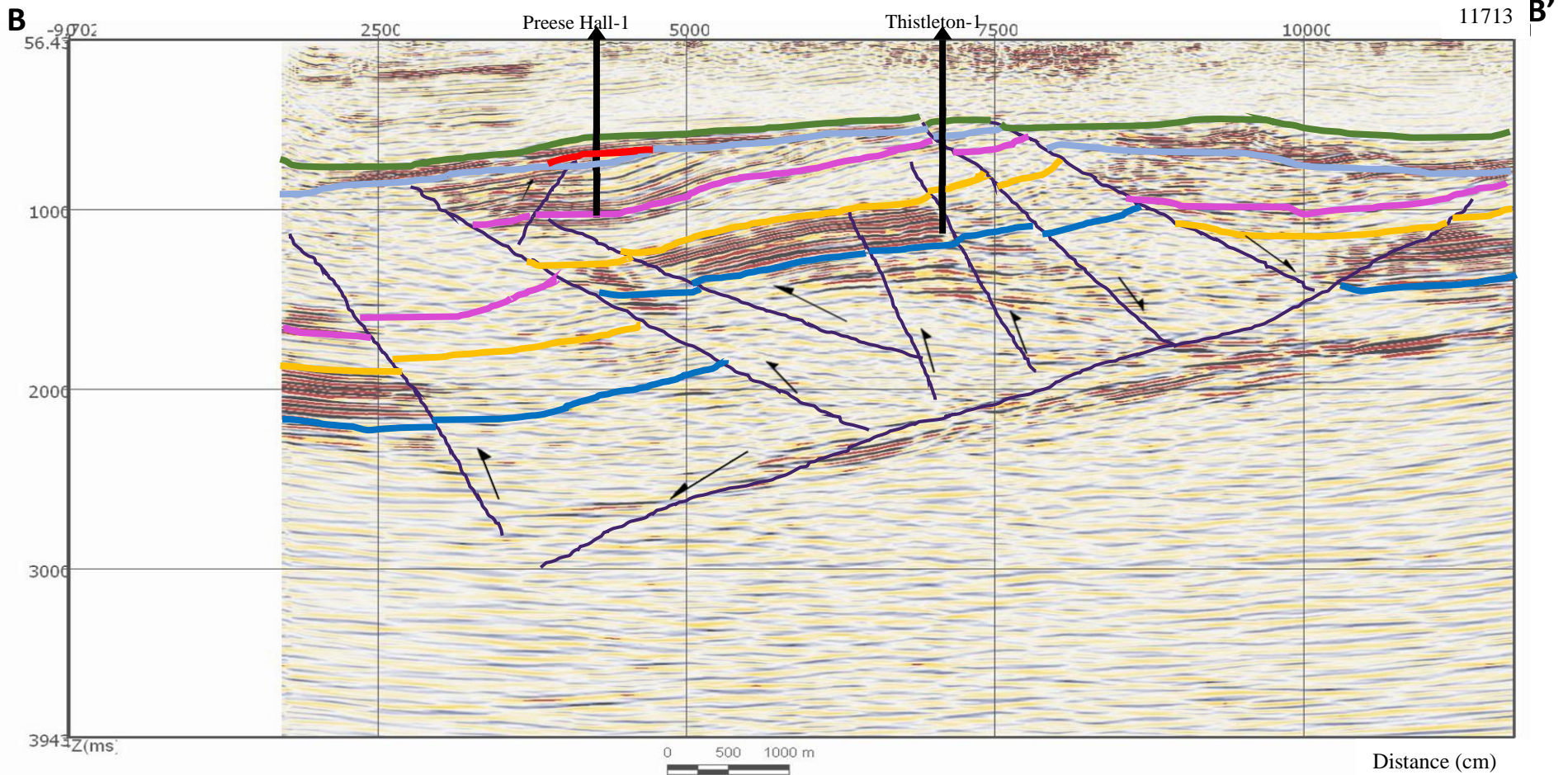
Figure 4-9: 3D reflection seismic data in map-view in OpendTect program. Blue, red, light green and yellow lines represent the locations of the vertical cross-sections in Figure 4-10 to 4-13. The black triangles represent the locations of the wells.

Figure 4-10: cross-section of the 3D reflection seismic data from PH-1 well to PNR-1z well



Legends			5.21
	Top of Manchester Marl		
	Top of Coal Measures Group		
	Top of Milstone Grit		
	Top of Upper Bowland Shale		
	Top of Lower Bowland Shale		
	Top of Worston Shale Group		-5.18

Figure 4-11: cross-section of the 3D reflection seismic data from PH-1 well to TH-1 well













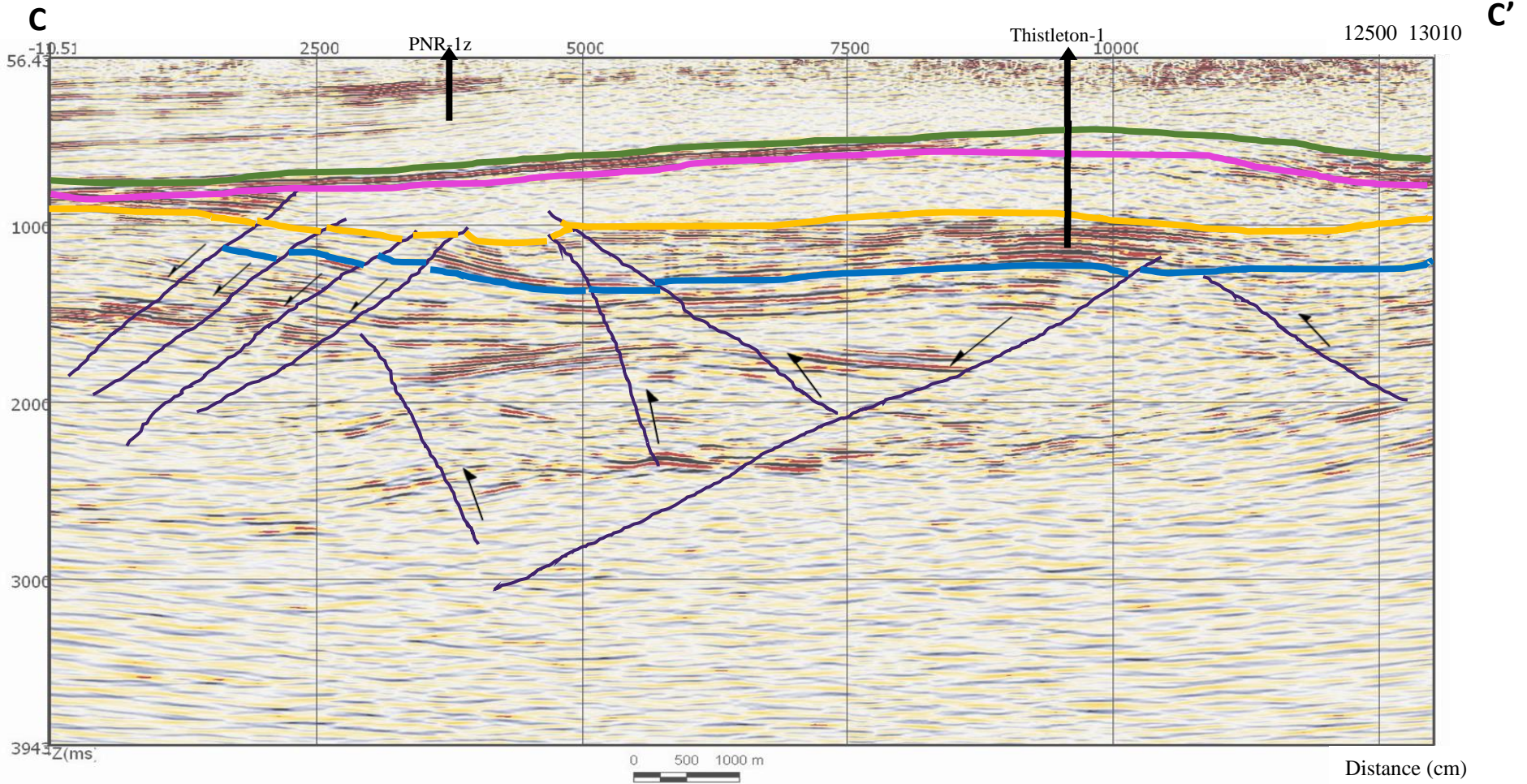
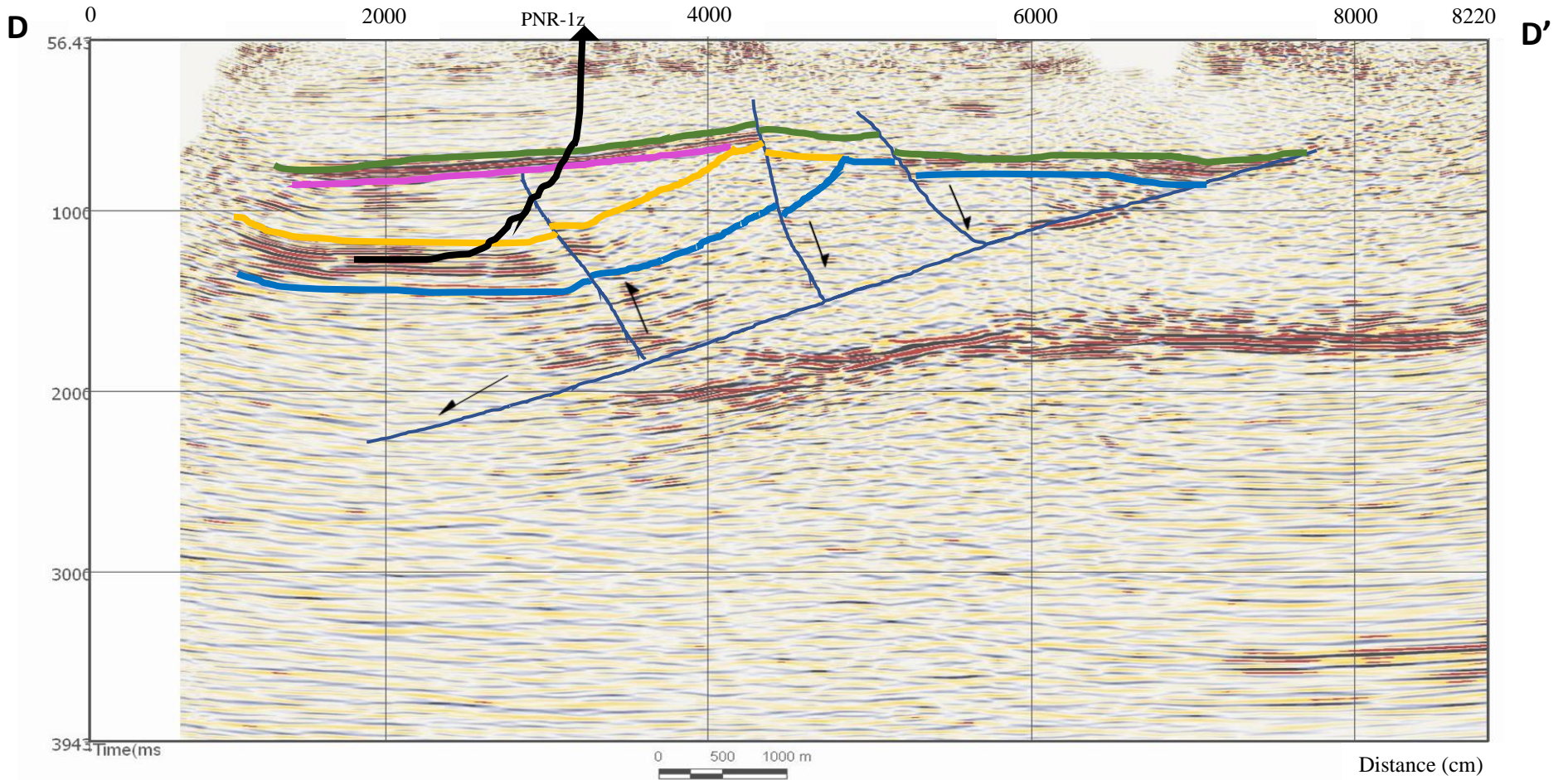
Legends		 Normal Fault  Thrust Fault  Well	
	Top of Manchester Marl		
	Top of Coal Measures Group		
	Top of Milstone Grit		
	Top of Upper Bowland Shale		
	Top of Lower Bowland Shale		
	Top of Worston Shale Group		

Figure 4-12: cross-section of the 3D reflection seismic data from PNR-1z well to TH-1 well



Legends				5.21	
	Top of Manchester Marl		Normal Fault		
	Top of Upper Bowland Shale		Thrust Fault		
	Top of Lower Bowland Shale		Well		
	Top of Worston Shale Group			-5.18	

Figure 4-13: cross-section of the 3D reflection seismic data across PNR-1z well in the E-W direction



Legends		
	Top of Manchester Marl	
	Top of Upper Bowland Shale	
	Top of Lower Bowland Shale	
	Top of Worston Shale Group	
		Normal Fault
		Thrust Fault
		Well

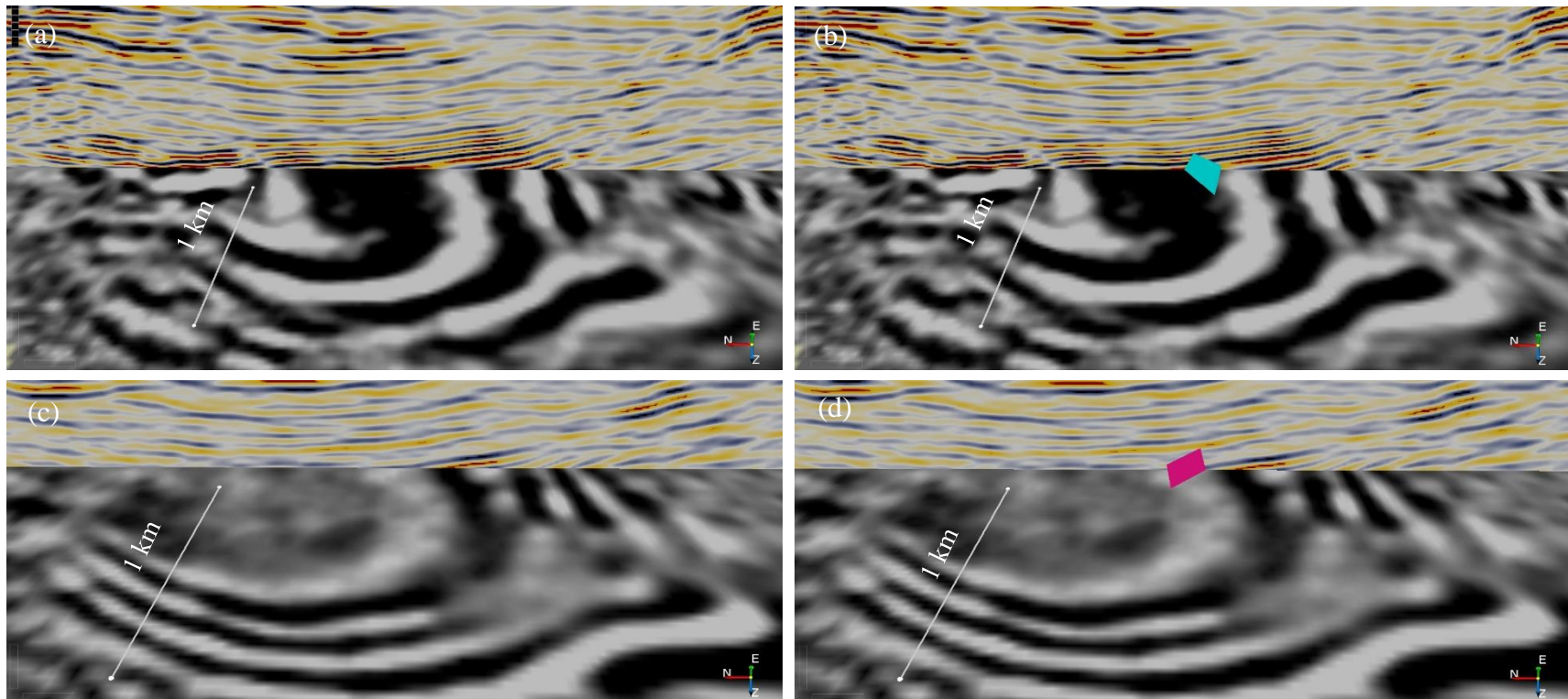


Figure 4-14: The causative faults in the 3D seismic data. Each figure shows the intersection between a vertical and horizontal cross-section of the 3D seismic data in different colour scheme (for better visibility). (a) and (b) illustrate the location of the causative fault at the PNR-1z well proposed by Clarke et al. (2019) (with and without the fault plane). (c) and (d) show the location of the causative fault at the PNR-2 well proposed by Kettlety et al. (2020) (with and without the fault plane). The cyan plane is the causative fault plane of the PNR-1z events established by Clarke et al. (2019). The pink plane represents the causative fault plane of the PNR-2 events established by Kettlety et al. (2020).

Chapter 5: The Reactivated Fault Investigation Using the Seismic Attributes

This chapter explores the application of seismic attributes in the reactivated fault investigation at the PNR wells. This chapter provides the results, observations, and discussion from the investigations using the similarity, spectral decomposition, and curvature attributes on the Bowland Shale.

5.1 The Results and Observations of the Fault Investigation Using the Seismic Attributes

5.1.1 Similarity

Figure 5-1 illustrates the efficiency of similarity attribute applied to a time-slice for highlighting smaller faults or other features causing dissimilarity (represented by dark lines) that are harder to detect in the raw 3D seismic data. These dark lines tend to run in the NE-SW direction, indicating that the maximum stress direction is NW-SE. It also illustrates the fracture zones, which are represented by areas with chaotic orientations of dark lines (blue polygons). The dark lines within these zones are relatively shorter and are not oriented in a certain direction. Moreover, the similarity attribute also picks up the faults that are produced during the formation of the anticline in the upper, middle section of the figure (yellow polygon). They have very similar orientations and are located close to each other, orderly forming a cluster. The area around the PNR wells have relatively brighter colour, implying that there are lesser number of faults in the region. This means that drilling in this area has lesser chance to produce felt seismicity. Figure 5-2 and 5-3 are also the horizontal time slices which run through PNR-1z and PNR-2 event clusters in order to identify the causative faults. However, they did not show any presences of faults or geological features near the event clusters as there are no black lines in those areas.

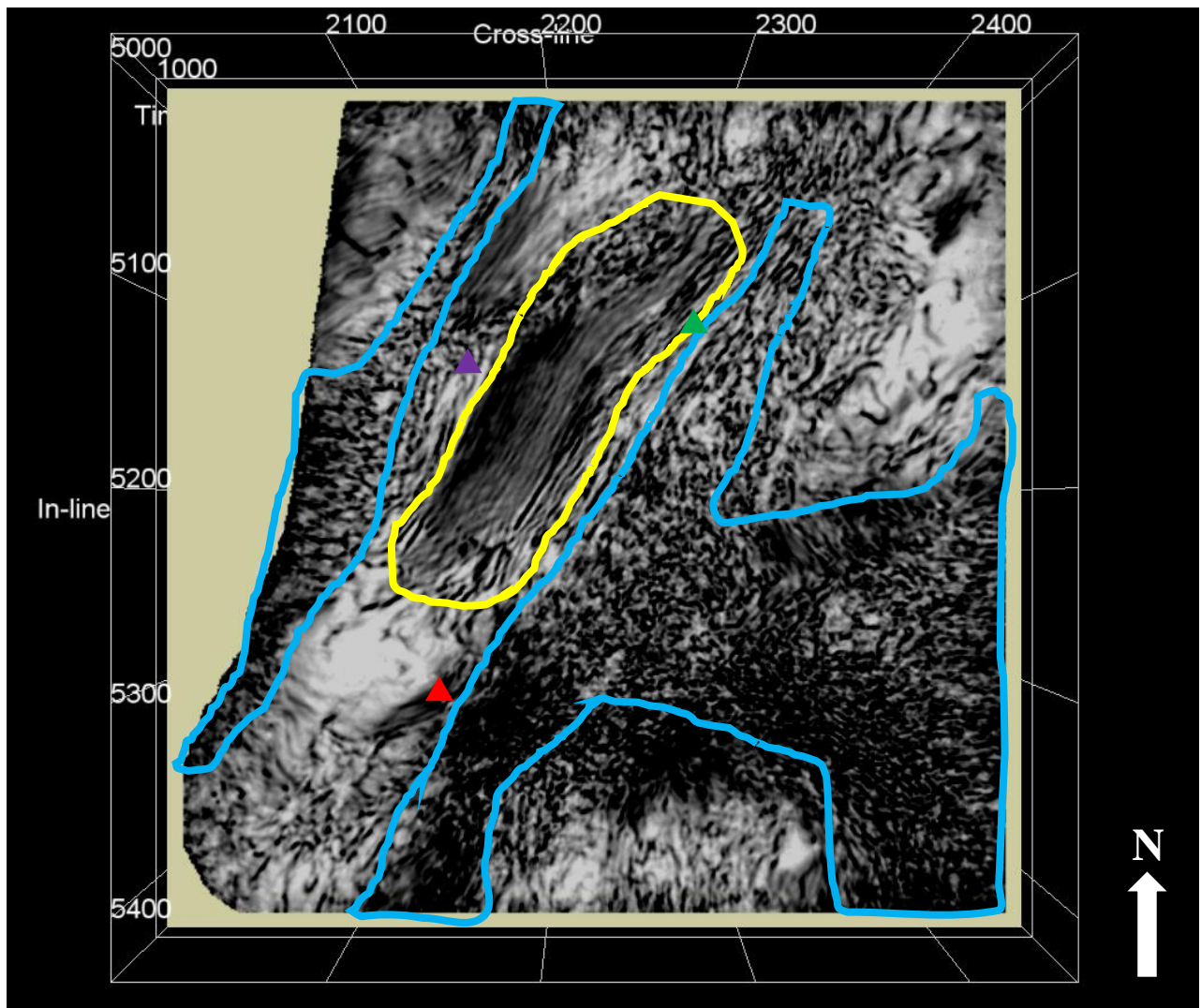


Figure 5-1: Similarity attribute applied on the time slice at 1,270 ms (2,366 m). Lighter areas have high similarity values, while darker areas have less. Faults in this region are marked by dark lines. The yellow polygon represents the faults generated at the anticline, while the blue polygons are the fault networks. The purple, green, and red triangles represent the locations of the PH-1, TH-1, and PNR wells.

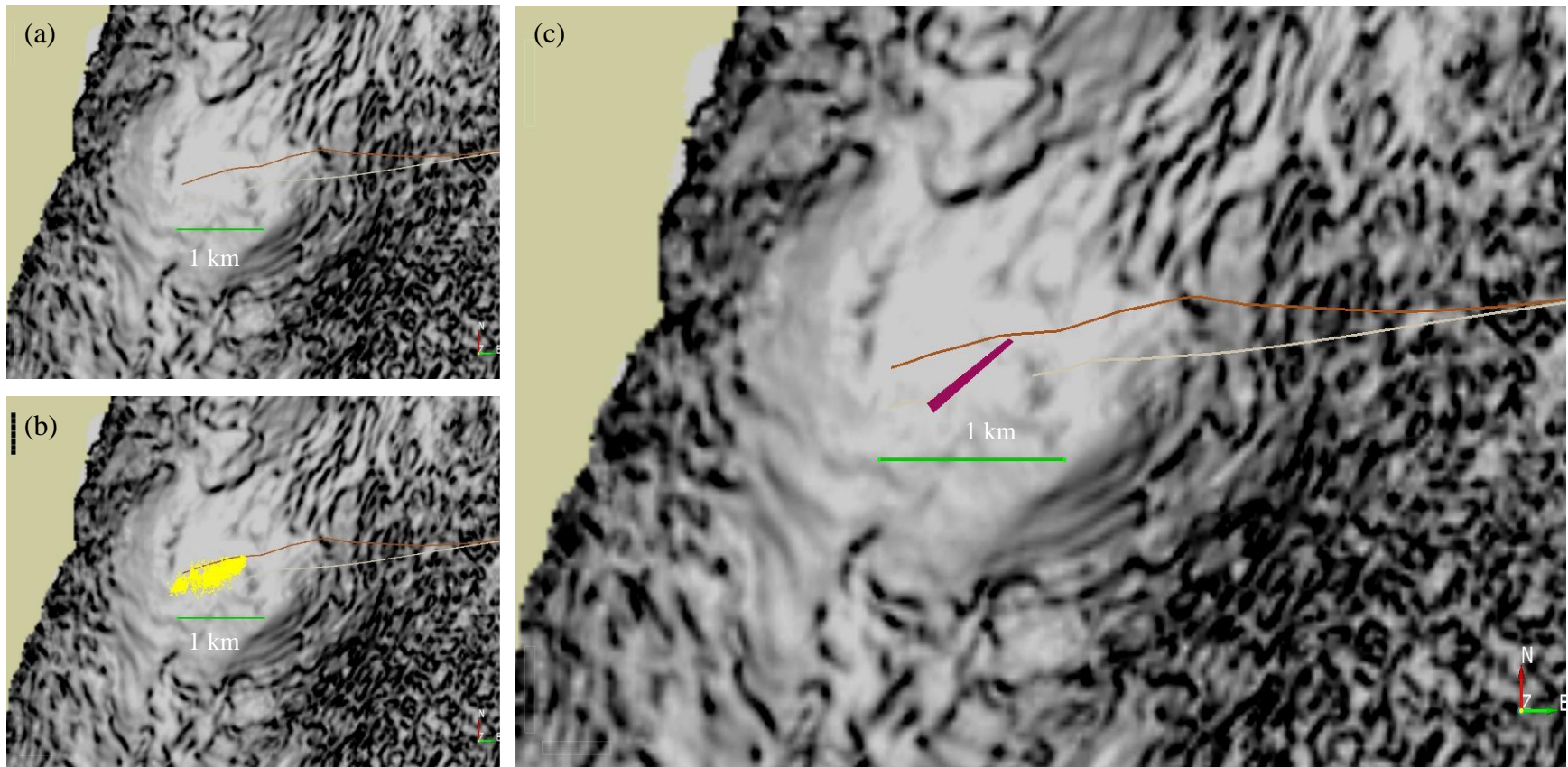


Figure 5-2: (a) Similarity attribute applied on the time slice at 1,260 ms (2,343 m). (b) Similarity attribute applied on the time slice at 1,260 ms (2,343 m) with the PNR-1z event locations (yellow dots). (c) Similarity attribute applied on the time slice at 1,260 ms (2,343 m) with the PNR-1z fault plane (pink plane) established by Clarke et al. (2019). The white line represents the PNR-1z well track, while the orange line represents the PNR-2 well track.

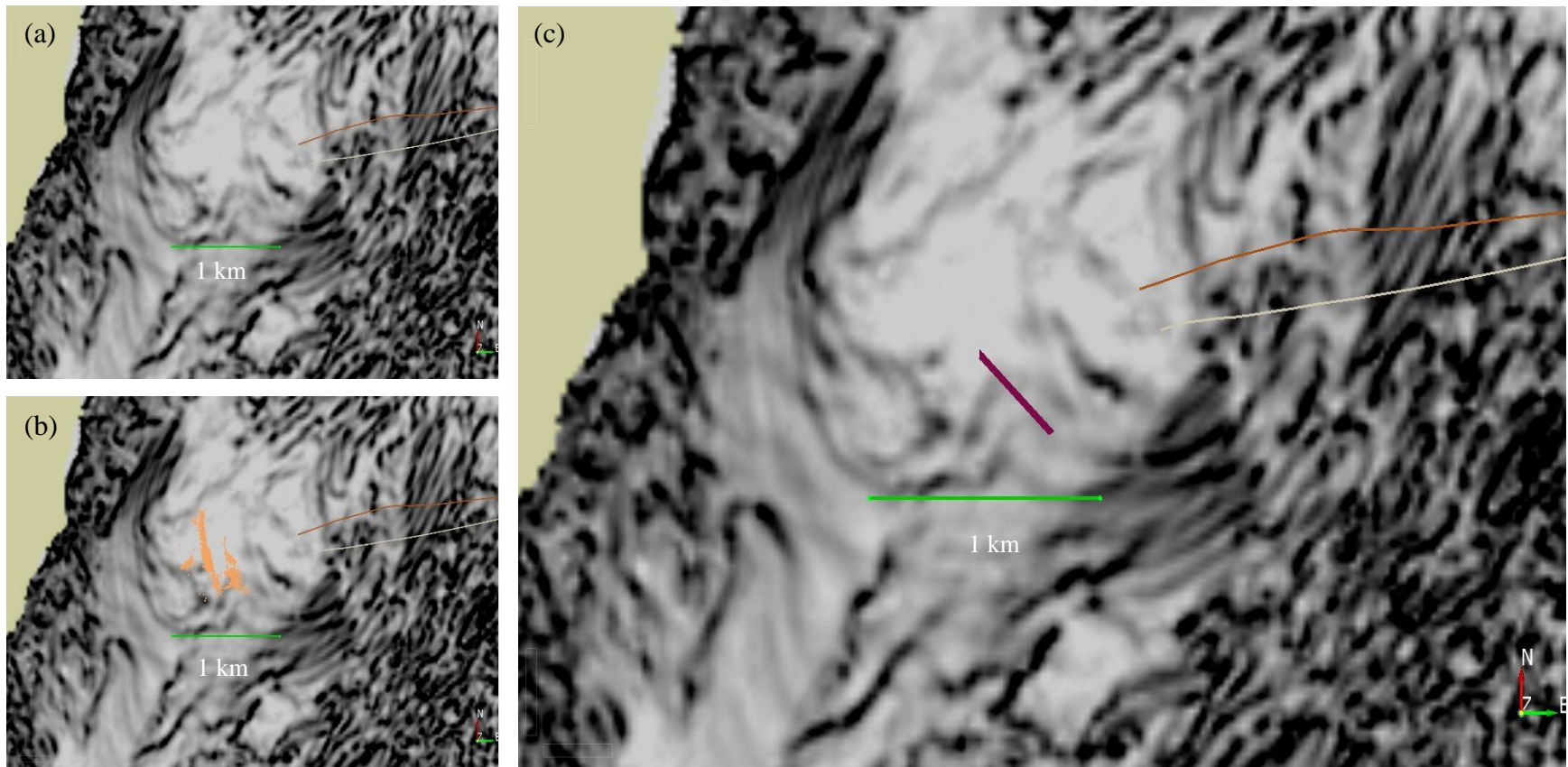


Figure 5-3: (a) Similarity attribute applied on the time slice at 1,180 ms (2,156 m). (b) Similarity attribute applied on the time slice at 1,180 ms (2,156 m) with the PNR-2 event locations (yellow dots). (c) Similarity attribute applied on the time slice at 1,180 ms (2,156 m) with the PNR-2 fault plane (pink plane) established by Kettlety et al. (2020). The white line represents the PNR-1z well track, while the orange line represents the PNR-2 well track.

Since no sign of the reactivated faults were clearly visible in Figure 5-1 to 5-3, I investigated attributes on 2 additional sub-horizons that I picked around the PNR site (Figure 5-4). These two sub-horizons are in the Upper Bowland Shale and the Lower Bowland Shale. These horizons run through the same depth as the PNR-1z and PNR-2 event clusters; thus, enabling more precise visualization of attributes at the depth where microseismicity occurred.

Figure 5-5 and 5-6 show similarity plotted on horizons picked near to the PNR-1z and PNR-2 event locations. This method highlights faults that were not previously visible on the raw 3D reflection seismic data. The similarity attribute on the picked horizons is also unable to reveal the reactivated faults at the PNR-1z as no features are seen in the same position and orientation of the actual faults detected by Clarke et al. (2019). However, Figure 5-6 shows that there are 2 dark lines (highlighted by the red, dashed box) which disappears at the similar position as the fault plane identified by Kettlety et al. (2020). This might be because the 2 dark lines, which represent geological features, are cut by the causative fault. Therefore, this might serve as an evidence of the reactivated fault at the PNR-2 well.

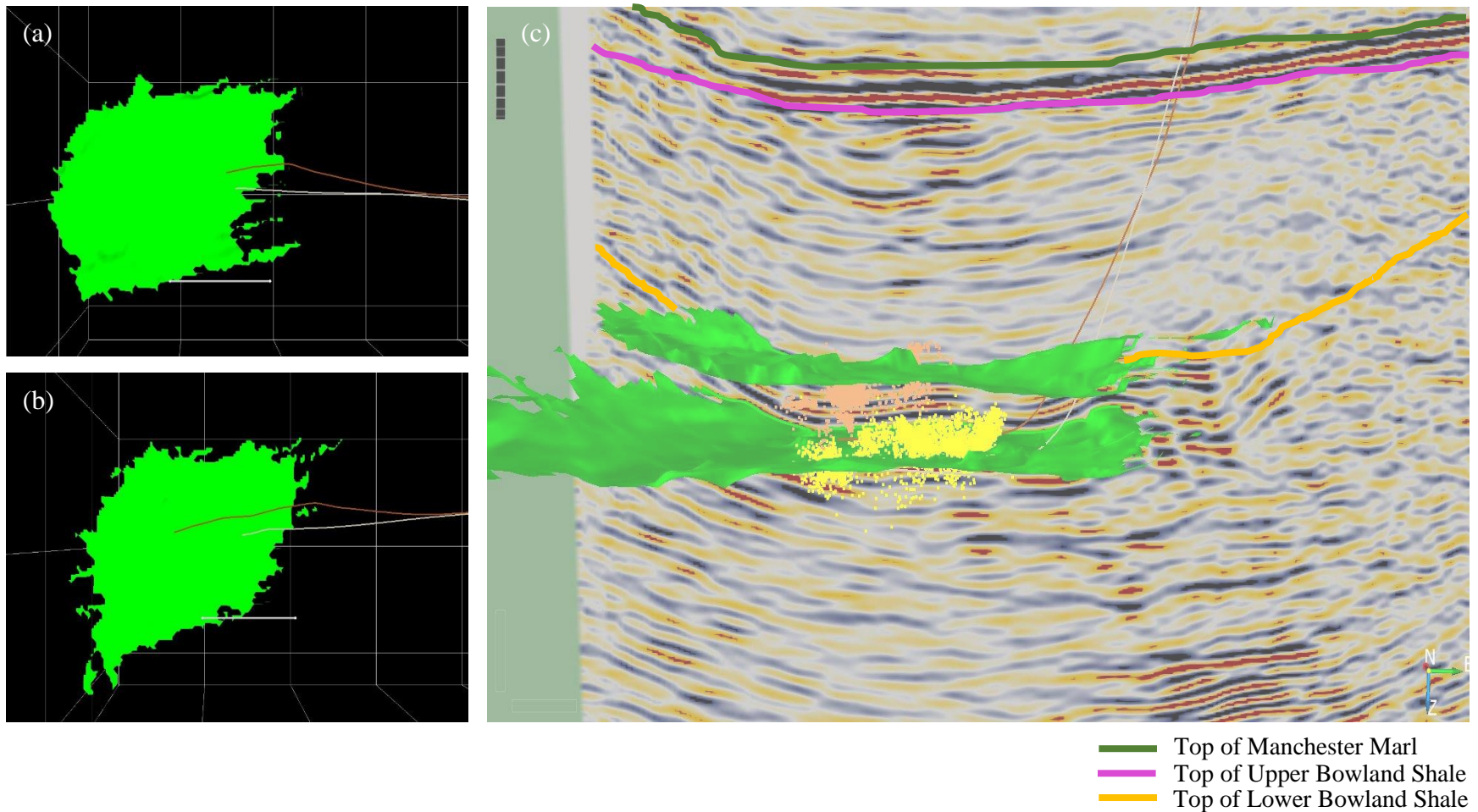


Figure 5-4: Additional horizons are picked near the PNR-1z and PNR-2 events. (a) The horizon near the PNR-1z events, located in the Lower Bowland Shale. (b) The horizon near the PNR-2 events, located in the Upper Bowland Shale. (c) The locations of both horizons regarding to the event locations (the upper horizon is (b) and the lower horizon is (a)). The yellow dots represent the locations of PNR-1z events, while the orange dots are the locations of PNR-2 events. The small white line represents the PNR-1z well track, while the small orange line is the PNR-2 well track. The top of Manchester Marl, Upper Bowland Shale and Lower Bowland Shale are represented by solid green, pink and orange lines in order.

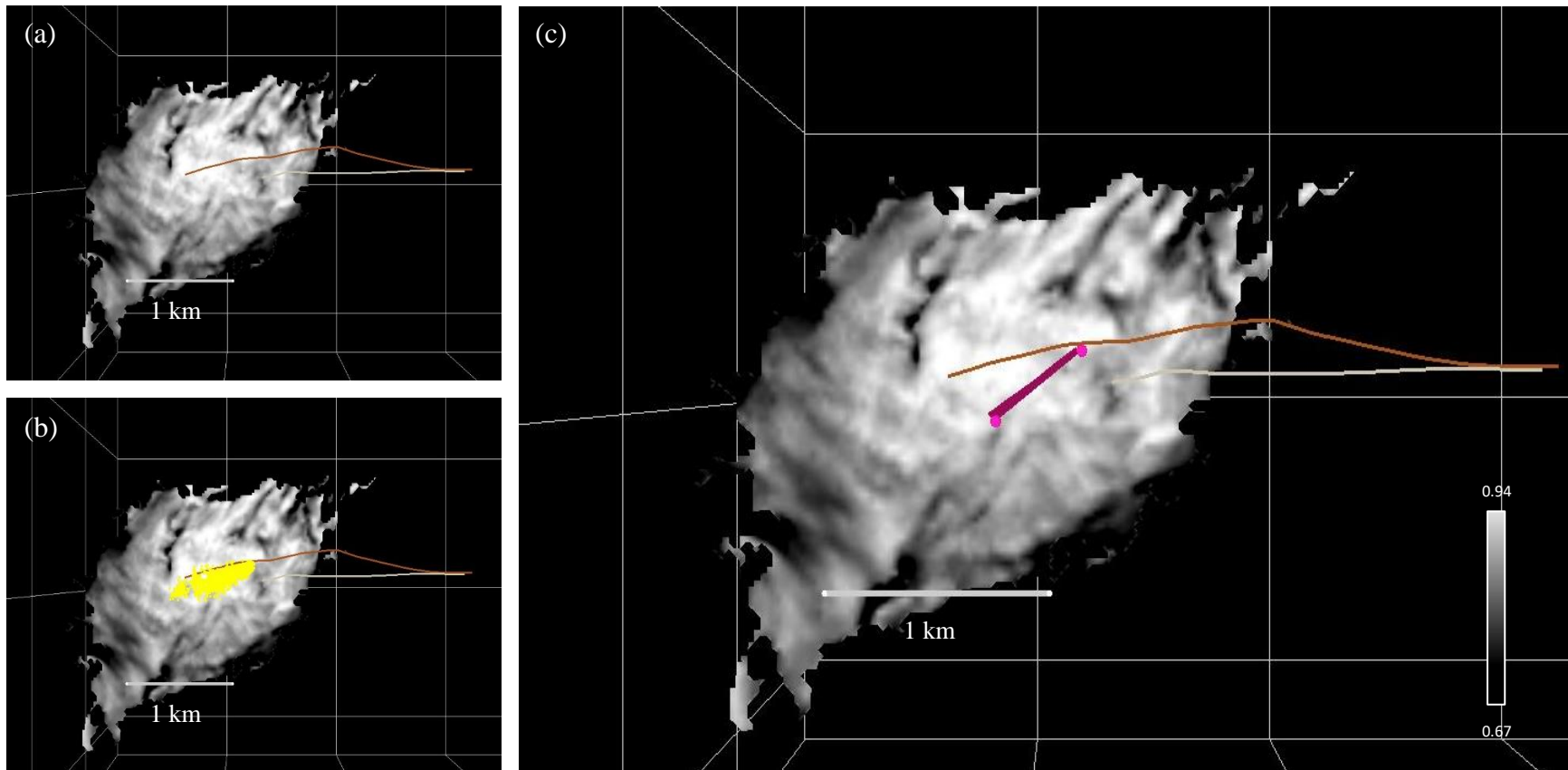


Figure 5-5: (a) Similarity attribute applied on the picked horizon near PNR-1z events. (b) Similarity attribute applied on the picked horizon near PNR-1z events with the actual event locations (yellow dots). (c) Similarity attribute applied on the picked horizon near PNR-1z events with the fault plane (pink plane) established by Clarke et al. (2019). The white line represents the PNR-1z well track, while the orange line represents the PNR-2 well track.

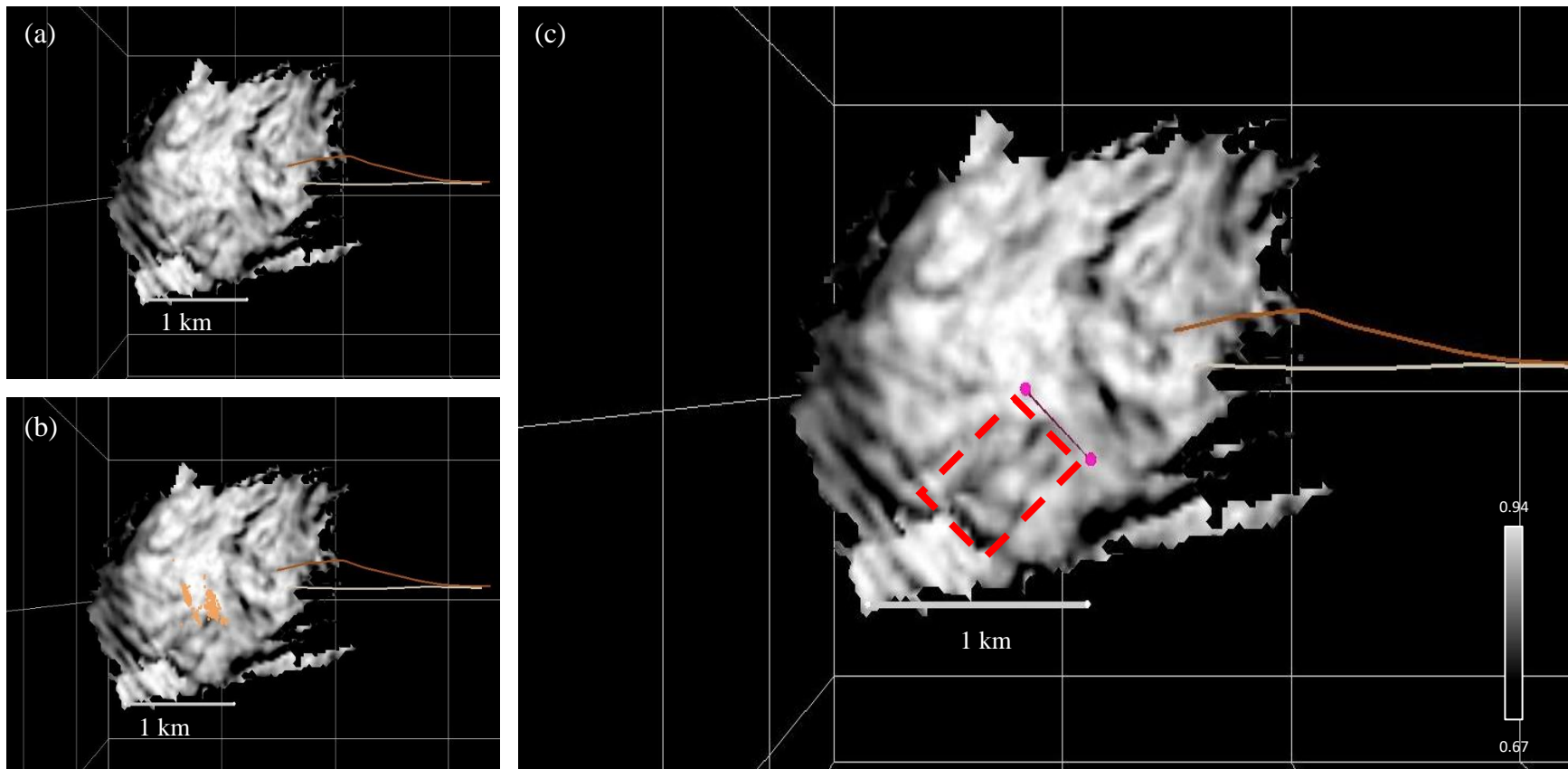


Figure 5-6: (a) Similarity attribute applied on the picked horizon near PNR-2 events. (b) Similarity attribute applied on the picked horizon near PNR-2 events with the actual event locations (orange dots). (c) Similarity attribute applied on the picked horizon near PNR-2 events with the fault plane (pink plane) established by Kettlety et al. (2020). The white line represents the PNR-1z well track, while the orange line represents the PNR-2 well track. The red, dashed box represents 2 geological features that might get cut by the causative fault and disappear.

5.1.2 Spectral Decomposition

I have also applied the spectral decomposition attribute to this portion of the data set. I generated an RGB colour-blended horizon using the spectral decomposition attribute with low (15 Hz), mid (30 Hz), and high (50 or 70 Hz) frequency values (Figure 5-7 and 5-8). This method seems to reveal additional faults represented by dark-coloured areas, which are not picked up by the similarity attribute. The reactivated fault at the PNR-1z is not obviously highlighted by this method, while the same phenomenon occurs again for the PNR-2 fault. The 2 dark lines identified in Figure 5-6 are also detected by the spectral decomposition attribute in Figure 5-8. Again, these dark lines get cut off and disappear at the fault plane identified by Kettelty et al. (2020). This might indicate the presence of the causative fault of the PNR-2 events.

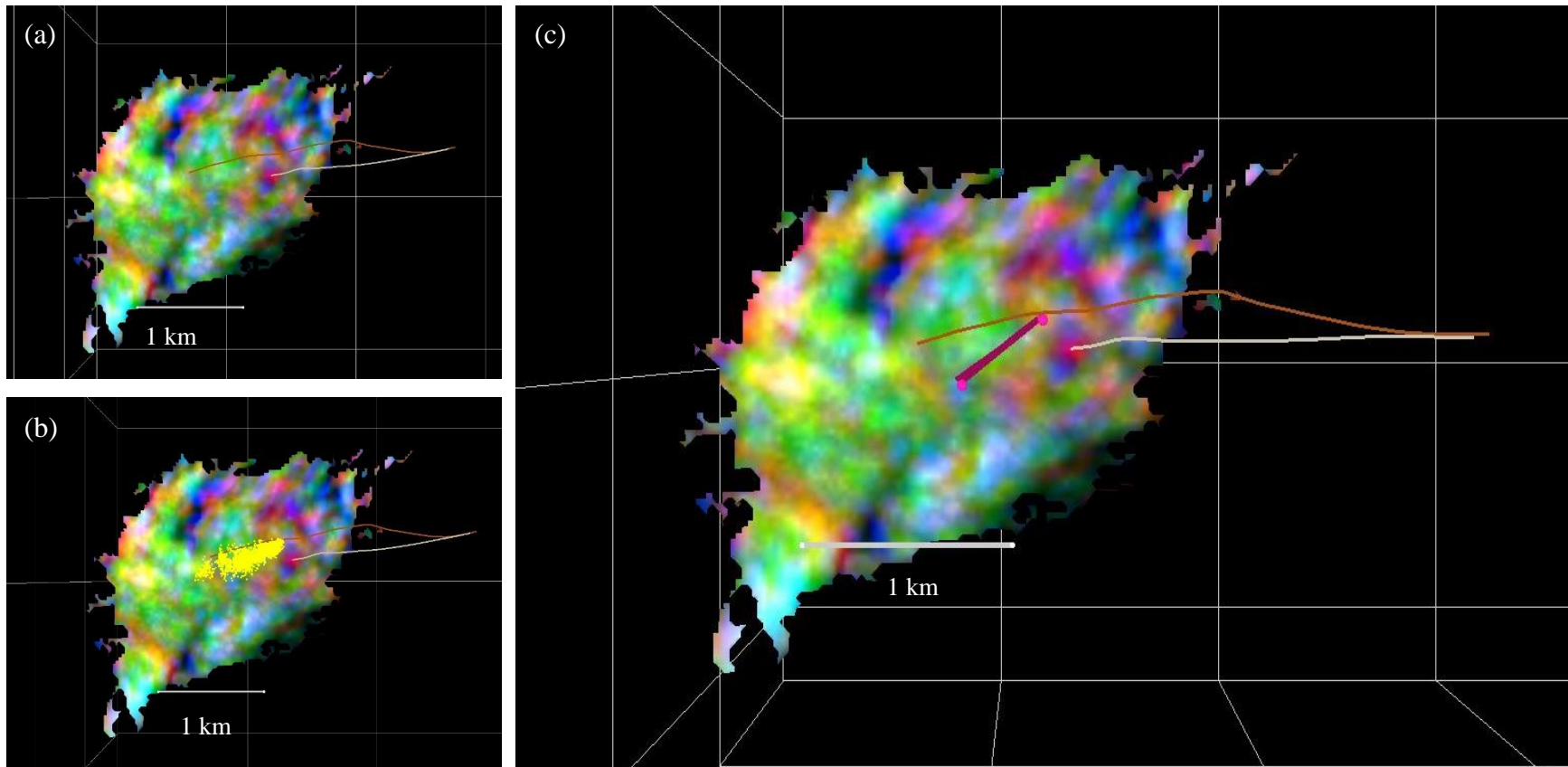


Figure 5-7: (a) RGB colour-blended spectral decomposition attributes on picked horizons near PNR-1z events. (b) RGB colour-blended spectral decomposition attributes on picked horizons near PNR-1z events with the actual event locations (yellow dots). (c) RGB colour-blended spectral decomposition attributes on picked horizons near PNR-1z events with the fault plane (pink plane) established by Clarke et al. (2019). R-component is 15 Hz, G-component is 30 Hz, and B-component is 70 Hz. The white line represents the PNR-1z well track, while the orange line represents the PNR-2 well track.

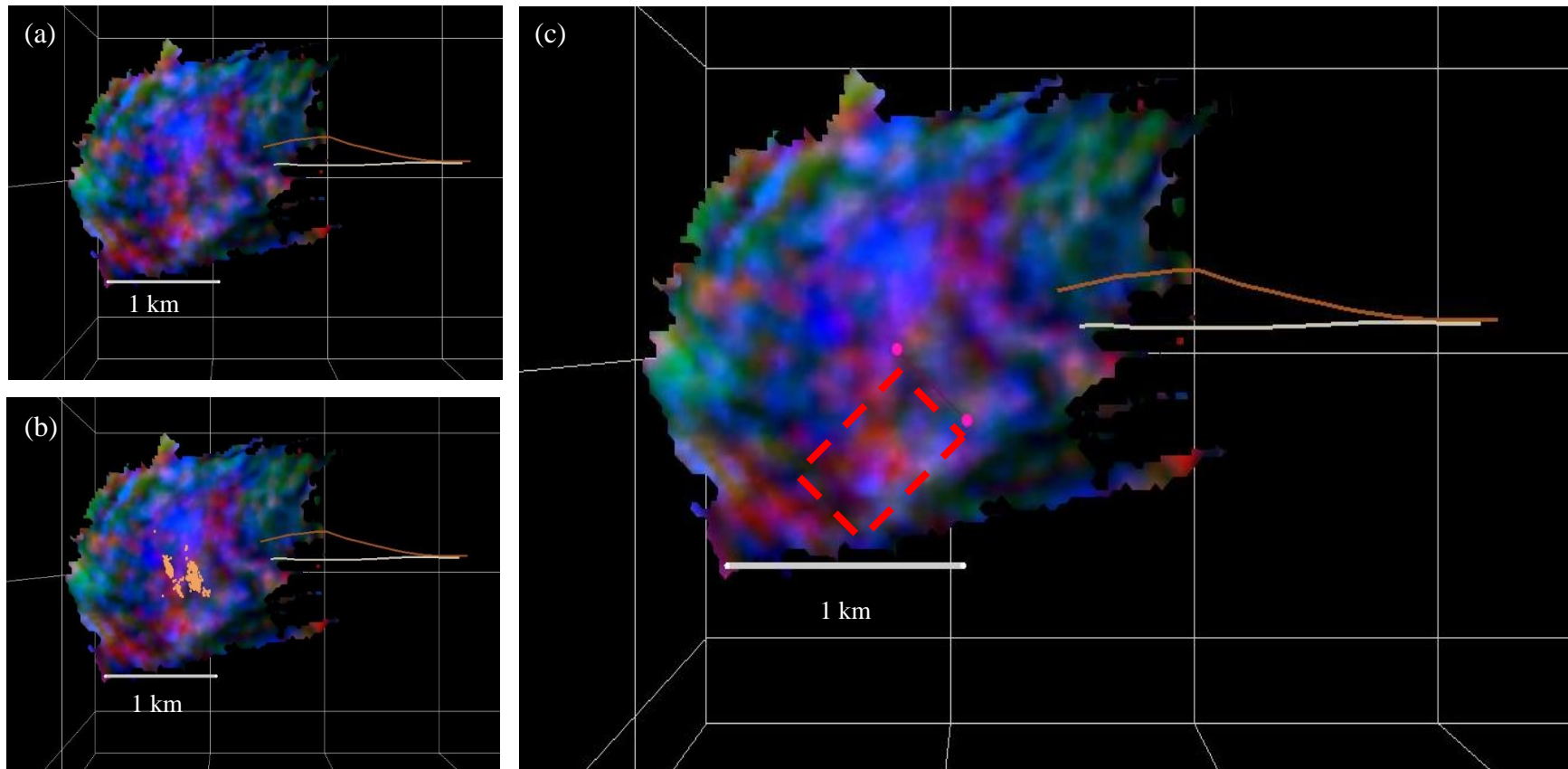


Figure 5-8: (a) RGB colour-blended spectral decomposition attributes on picked horizons near PNR-2 events. (b) RGB colour-blended spectral decomposition attributes on picked horizons near PNR-2 events with the actual event locations (orange dots). (c) RGB colour-blended spectral decomposition attributes on picked horizons near PNR-2 events with the fault plane (pink plane) established by Kettlety et al. (2020). R-component is 15 Hz, G-component is 30 Hz, and B-component is 50 Hz. The white line represents the PNR-1z well track, while the orange line represents the PNR-2 well track. The red, dashed box represents 2 geological features that potentially get cut off by the fault.

Analysing a single high-frequency spectral decomposition map (Figure 5-9 to 5-13) seems to be able to detect the causative faults at the PNR sites better as small features can be better highlighted with high-frequency tuning (Barbato, 2012; Jahan & Castagna, 2017). This is because a high-frequency wavelet has a smaller wavelength, so it is more sensitive to smaller features. Figure 5-10 reveals a weak dark line in roughly the same position as the fault identified with microseismic observations at PNR-1z well (white, dashed boxes in Figure 5-10). Therefore, there is a possibility that this small fault is the one that reactivated and caused the induced seismicity in 2018. The presence of the reactivated fault that causes the felt seismicity at PNR-2 well, however, is still ambiguous at best. This method is able to pick up the aforementioned geological features (red, dashed box in figure 5-13) that potentially get cut off by the fault, but it cannot reveal the fault itself. Even though the attribute highlights a faint dark line that has the similar orientation as the fault plane from Kettlety et al. (2020) (white, dashed boxes in Figure 5-13), it cannot be tracked further as the dark line disappears at proximal depths.

The newly found PNR-1z fault has been picked and mapped. The strike and dip of its fault plane are $\sim 216^\circ (\pm 19^\circ)$ and $\sim 55^\circ (\pm 7^\circ)$ respectively, which is slightly different from what Clarke et al. (2019) found (the strike of $\sim 237^\circ$ and dip of $\sim 70^\circ$). The depth extent and length of the fault plane in map-view are 130 m and 200 m. Nevertheless, the size of the fault plane identified by Clarke et al. (2019) is at least 520 m in map-view, which is much bigger than what I found. This might be because spectral decomposition at high tuning frequency tends to be attenuated easily (Othman et al., 2016), which means that it can be interfered by other sources such as small fractured horizons.

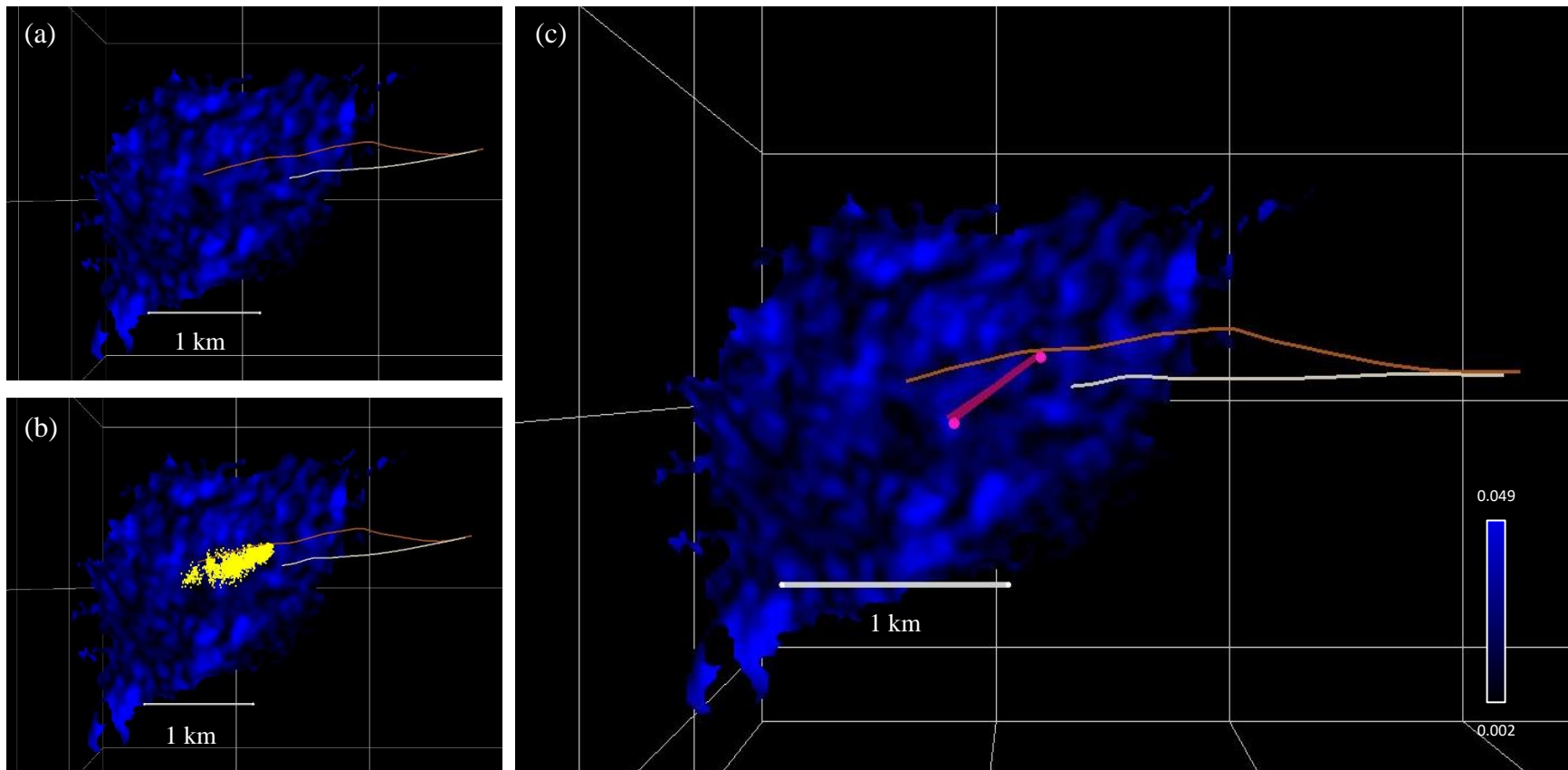


Figure 5-9: (a) High-frequency (70 Hz) spectral decomposition attributes on picked horizons near PNR-1z events. (b) High-frequency (70 Hz) spectral decomposition attributes on picked horizons near PNR-1z events with the actual event locations (yellow dots). (c) High-frequency (70 Hz) spectral decomposition attributes on picked horizons near PNR-1z events with the fault plane (pink plane) established by Clarke et al. (2019). The white line represents the PNR-1z well track, while the orange line represents the PNR-2 well track.

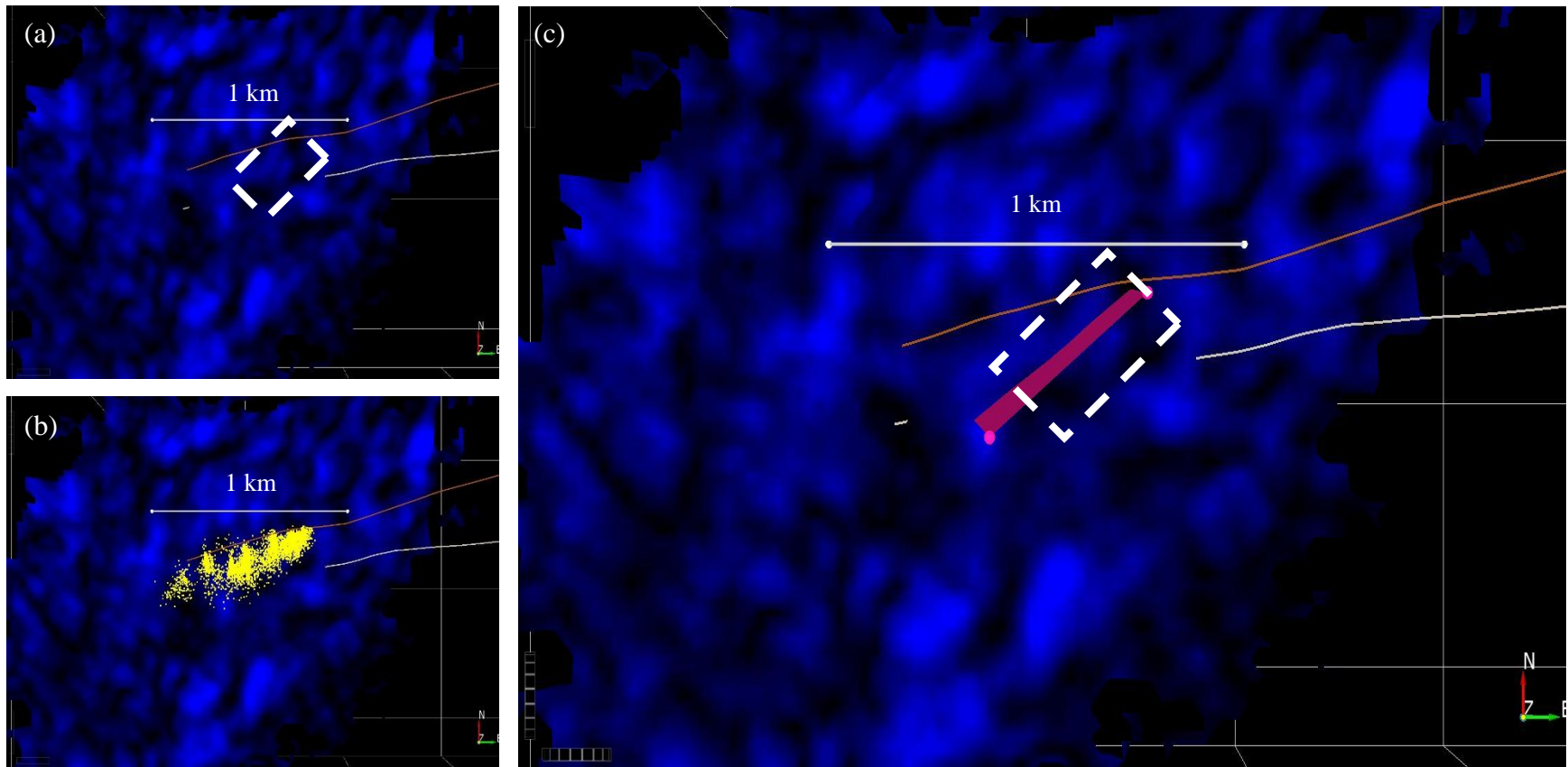


Figure 5-10: (a) Zoomed-in high-frequency (70 Hz) spectral decomposition attributes on picked horizons near PNR-1z events. (b) Zoomed-in high-frequency (70 Hz) spectral decomposition attributes on picked horizons near PNR-1z events with the actual event locations (yellow dots). (c) Zoomed-in high-frequency (70 Hz) spectral decomposition attributes on picked horizons near PNR-1z events with the fault plane (pink plane) established by Clarke et al. (2019). The white line represents the PNR-1z well track, while the orange line represents the PNR-2 well track. The white boxes indicate a dark line that is believed to be the causative fault of the PNR-1z felt seismicity.

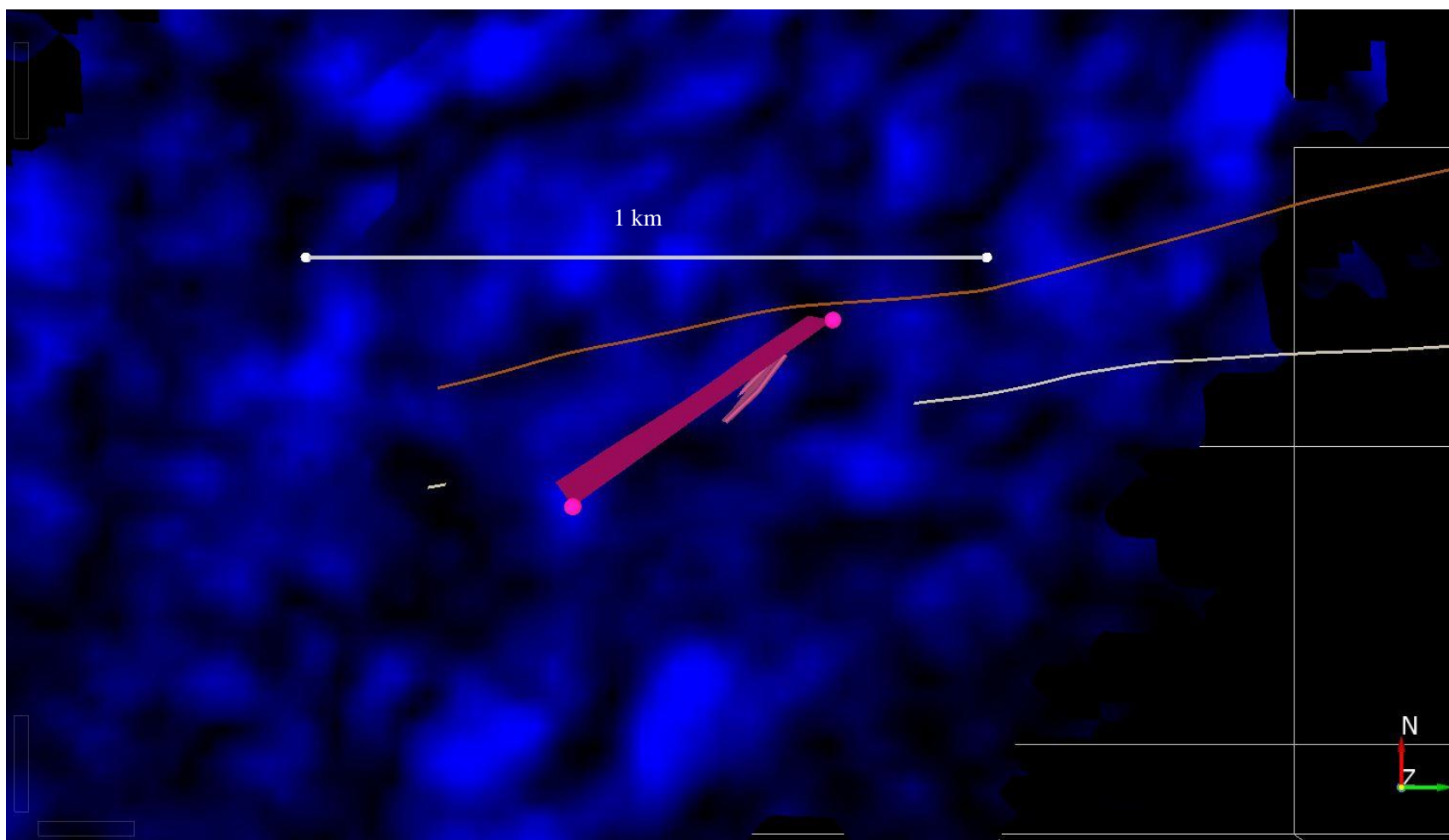


Figure 5-11: The identified fault is picked and tracked. The lighter pink plane represents the newly picked fault plane. The darker pink plane represents the fault plane established by Clarke et al. (2019). The white line represents the PNR-1z well track, while the orange line represents the PNR-2 well track.

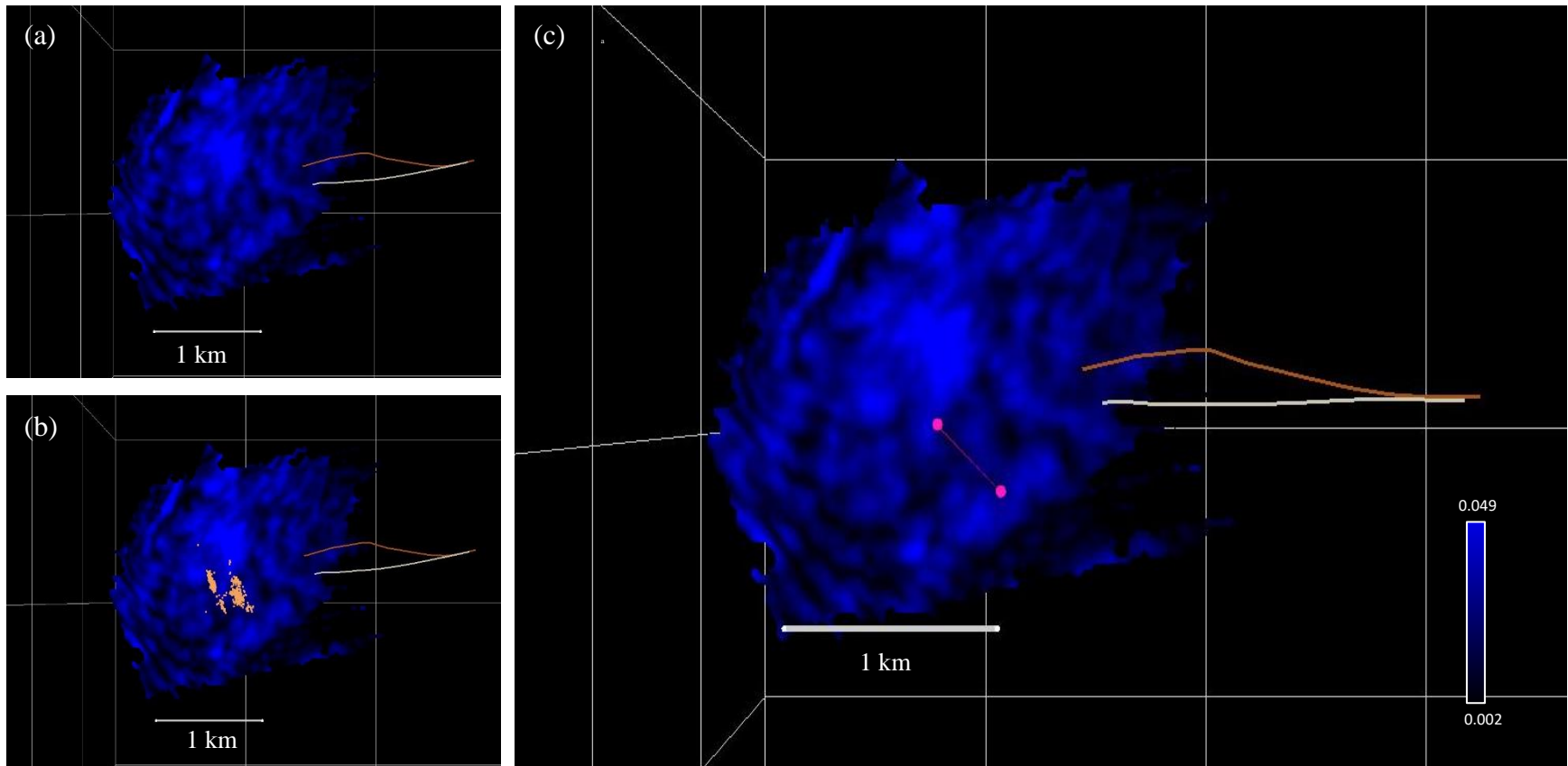


Figure 5-12: (a) High-frequency (50 Hz) spectral decomposition attributes on picked horizons near PNR-2 events. (b) High-frequency (50 Hz) spectral decomposition attributes on picked horizons near PNR-2 events with the actual event locations (orange dots). (c) High-frequency (50 Hz) spectral decomposition attributes on picked horizons near PNR-2 events with the fault plane (pink plane) established by Kettlety et al. (2020). The white line represents the PNR-1z well track, while the orange line represents the PNR-2 well track.

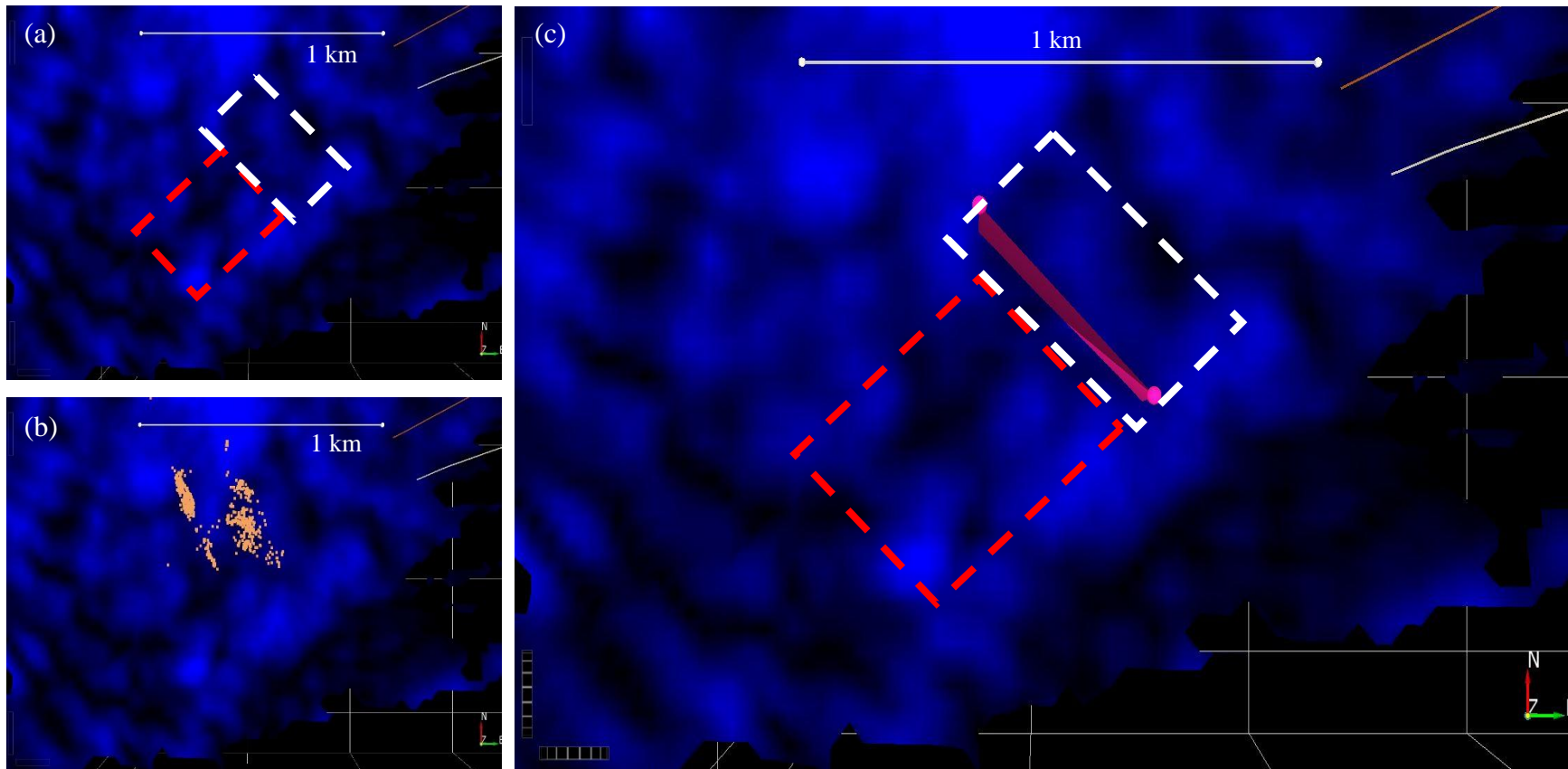


Figure 5-13: (a) Zoomed-in high-frequency (50 Hz) spectral decomposition attributes on picked horizons near PNR-2 events. (b) Zoomed-in high-frequency (50 Hz) spectral decomposition attributes on picked horizons near PNR-2 events with the actual event locations (orange dots). (c) Zoomed-in high-frequency (50 Hz) spectral decomposition attributes on picked horizons near PNR-2 events with the fault plane (pink plane) established by Kettlety et al. (2020). The white line represents the PNR-1z well track, while the orange line represents the PNR-2 well track. The white, dashed boxes indicate a faint dark line, which is suspected to be the causative fault, but it cannot be tracked further. The red, dashed boxes represent the geological features that potentially get cut off by the fault.

5.1.3 Curvature

The curvature attribute has been utilized to find potential vertical offsets caused by faults or other features on the picked surfaces. Similarly, this attribute has also been applied to the same horizons. Figure 5-14 to 5-17 show the most-positive and most-negative curvature attributes applied on the picked horizons for detecting the reactivated faults. Nevertheless, it is unable to pick up the offsets from the reactivated faults at both PNR-1z and PNR-2 wells as there are no obvious sign that indicates the presence of the faults near the fault planes derived from Clarke et al. (2019) and Kettlety et al. (2020).

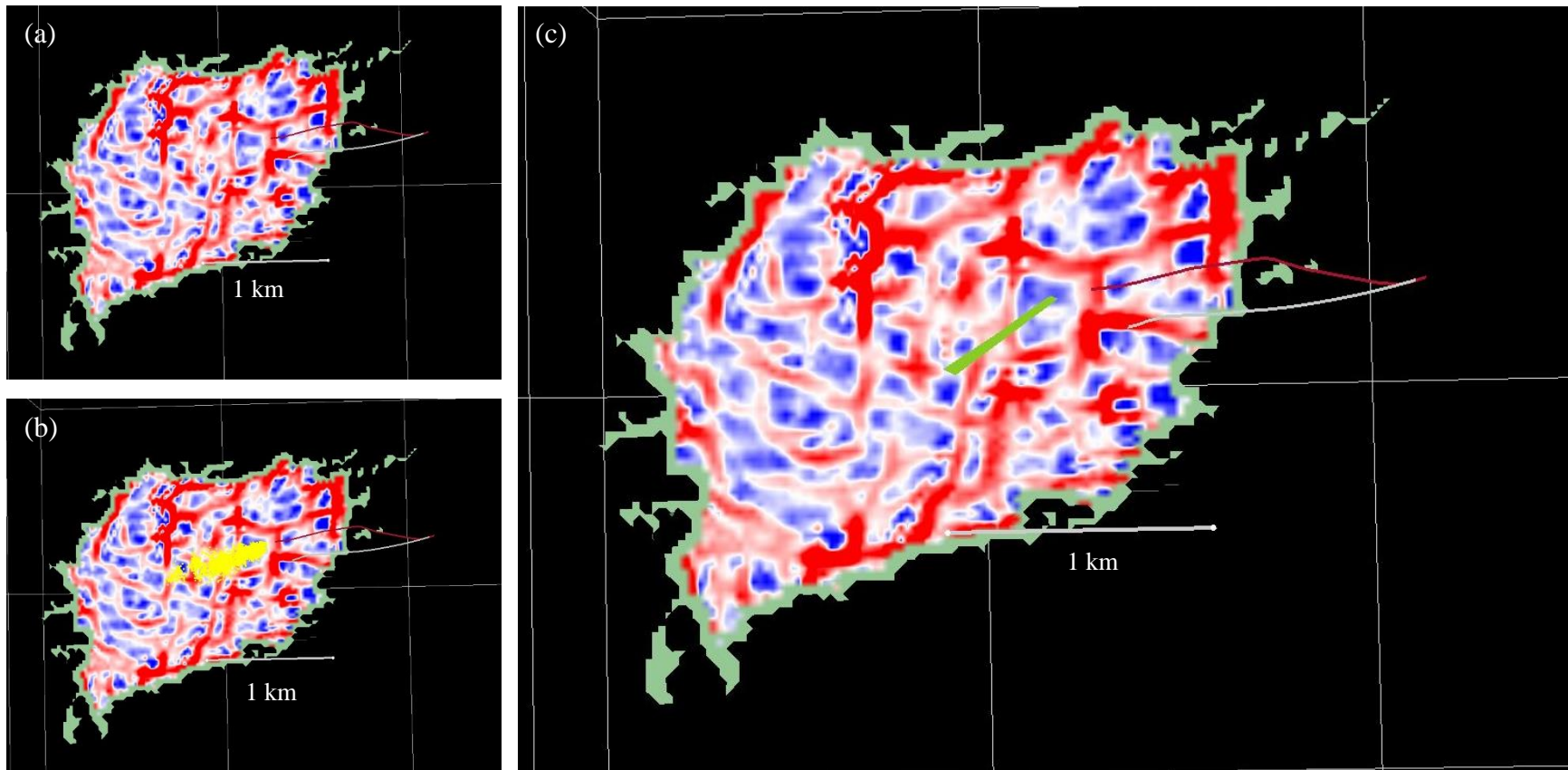


Figure 5-14: (a) Most-positive curvature attribute applied on the picked horizon near the PNR-1z events. (b) Most-positive curvature attribute applied on the picked horizon near the PNR-1z events with event clustered represented by yellow dots. (c) Most-positive curvature attribute applied on the picked horizon near the PNR-1z events with the fault plane (green plane) derived from Clarke et al. (2019). The white line represents the PNR-1z well track, while the red line represents the PNR-2 well track.

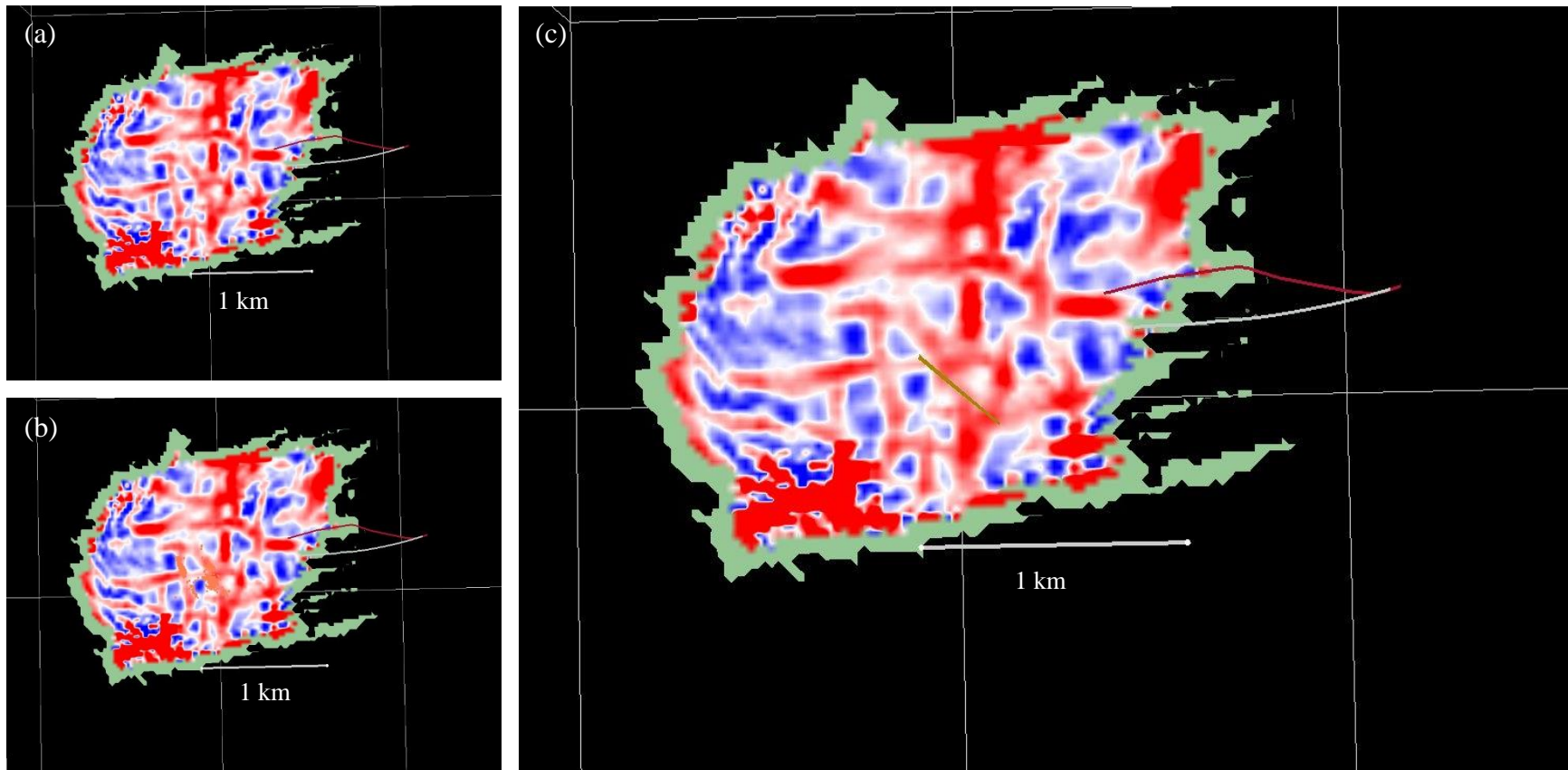


Figure 5-15: (a) Most-positive curvature attribute applied on the picked horizon near the PNR-1z events. (b) Most-positive curvature attribute applied on the picked horizon near the PNR-2 events with event clustered represented by orange dots. (c) Most-positive curvature attribute applied on the picked horizon near the PNR-2 events with the fault plane (brown plane) derived from Kettley et al. (2020). The white line represents the PNR-1z well track, while the red line represents the PNR-2 well track.

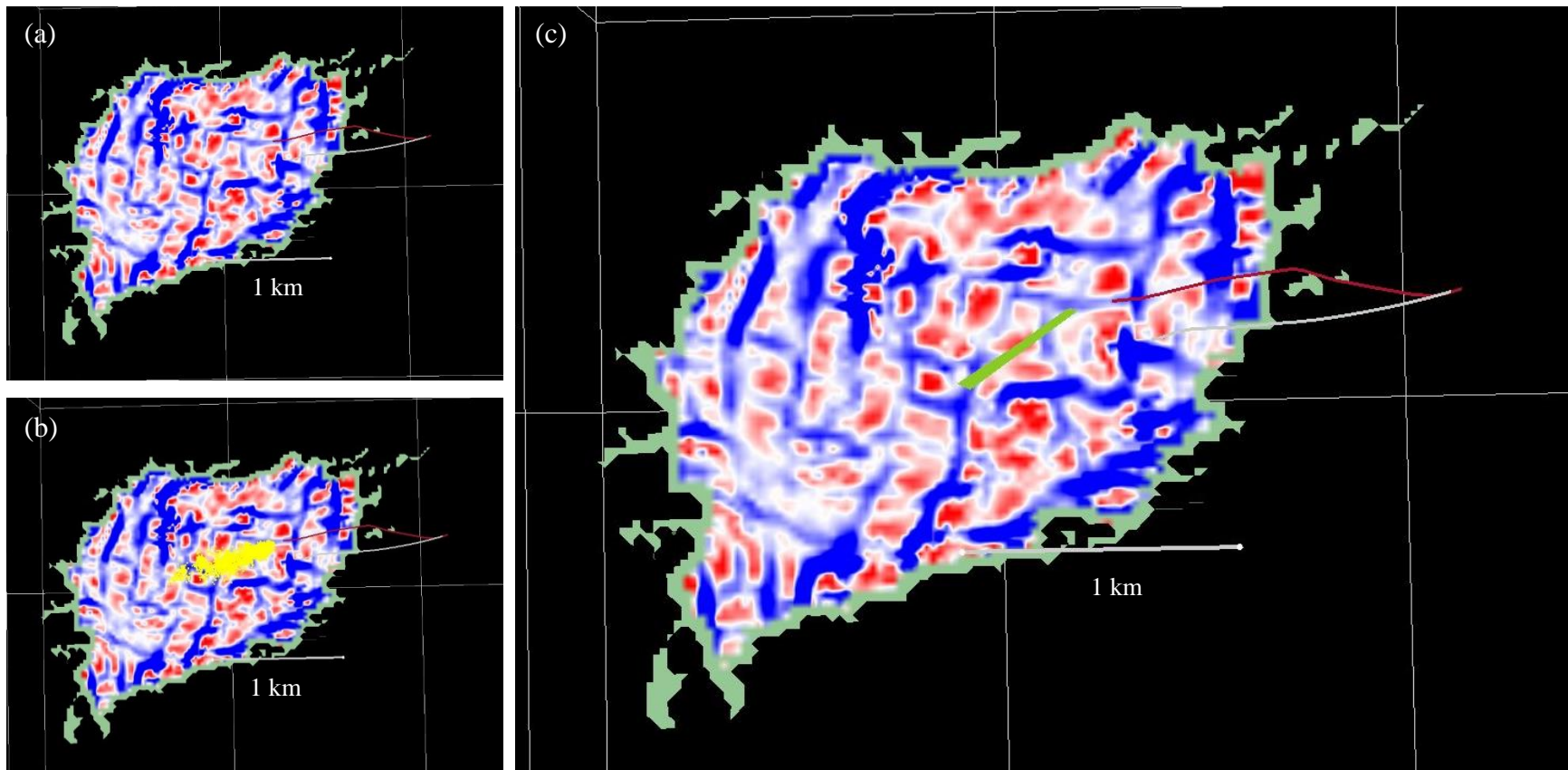


Figure 5-16: (a) Most-negative curvature attribute applied on the picked horizon near the PNR-1z events. (b) Most-negative curvature attribute applied on the picked horizon near the PNR-1z events with event clustered represented by yellow dots. (c) Most-negative curvature attribute applied on the picked horizon near the PNR-1z events with the fault plane (green plane) derived from Clarke et al. (2019). The white line represents the PNR-1z well track, while the red line represents the PNR-2 well track.

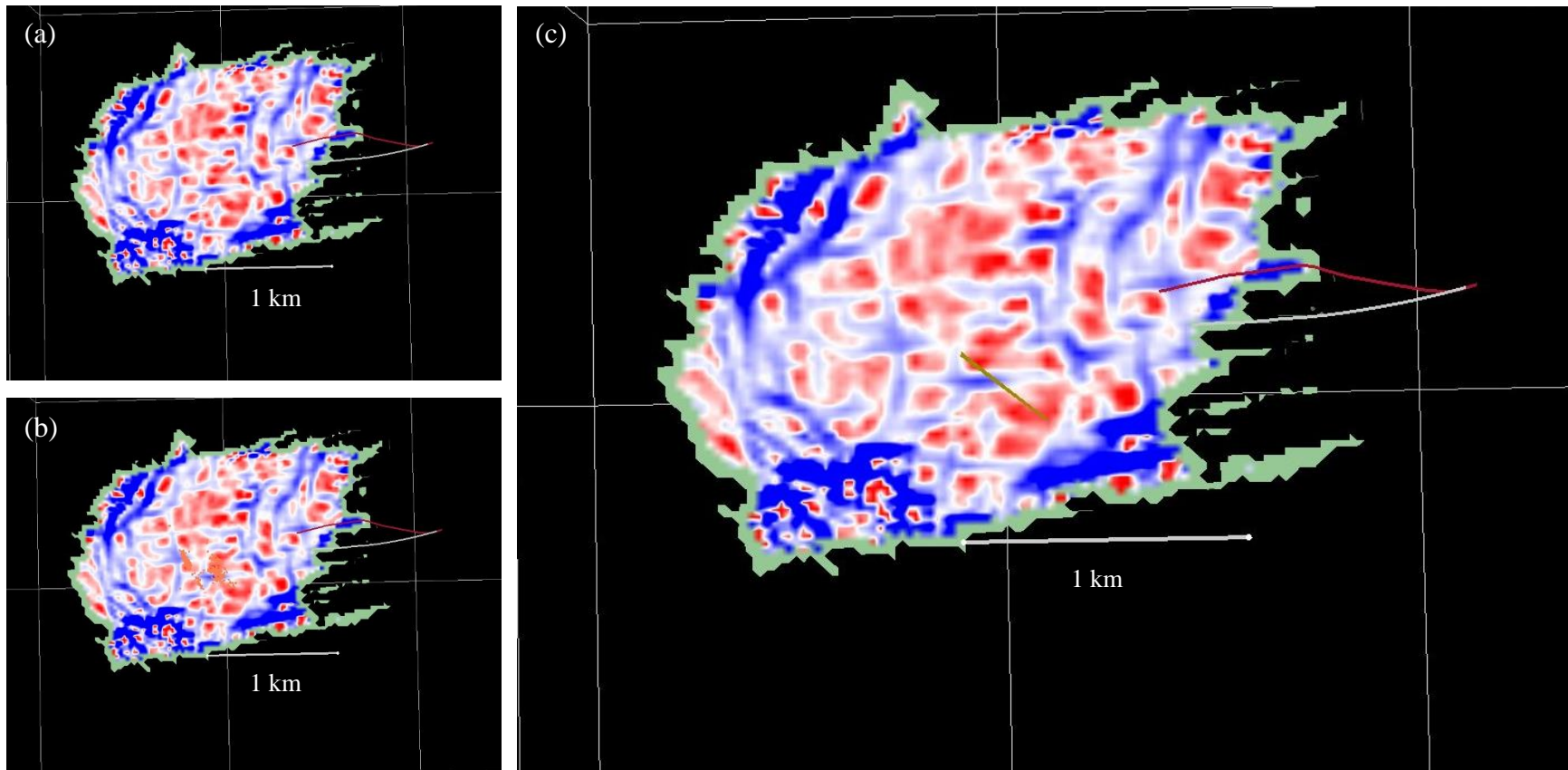


Figure 5-17: (a) Most-negative curvature attribute applied on the picked horizon near the PNR-1z events. (b) Most-negative curvature attribute applied on the picked horizon near the PNR-2 events with event clustered represented by orange dots. (c) Most-negative curvature attribute applied on the picked horizon near the PNR-2 events with the fault plane (brown plane) derived from Kettley et al. (2020). The white line represents the PNR-1z well track, while the red line represents the PNR-2 well track.

5.2 The Comparison between the Fault Investigation Using the Seismic Attributes and the Investigation Using Only the 3D Seismic Data

Figure 5-18 shows the comparison between the 2 methods of the fault investigation: using the seismic attributes and using the 3D seismic data. The results show that the seismic attributes are able to pick up most of the faults picked by using only the 3D seismic data. The seismic attributes are also able to detect more faults that were not previously seen on the 3D seismic data. The similarity and spectral decomposition attributes detect the changes in the seismic signals, showing faults in darker lines in Figure 5-18 (a) and (c). The curvature attribute (Figure 5-18 (e) and (f)) detects the changes in the shape of the surface, so it can detect offsets of faults. Thus, most of the faults are aligned between the zones with high and low curvature values since they represent the abrupt changes in the surface shape, or the offsets of the faults. This figure verifies that the applications of the seismic attributes can improve the fault investigation of the Bowland Shale. This motivates the reactivated faults investigation by using the seismic attributes in this study.

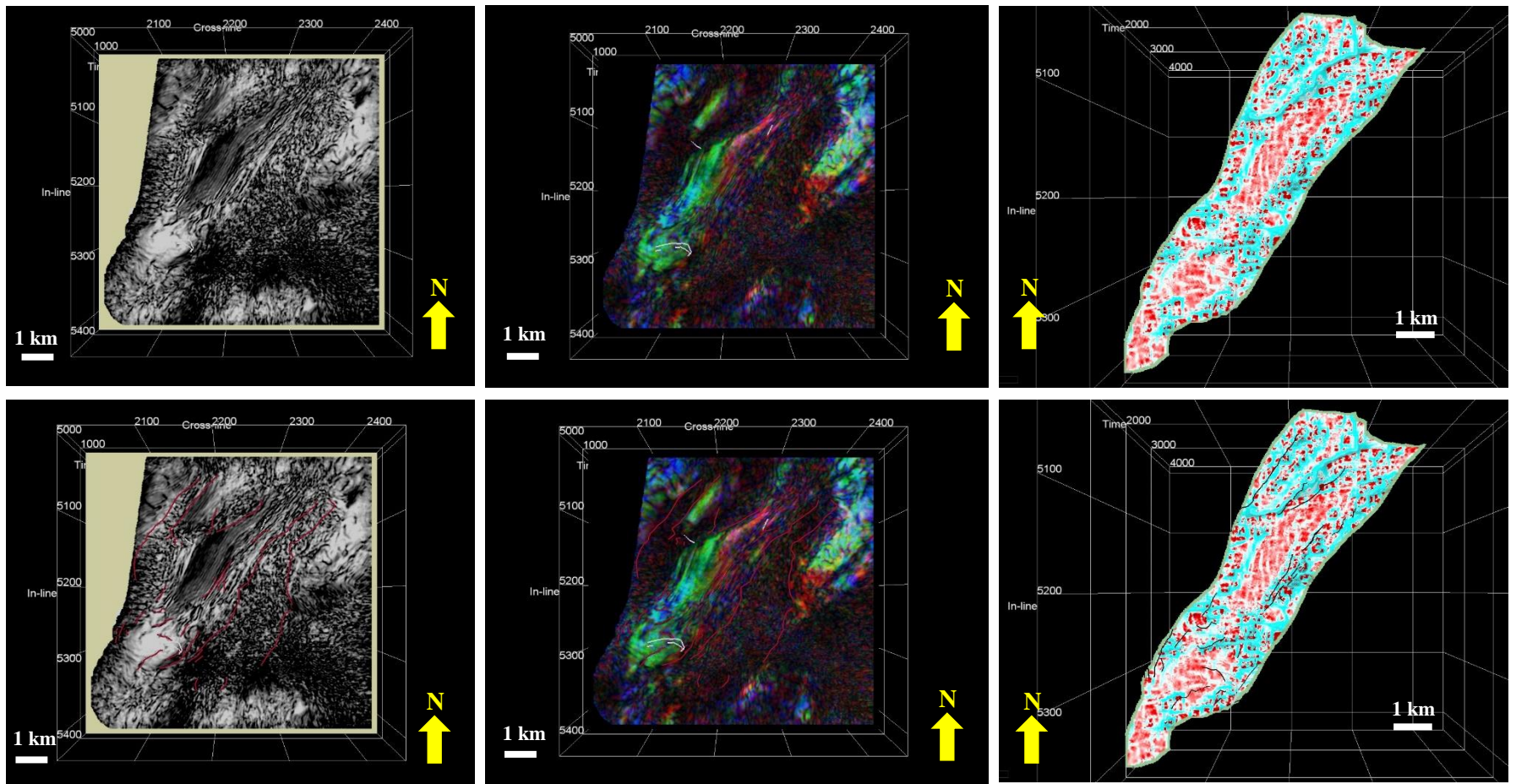


Figure 5-18: The efficiency of the fault investigation using the seismic attributes, compared to the investigation using only the 3D seismic data. (a) and (b) represent the similarity attribute applied on a time slice at 1,270 ms (2,366 m) with the locations of the faults picked in Chapter 4 (red lines in (b)). (c) and (d) represent the colour-blended spectral decomposition applied on a time slice at 1,270 ms (2,366 m) with the locations of the faults picked in Chapter 4 (red lines in (d)). (e) and (f) show the most negative curvature applied on the Lower Bowland Shale horizon with the locations of the faults picked in Chapter 4 (black lines in (f)). The well tracks are represented by the white lines.

5.3 Discussion

The results suggest that these causative faults at the PNR sites are either too small to be picked up by the conventional seismic attributes, or they are hidden by the interference of noise. These faults must be present since they cannot be new faults generated during the hydraulic fracturing because their orientations are different from the maximum horizontal stress direction (azimuth of $\sim 170^\circ$) at which fractures from hydraulic stimulation will propagate. The fault identified in the microseismic data at PNR-1z well does not show up in the similarity, curvature, or in the spectral decomposition at low or mid frequency. Only the high frequency spectral decomposition attribute reveals possible faulting features, and even these are not wholly compelling. On the other hand, the presence of the PNR-2 fault is still ambiguous with the application of these seismic attributes. The fault itself does not show up in any of the seismic attributes applied on the horizons, but there are vague signs of the fault found on the horizons with the similarity and the spectral decomposition attributes as mention above. This suggests that these faults might be too small and subtle to cause offsets or dissimilarity on the seismic horizons, or that they are strike-slip faults, which typically do not generate vertical offsets on a surface. The focal mechanism data from Clarke et al. (2019) and Kettlety et al. (2020) support this interpretation that both of them are likely strike-slip faults. The similarity, spectral decomposition and curvatures attributes all rely on vertical offsets or changes in the surface's shape; thus, it is hard to see strike-slip faults in these attributes.

In general, it is possible to detect strike-slip faults on a vertical cross-section of a seismic data (Pedro, 1987). Pedro (1987) proposes the criteria for identifying strike-slip faults on a cross-section. These include the presence of flower structures, offsets, abrupt changes in seismic facies along the fault, and changes in the amount or dipping direction of the fault plane along the strike

(Pedro, 1987). However, these features are not present in this work as the reactivated faults are subtle and not visible on the 3D seismic data. In addition, there were several successful practical attempts to detect strike-slip faults using the conventional seismic attributes. For example, the study of Tarim Basin, China by Ma et al. (2019) shows that strike-slip faults show up on similarity and amplitude attributes. Another example is the case study in Eastern Colombia by Pico et al. (2014), where they were able to detect strike-slip faults using the coherence and volume curvature attributes. However, it is not the case in this study, where the faults do not obviously show up on these attributes, potentially because of how subtle they are.

Furthermore, there is a possibility that the interference from noise can cause false positives and errors. The signal interference of small, fractured layers can distort the signals of the causative faults or generate false positives by the constructive interference of small lobes of signals. Since this spectral decomposition technique is performed at a high frequency, even a small interference from other layers or structures can easily change the outcomes (Othman et al., 2016). Thus, there is a chance that the signals from these faults are interfered, resulting in misinterpretations.

Under the current technology, faults with the magnitude of M_L 2.9 or smaller events are still hard to be seen on 3D reflection seismic data and seismic attributes, according to the results of this study. Without the data from Clarke et al. (2019) and Kettlety et al. (2020), it is very difficult to locate the causative faults even with the seismic attributes applied since they have similar appearance to false positives and other geological features. Therefore, seismic monitoring as well as the Traffic Light Scheme are important for mitigating felt seismicity from hydraulic stimulation. These data, combined with the data from the WCSB, indicate that there are a lot of uncertainties in investigating hidden reactivated faults from hydraulic fracturing, which also

means there are still rooms for improvements for geological technology and knowledge in the future.

Chapter 6: Well Log Analysis

The second goal of this study is to identify sweet spots within the Bowland Shale. To achieve this, the well log analysis, seismic inversion, and $\lambda\rho$ - $\mu\rho$ calculation are performed. In this chapter, I analyse the well logs from Preese Hall-1 (PH-1) and Preston New Road-1 (PNR-1) wells to establish the relationship between geophysical variables and rock properties. Well logs provide essential information about rock formations under the surface, allowing the calibration of seismic observations and lithological properties.

6.1 PCC and PCA of PH-1 and PNR-1 wells

Pearson's Correlation Coefficient analysis (PCC) and Principal Component Analysis (PCA) are statistical techniques for finding meaningful relationships between two or more sets of data. PCC analysis is based on the coefficient r , which measures the linear relationship between two variables. For PCA, the sets of data are plotted against each other in multidimensional space to find the eigenvectors, which can identify overall trends within the data. These statistical techniques can be applied to well logs to determine the relationship and interdependency between different geophysical variables.

Tables 6-1 to 6-4 and Figures 6-1 and 6-2 show the PCC and the PCA results for the PH-1 well, for both the whole well log and for only the Bowland Shale. Tables 6-5 and 6-6 and Figure 6-3 show the same for the PNR-1 well. Table 6-1 shows that, for the entire PH-1 well logs, every parameter shows a good correlation to each other, except for GR, which shows a weak relationship with DT and DTS, and a very weak relation to RHOB. This might be because GR only relates to lithology and does not depend on depth and pressure like other variables. According to Table 6-2, the parameter variability across the whole PH-1 well log can be

explained by the primary principal component (PC1) and the secondary principal component (PC2) as they account for more than 98% of the total variation of the logs. The eigenvector of PC1 is dominated by the GR component, meaning that the deviation in this log can be explained mostly by the GR component. Thus, most of the changes in every parameter respond to the changes in the GR log, and therefore reflect changes in the clay content of the rock. The PC1 score log in Figure 6-1 also shows the similarity to the GR log. PC2 is mostly dominated by DTS and DT, which are usually correlated well with each other in the area with no hydrocarbons or fluids. Therefore, PC2 score log may highlight the fluid or hydrocarbon presences in the well. Figure 6-1 shows that the PC2 score values become more negative in the Bowland Shale Formation (~2,000 m – 2,700 m). This may reveal the presence of hydrocarbon in the Bowland Shale Formation since P/S wavespeed ratio may behave differently in gas-bearing rock formations, as described above.

	DT	DTS	GR	NPHI	RHOB
DT	1	0.7742	0.3690	0.8238	-0.6978
DTS		1	0.2072	0.6126	-0.4742
GR			1	0.3699	-0.0376
NPHI				1	-0.7684
RHOB					1

Table 6-1: The r-coefficient values for the variables DT, DTS, GR, NPHI, and RHOB of the overall PH-1 well.

	PC1	PC2	PC3	PC4	PC5
DT	0.1150	0.4335	0.8931	0.0362	-0.0055
DTS	0.1223	0.8867	-0.4459	-0.0045	-0.0008
GR	0.9858	-0.1606	-0.0489	-0.0023	-0.0011
NP	0.0022	0.0065	0.0149	-0.3082	0.9512
RHOB	-0.0007	-0.0106	-0.0314	0.9506	0.3086
% Variance	80.62511	17.71093	1.660398	0.003108	0.000449

Table 6-2: The eigenvectors and %variance from the PCA of the variables DT, DTS, GR, NP, and RHOB from the overall PH-1 well.

	DT	DTS	GR	NPHI	RHOB
DT	1	0.8623	0.7532	0.8772	-0.6398
DTS		1	0.7436	0.8580	-0.6168
GR			1	0.7159	-0.4432
NPHI				1	-0.7365
RHOB					1

Table 6-3: The r-coefficient values for the variables DT, DTS, GR, NPHI, and RHOB of the PH-1 well (only Bowland Shale Formation).

	PC1	PC2	PC3	PC4	PC5
DT	0.1521	0.4188	0.8952	0.009	-0.0045
DTS	0.2454	0.8614	-0.4447	0.0037	-0.0022
GR	0.9574	-0.2873	-0.0283	-0.0003	-0.0003
NPHI	0.0021	0.0061	0.0053	-0.3797	0.9251
RHOB	-0.0012	-0.0051	-0.0048	0.9251	0.3797
% Variance	94.72641	4.605671	0.667414	0.000406	0.000101

Table 6-4: The eigenvectors and %variance from the PCA of the variables DT, DTS, GR, NPHI, and RHOB from the PH-1 well (only Bowland Shale Formation).

	DT	DTS	GR
DT	1	0.7366	0.6044
DTS		1	0.6376
GR			1

Table 6-5: The r-coefficient values for the variables DT, DTS, and GR of the PNR-1 well.

	PC1	PC2	PC3
DT	0.1381	0.3815	0.914
DTS	0.2511	0.8792	-0.4049
GR	0.9581	-0.2854	-0.0256
% Variance	91.04485	7.449422	1.505732

Table 6-6: The eigenvectors and %variance from the PCA of the variables DT, DTS, and GR from the PNR-1 well.

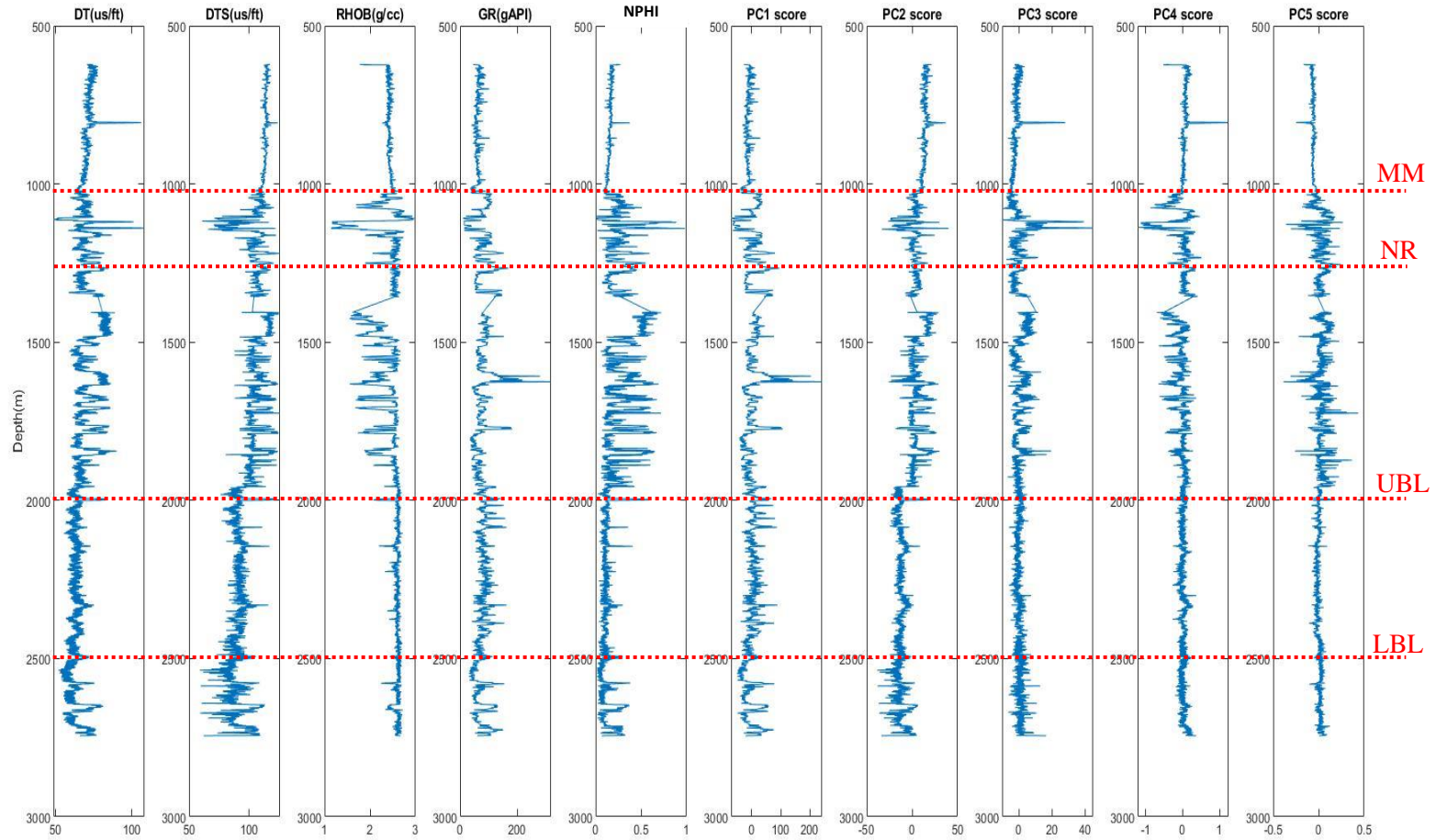


Figure 6-1: PH-1 well logs and PCA score logs. The formation tops' markers are represented by the red, dashed lines labeled with the abbreviated formation names. MM stands for the Manchester Marl Formation, NR is the Namurian Rough Rock, UBL is the Upper Bowland Shale Formation, and LBL represents the Lower Bowland Formation.

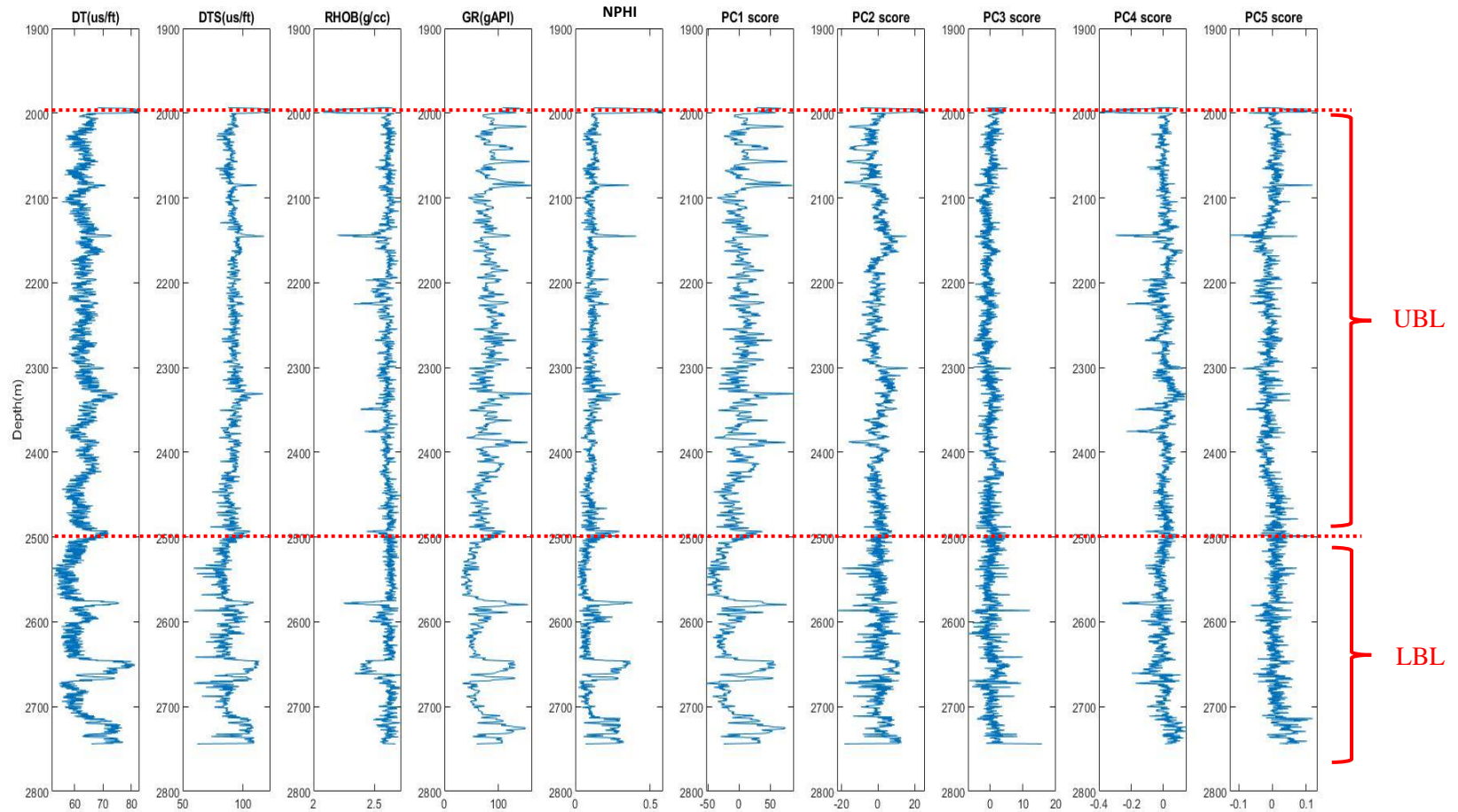


Figure 6-2: PH-1 well logs and PCA score logs (only for the Bowland Shale Formation). The formation tops' markers are represented by the red, dashed lines labeled with the abbreviated formation names. UBL is the Upper Bowland Shale Formation, and LBL represents the Lower Bowland Formation.

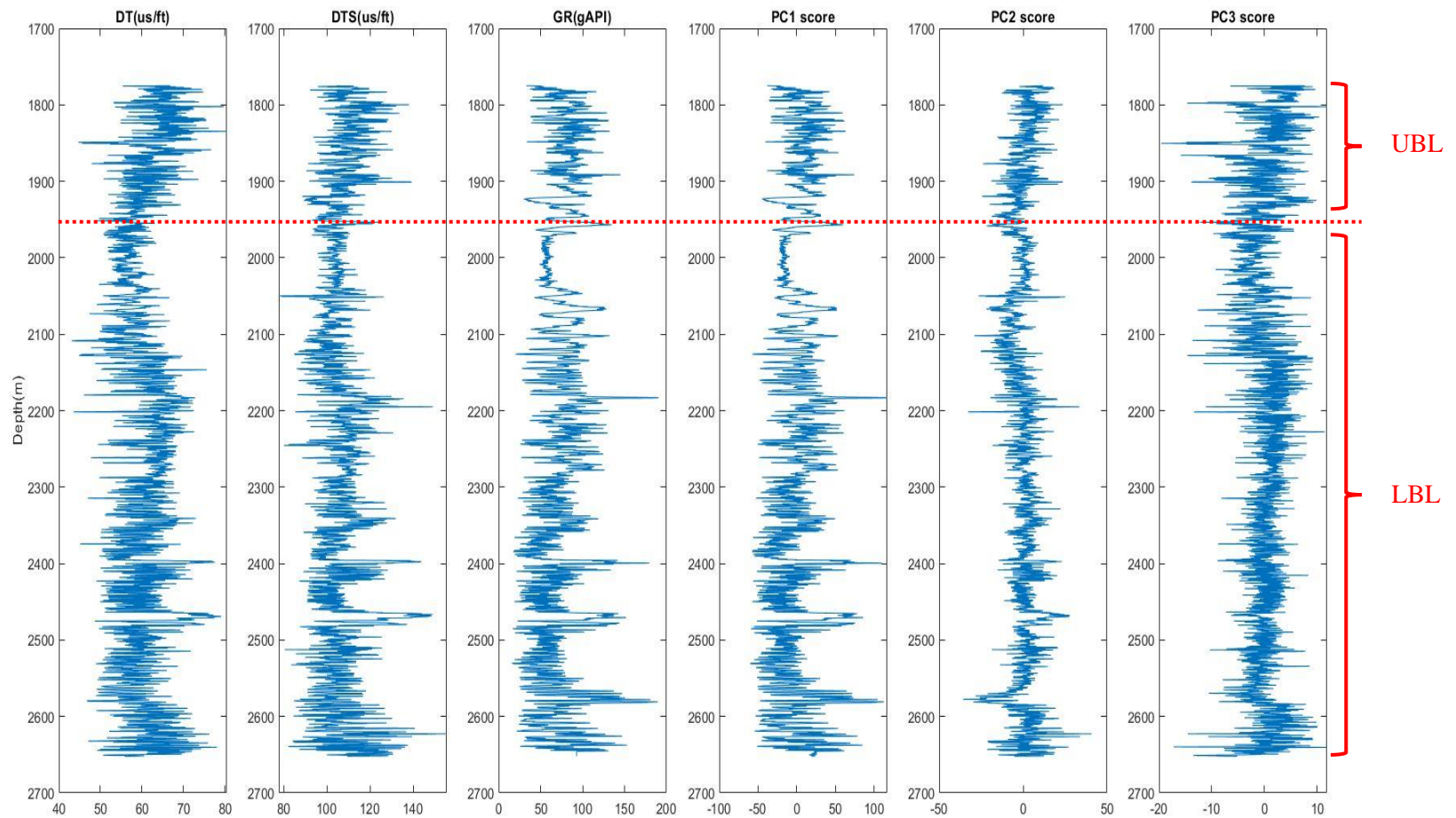


Figure 6-3: PNR-1 well logs and PCA score logs. The formation tops' markers are represented by the red, dashed lines labeled with the abbreviated formation names. UBL is the Upper Bowland Shale Formation, and LBL represents the Lower Bowland Formation.

The PCC and PCA for the Bowland Shale Formation from PH-1 logs show slightly different results. Table 6-3 shows that most of the variables have a strong correlation to each other, and only the RHOB variable has a negative relationship with the others. However, GR does not correlate well with RHOB. This might be because the presences of organic content and gas, which is hard to detect from the GR log, lower the bulk density of the shale formation. The PCA result from Table 6-4 indicates that geophysical parameter variation within the Bowland Shale Formation can also be explained by PC1 and PC2 with more than 99% of the total variation. The eigenvector of PC1 in the Bowland Shale Formation is, again, heavily dominated by GR log, making the PC1 score log very similar to the GR log in Figure 6-2. The PC2 is dominated by the combination of DT and DTS. The negative peaks in PC2 score log may be interpreted as hydrocarbon-rich zones.

Table 6-5 and 6-6 and Figure 6-3 contain the PCC and PCA data from the PNR-1 well. Since the PNR-1 well logs only have the data from the Bowland Shale Formation (mostly Lower Bowland Shale Formation), similar results as Table 6-3 and 6-4 were expected. However, the PCC results are slightly different from the PH-1 well. The PNR-1 well shows a much better correlation of GR to DT and DTS, compared to the data from the entire PH-1 well. The dissimilarity of the data from the PH-1 and PNR-1 wells might be because of the depth ranges of these data. The data from the PNR-1 well are limited to a much smaller depth range, so the GR log from the PNR-1 well linearly correlate more to other variables that change with depth like DT and DTS. The PCA results from both wells are similar. PC1 and PC2 account for more than 98% of variation in the data. The GR component dominates the variation of the PC1, while the PC2 is dominated by DT and DTS, similar to the previous well logs.

6.2 Cross-plot Analysis of PH-1 and PNR-1 Well Logs

Cross-plot analysis provides further insight into the relationship between geophysical properties of rocks as well as characterizing rock formations. Figure 6-4 shows a cross-plot between DT and DTS with the measured depth (MD), or the depth measured along the well path, as the colour-coding from the PH-1 well logs. This cross-plot clearly distinguishes the formations into 4 groups based on their lithologies. It shows a distinct trend as higher DT and DTS values (i.e., lower velocities) correspond to formations in the shallower depths, and vice versa. This is mostly because of the higher porosities and lower amounts of diagenesis at shallower depths, which results in lower V_p and V_s values. However, there is a cluster of data from the depth range of ~1,600 – 1,770 m that has very high DT and DTS (yellow polygon), which does not follow the general trend with depth. This group mostly belongs to the shales and siltstones in the Sabden Shale Group and Roeburndale Formation. The blue polygon delineates the data from the formations above the Variscan unconformity, which have high DT and DTS. The green polygon represents the data between the Variscan unconformity and the Bowland Shale Formation. They seem to follow the general trend with depth as they fall between the blue and red polygons. The Upper and Lower Bowland Shale Formations are marked by the red polygon on the lower side of the cross-plot, corresponding to higher V_s values. They are well separated from the rest of the formations, indicating that the Bowland Shale Formation has distinct physical properties.

Figure 6-5(a) shows the cross-plot analysis between V_p and GR with MD as the colour-coding within the Bowland Shale. It exhibits a negative linear relationship between GR and V_p , meaning that P-wave is slower in the regions with high shale content. Figure 6-5(b) shows the cross-plot analysis between V_p and RHOB with MD as the colour-coding within the Bowland

Shale. V_p and RHOB have a positive linear relationship to each other. Since V_p and GR are inversely correlated, this implies that rocks with low shale content have higher densities.

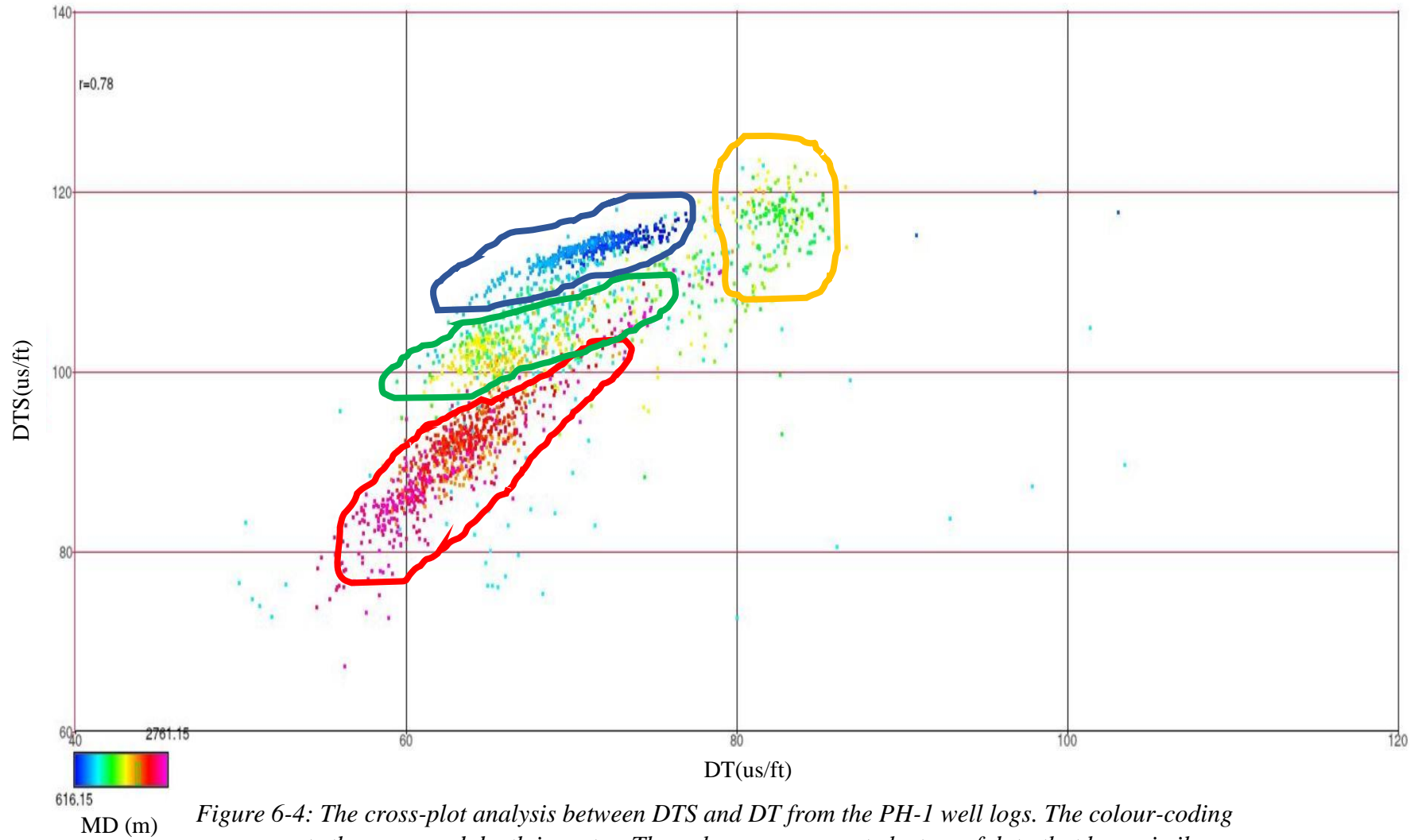


Figure 6-4: The cross-plot analysis between DTS and DT from the PH-1 well logs. The colour-coding represents the measured depth in meter. The polygons represent clusters of data that have similar geophysical properties.

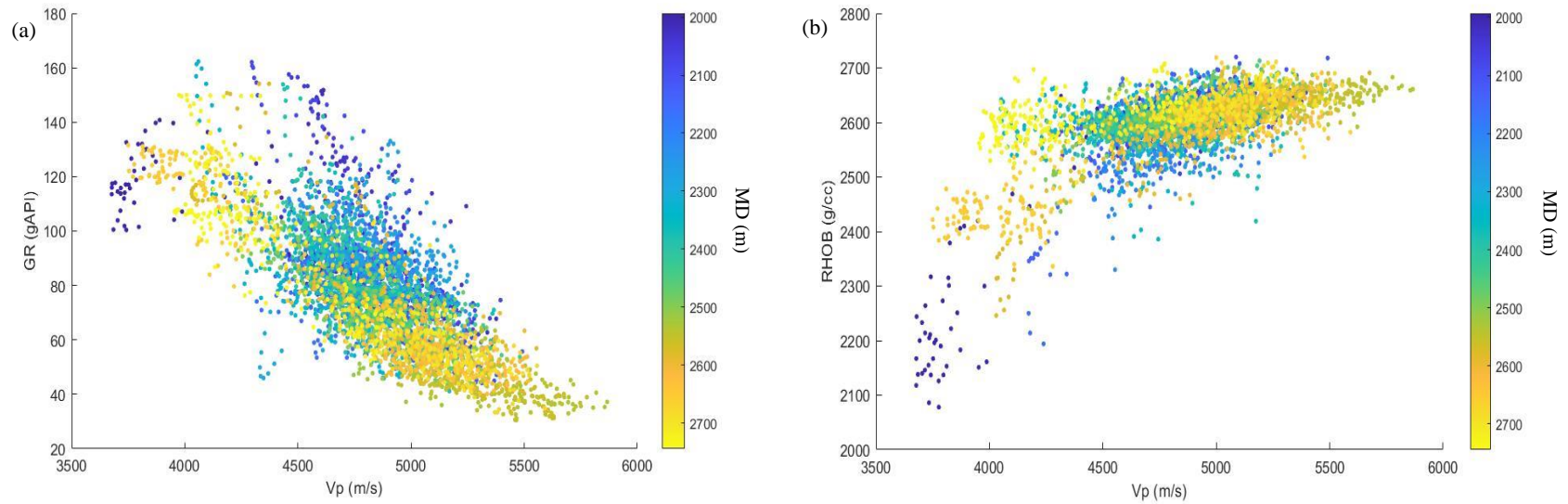


Figure 6-5: The cross-plot analysis of the well log data from PH-1 well within the Bowland Shale Formation range with MD as the colour-coding. (a) shows the cross-plot between GR and V_p , while (b) shows the cross-plot between RHOB and V_p .

Figure 6-6 shows the $\lambda\rho - \mu\rho$ cross-plots of the PH-1 well log data. As explained in Chapter 2, $\lambda\rho$ and $\mu\rho$ are the parameters that relate to the brittleness and total organic content (TOC); therefore, $\lambda\rho - \mu\rho$ cross-plot are commonly used to characterize reservoirs. Figure 6-6(a) shows that the $\lambda\rho - \mu\rho$ cross-plot is able to distinguish lithofacies differences within the well. The data from the shallower formations above the Variscan Unconformity are represented by blue colour. The data from the formations between the unconformity and the Bowland Shale Formation are mostly plotted in cyan colour.

In comparison with other formations, the data from Bowland Shale Formation are mostly located in the zone of low $\lambda\rho$ and high $\mu\rho$ values, represented by yellow and orange dots in Figure 6-6(a). This implies that the formation is very brittle, and therefore productive, with high recovery factor (RF) and expected ultimate recovery (EUR), according to the template established by Alzate & Devegowda (2013). Figure 6-6(b) and 6-6(c) display the $\lambda\rho - \mu\rho$ cross-plot from PH-1 well with Young's modulus (E) and Poisson's ratio (ν) as the colour-coding. The cross-plots show distinct trends of E and ν on the $\lambda\rho - \mu\rho$ cross-plot: the E values increase towards the top side of the graph, and the ν values increase towards the right side of the plot. The data from the Bowland Shale Formation are plotted in the positions with high E and low ν , which are considered to be favourable for successful hydraulic fracture placement (Goodway et al., 2010; Chopra et al., 2012; Perez & Marfurt, 2013).

Figures 6-6(d) to 6-6(f) display only the data from the Bowland Shale Formation. The Upper and Lower Bowland Shale Formations have very similar reservoir quality, though some deeper zones in the Lower Bowland Shale Formation have superior reservoir with lower values of $\lambda\rho$ and $\mu\rho$. In addition, the Lower Bowland Shale values have a wider spread, reflecting the fact that it is less homogeneous than the Upper Bowland Shale. Alzate & Devegowda (2013) use

E as a proxy for the TOC as they have a negative relationship to each other. Thus, the most favourable reservoir properties will plot in the bottom left side of the cross-plot with low E , v , and $\lambda\rho$ as displayed by the red ellipse in Figure 6-6(e).

Figure 6-7 illustrates the $\lambda\rho - \mu\rho$ cross-plot from PNR-1 well. Again, the values from both Upper and Lower Bowland Shale Formations tend to be in the same area, implying that they have very similar reservoir quality. However, the strata below 2,500 m tend to be found within the zones of high reservoir quality (red polygon) more often than for shallower levels. This suggests that targeting these deeper layers would have a potential to produce a higher yield.

Figure 6-8 shows the position of the Bowland Shale on a $\lambda\rho - \mu\rho$ cross-plot with respect to the shale plays from the West Canadian Sedimentary basin and Barnett Shale of the US. The data of the Bowland Shale from PH-1 well are found in the red ellipse towards the top left of the other shale plays, while the data from PNR-1 well are found in the black ellipse. This indicates that the Bowland Shale is comparable to the data from the US and Canada. The data from PH-1 well, specifically, are comparatively more brittle and more porous, with properties that are more dominated by the presence of quartz, than some of these other formations. The data from PNR-1 well, though less brittle, have slightly higher TOC value

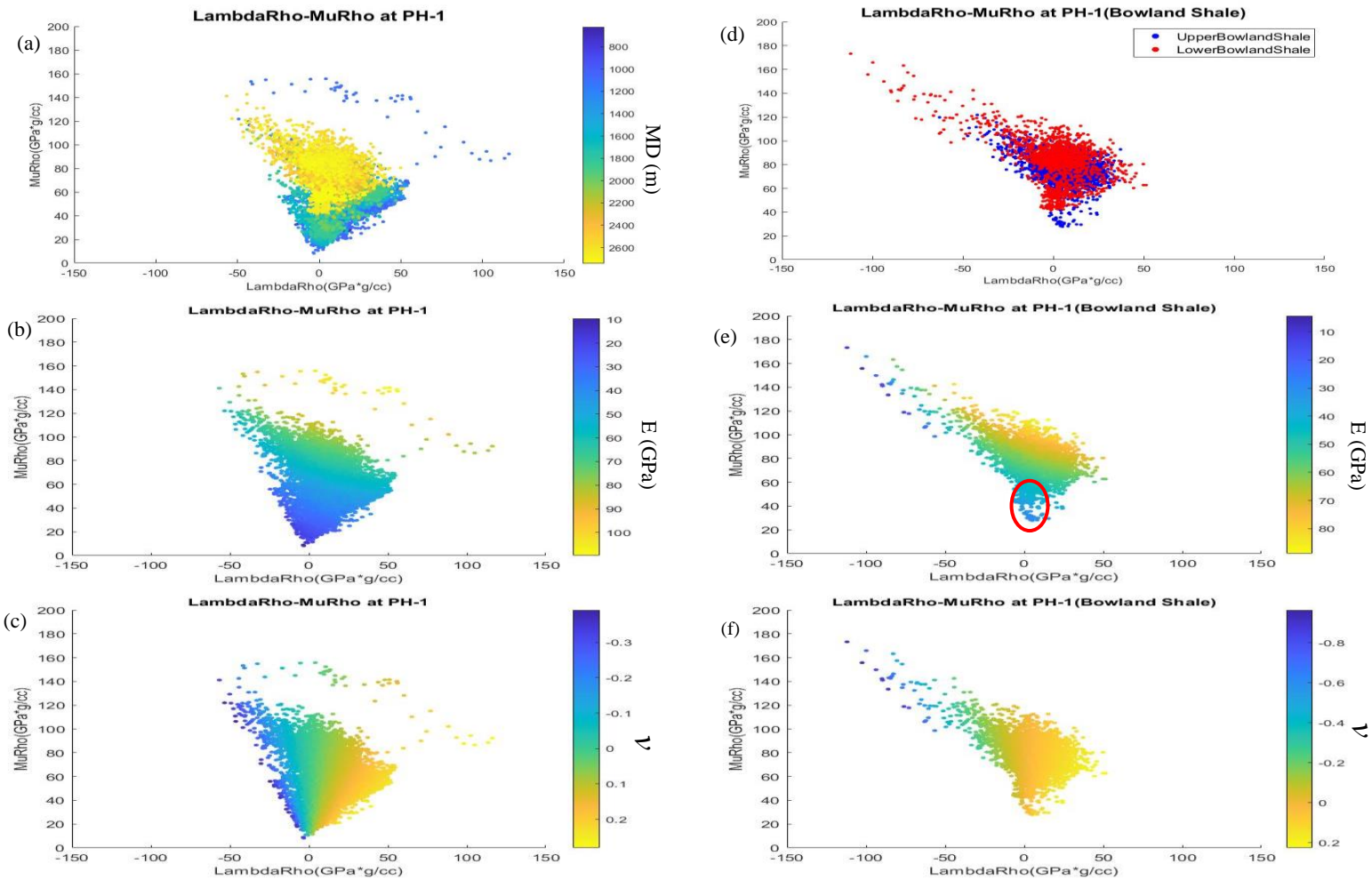


Figure 6-6: $\lambda\rho - \mu\rho$ cross-plot of well log data from the PH-1. (a), (b), and (c) show the cross-plot from the entire well logs with measured depth, E , and ν as the colour-coding. (d), (e), and (f) show the cross-plot of the data in the Bowland Shale Formation. The blue dots in (d) represent the data in the Upper Bowland Shale, while the red dots are the data in the Lower Bowland Shale. (e) and (f) are colour-coded by E and ν . The red ellipse in (e) represents the zones with the highest reservoir quality in the Bowland Shale Formation.

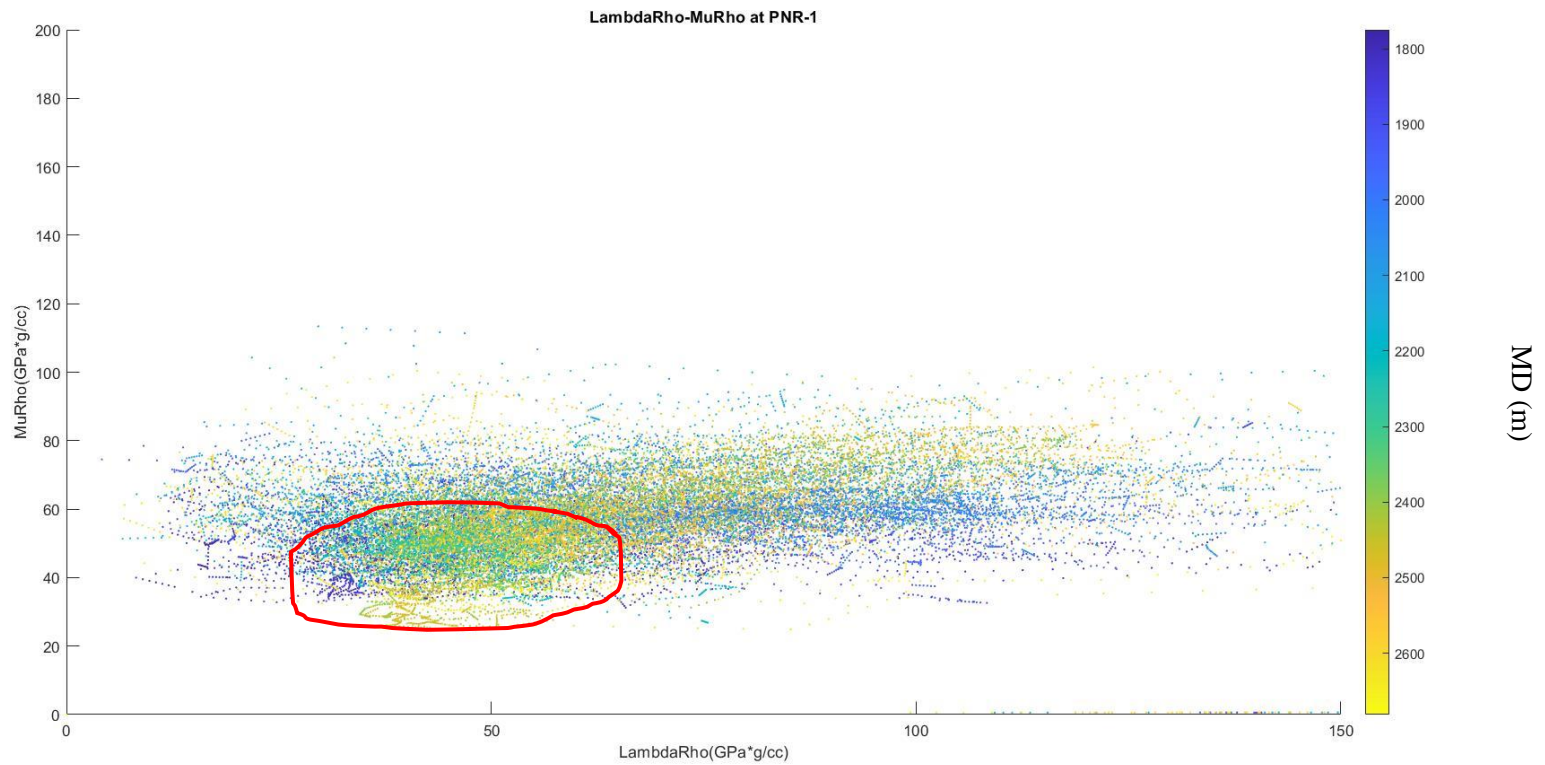


Figure 6-7: $\lambda\rho - \mu\rho$ cross-plot of well log data from the PNR-1 well. The plots are colour-coded by measured depth. The red polygon represents a zone with superior reservoir quality.

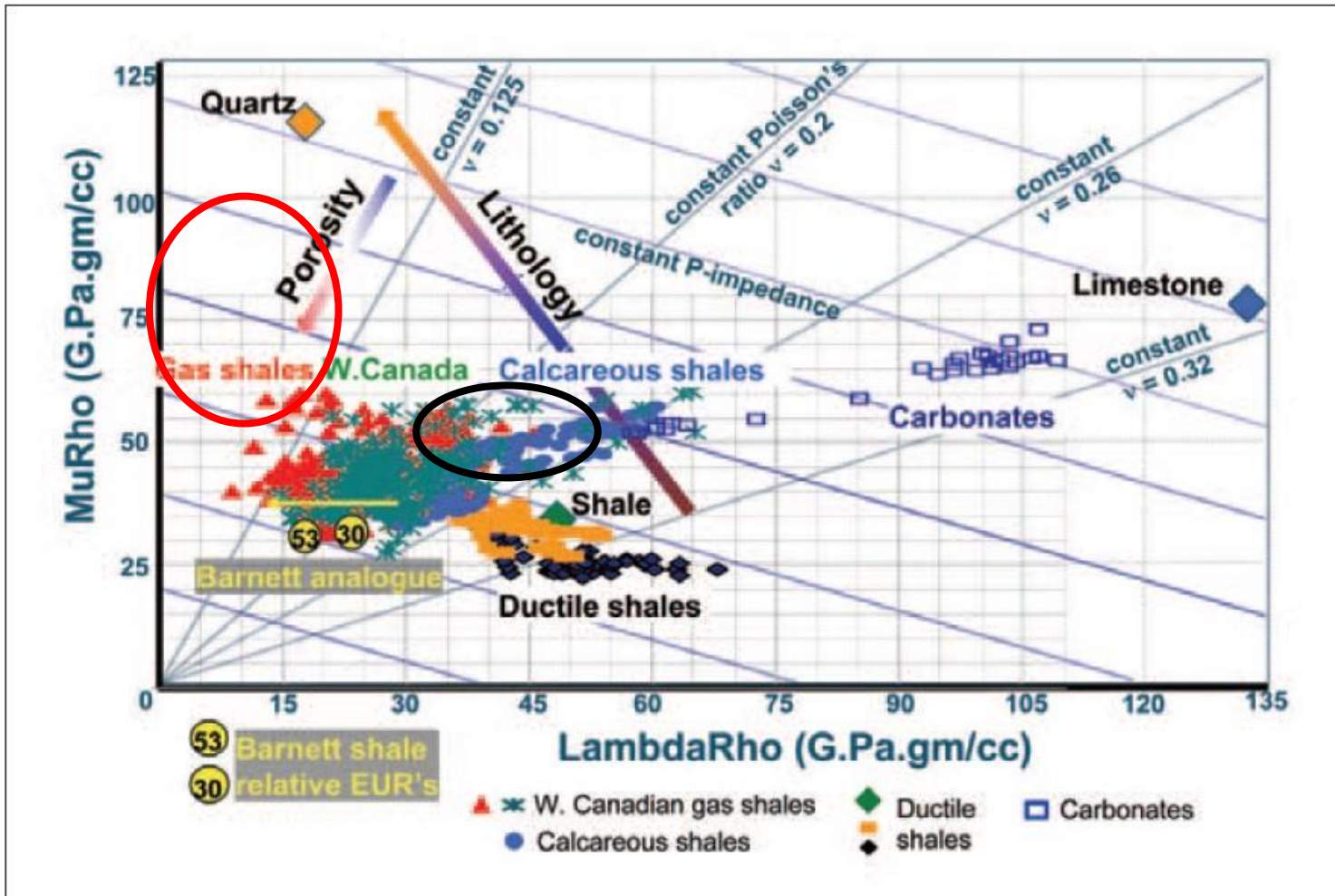


Figure 6-8: $\lambda\rho - \mu\rho$ cross-plot of PH-1 well log data of the Bowland Shale in comparison with the West Canadian shale play and the Barnett Shale of the US. The red ellipse represents the position of the majority of the Bowland Shale data from the PH-1 well. The black ellipse represents the position of the superior reservoir quality data from the PNR-1 well. The figure is derived and adapted from Goodway et al., (2010).

6.3 Well Log Analysis Conclusions

The PCA and cross-plot analysis verify that there is a strong chance that the Bowland Shale is productive. Therefore, further analysis can be performed on the Bowland Shale to find sweet spots in order to maximize the production. However, figure 6-8 shows that there is a large portion of the Bowland shale that has higher brittleness than the shale plays in the USA. This means that there is a high tendency for induced seismicity to occur by the stimulations in the Bowland. This corresponds to the fact that there have been several cases of induced seismicity in the Bowland Shale since the beginning of the operations (eg. Clarke et al., 2019; Kettlety et al., 2020). Thus, careful prospect spot selection is very important in order to avoid triggering felt seismicity. In addition, spots with high TOC but slightly lower brittleness might be taken into consideration as potential drilling spots as the chance of generating felt seismicity is lower in these spots. Therefore, the seismic inversion is necessary to classify the Upper and Lower Bowland Shale based on their productivity and brittleness, using the $\lambda\rho$ - $\mu\rho$ analysis.

Chapter 7: Seismic Inversion and Sweet-Spot Identification of the Bowland

Shale Formation

The classification of reservoir quality for the Bowland Shale, and its spatial variability, is one of the main objectives of this study. The results of the classification can provide insight of sweet spots, which might represent optimal targets for drilling. In this chapter, I use seismic inversion to generate the cubes of Acoustic Impedance (AI), Shear Impedance (SI), and of $\lambda\rho$, and $\mu\rho$ attributes.

7.1 Seismic inversion of Bowland Shale Formation

In this study, I apply a model-based post-stack seismic inversion technique to the Bowland Shale Formation seismic data in order to obtain the acoustic impedance (AI) and shear impedance (SI). The workflow of this process starts with the generation of an initial model and pseudo-wells – in this case I used the PH-1 well logs and picked horizons. Synthetic seismic traces are generated by convolving the reflectivity from the pseudo-wells with a wavelet extracted from the real data. The synthetic seismic traces are then matched with the real seismic traces. The acoustic and shear impedance models are altered over many iterations until the difference between the synthetic and real seismic traces diminishes to a certain threshold.

As a result, this method yields inversion estimates for AI and SI volumes. These cubes can be converted $\lambda\rho$ and $\mu\rho$ cubes, which, as described in the previous chapter, can be useful parameters for sweet-spot identification and indicating rock brittleness and TOC, for example. Figure 7-1 illustrates the workflow of the seismic inversion process that I used on the Bowland seismic cube.

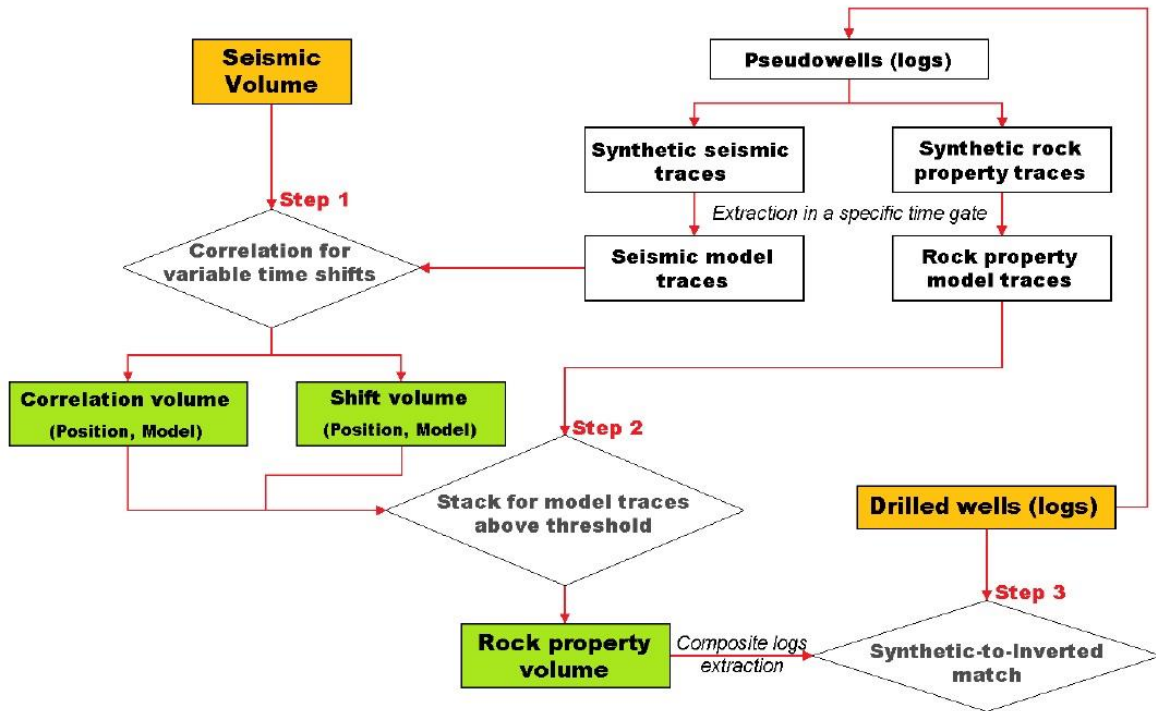


Figure 7-1: The detailed model-based seismic inversion workflow. This figure is derived from the OpendTect 6.0.5 manual.

Figure 7-2 shows the initial model I used from the seismic inversion, compared to the real seismic data. The model was created by using the PH-1 well and the top of the formations such as Manchester Marl, Namurian Upper Rock, Upper and Lower Bowland Shale Formations as the reference. The blank space in the left side of the figure with 1,000 – 1,250 ms TWT is due to the thrust fault that greatly influences the Bowland Shale Formation at this depth. There are 800 generated pseudo-wells scattered throughout the model. Figure 5-3 shows the wavelet used in the seismic inversion. This zero-phased wavelet was extracted from the real seismic data at the PH-1 well.

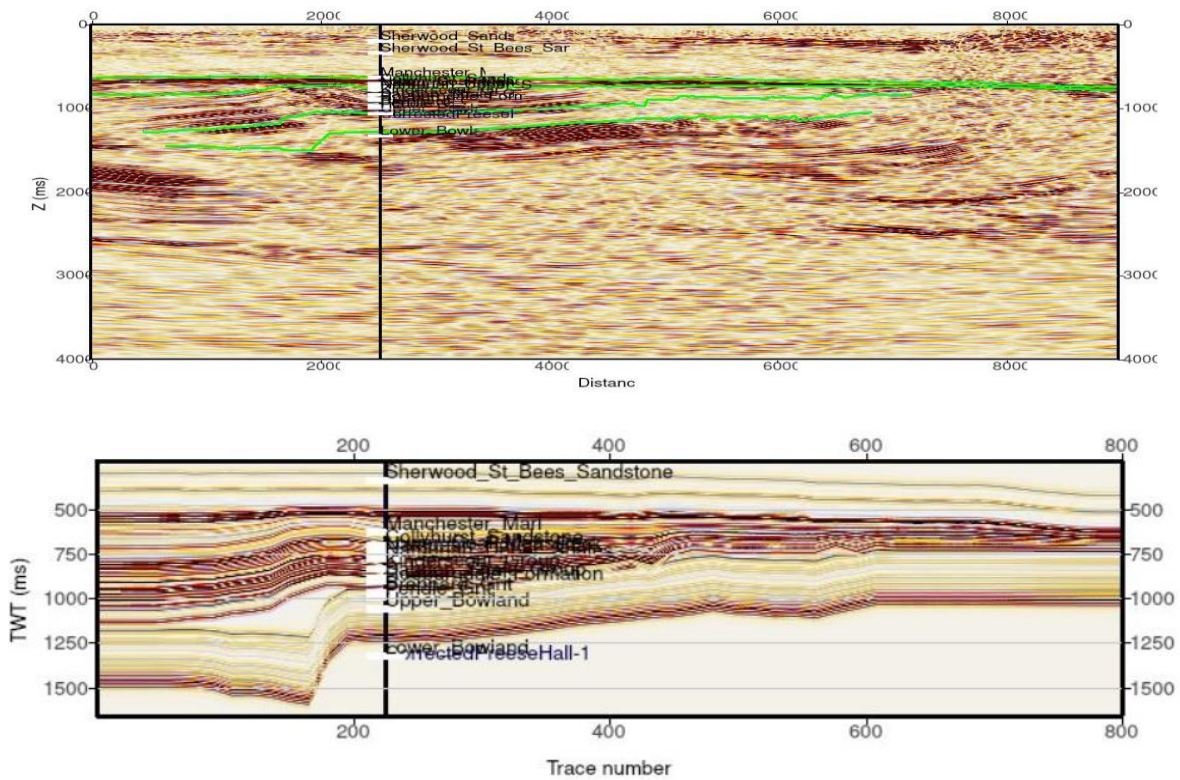


Figure 7-2: The comparison of the real and synthetic seismic data. The upper figure represents the actual seismic data, while the bottom one represents the synthetic data. The vertical black line is the PH-1 well track with horizon markers. The x-axis is distance (m) and trace number, while the y-axis is the two-way travel time (ms)

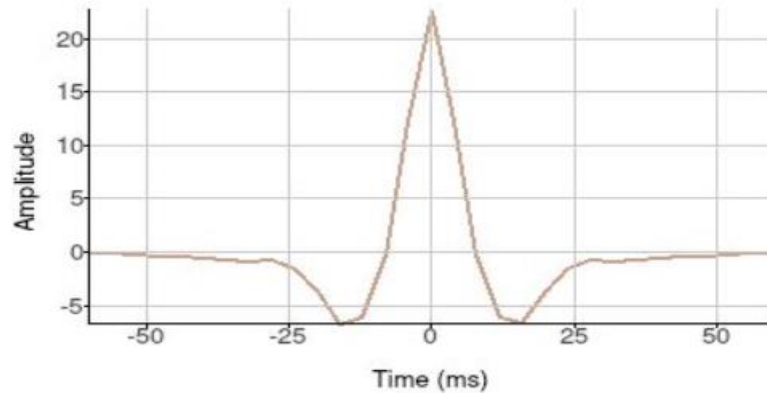


Figure 7-3: The zero-phased wavelet used for the seismic inversion process. It was extracted from at the PH-1 well.

7.2 Seismic inversion results

Four 3D seismic cubes were derived from the seismic inversion. Figures 7-4 and 7-5 show the AI, SI, $\lambda\rho$, and $\mu\rho$ volumes applied on the top of the Upper and Lower Bowland Shale Formations. The ranges of these variables correspond to the PH-1 well logs. In general, the regions with weak and chaotic signals seem to correspond with very high AI, SI, and $\mu\rho$ values, and negative values of $\lambda\rho$, as highlighted in hot colours in Figure 7-4(a), 7-4(b), 7-4(d), 7-5(a), 7-5(b), and 7-5(d), and cold colours in Figure 7-4(c) and 7-5(c). The variables in the areas targeted by the existing wells indicate that they are in the positions that are relatively more optimal for gas extraction.

Figure 7-6 show the AI and SI volumes applied on a vertical slice with the AI and SI well logs from the PH-1 well as the quality control. The outcomes of the inversion correspond to the well logs as the changes in the AI and SI values (in the Bowland Shale Formation range) in the well logs are reflected by the cubes as well.

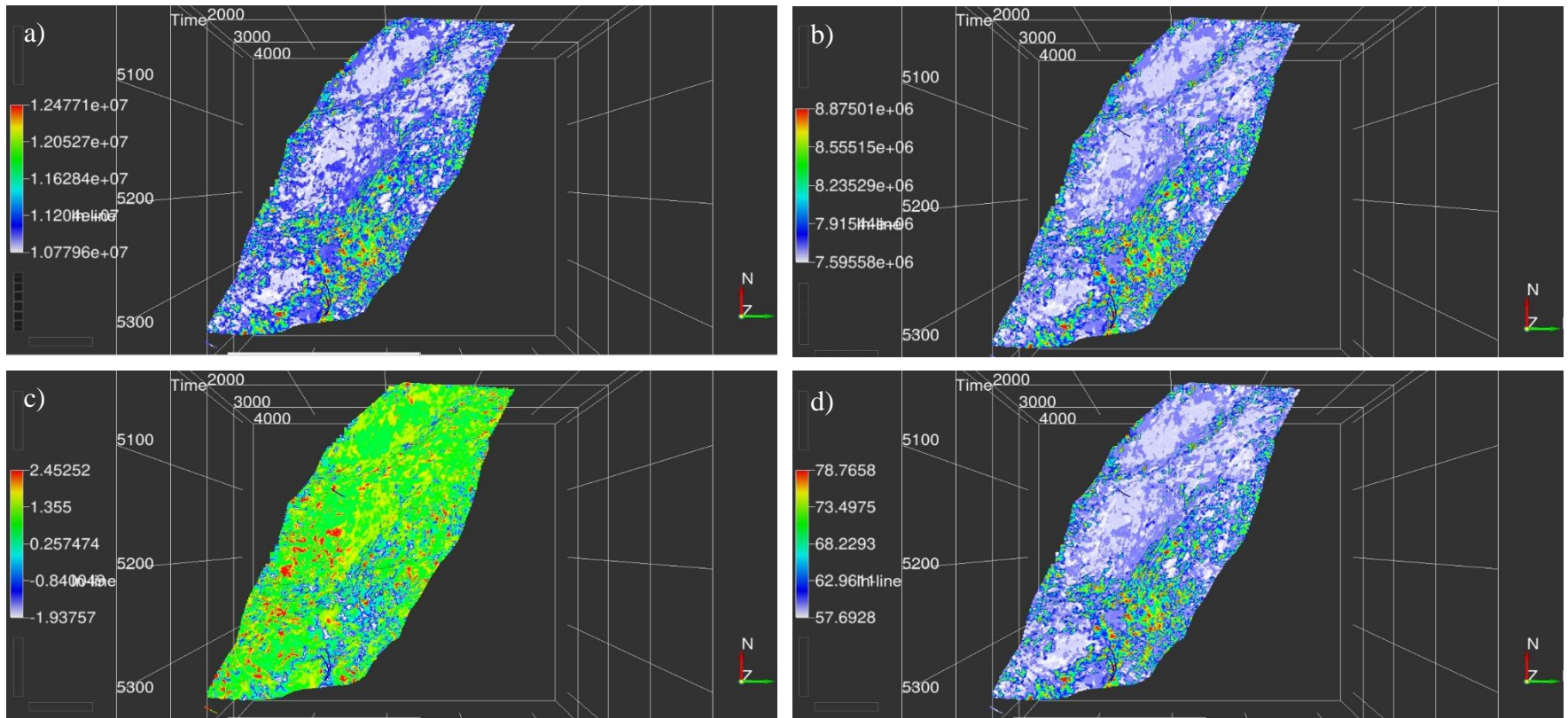


Figure 7-4: The AI , SI , $\lambda\rho$, and $\mu\rho$ volumes from the seismic inversion applied on the top of the Upper Bowland Shale Formation. (a), (b), (c), and (d) represent AI , SI , $\lambda\rho$, and $\mu\rho$ attributes, respectively.

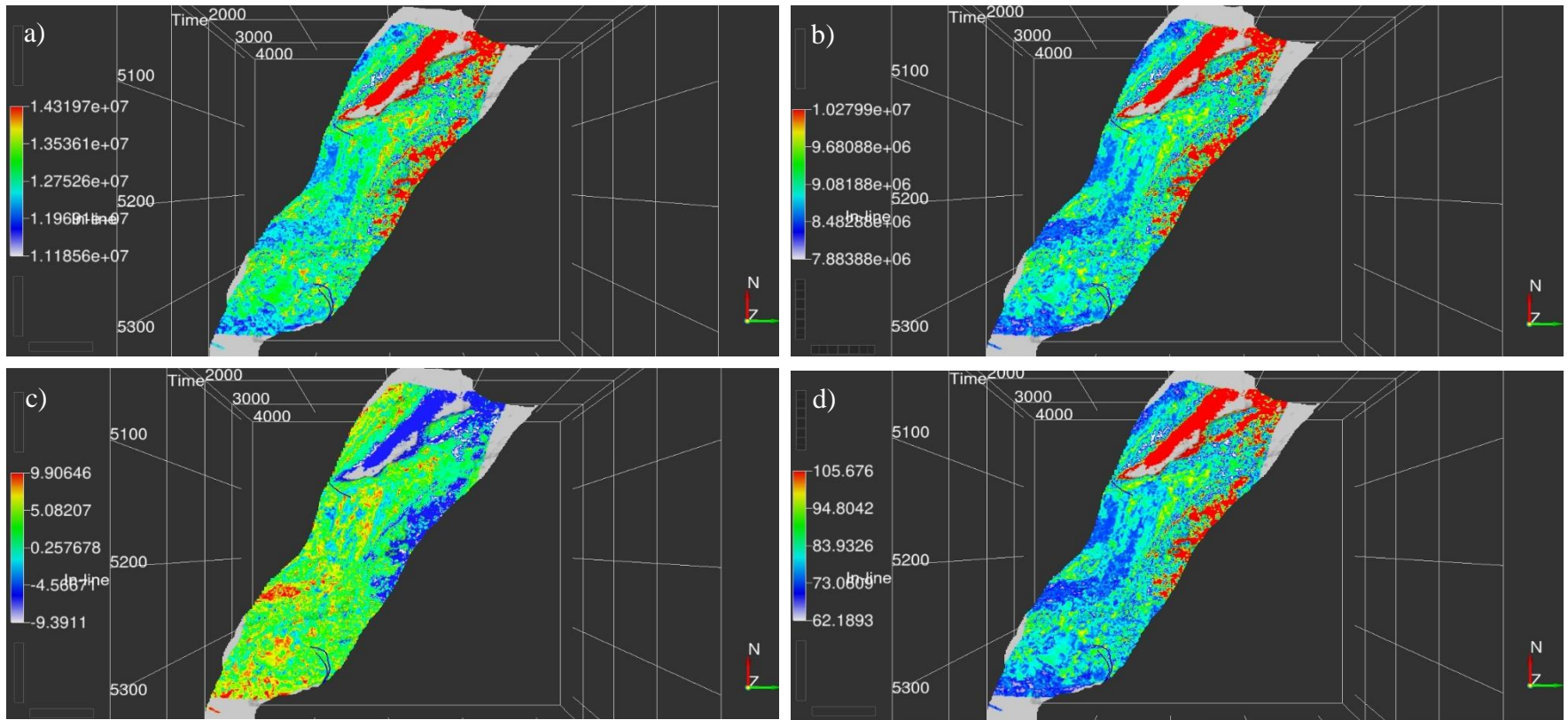


Figure 7-5: The AI, SI, $\lambda\rho$, and $\mu\rho$ volumes from the seismic inversion applied on the top of the Lower Bowland Shale Formation. (a), (b), (c), and (d) represent AI, SI, $\lambda\rho$, and $\mu\rho$ attributes, respectively.

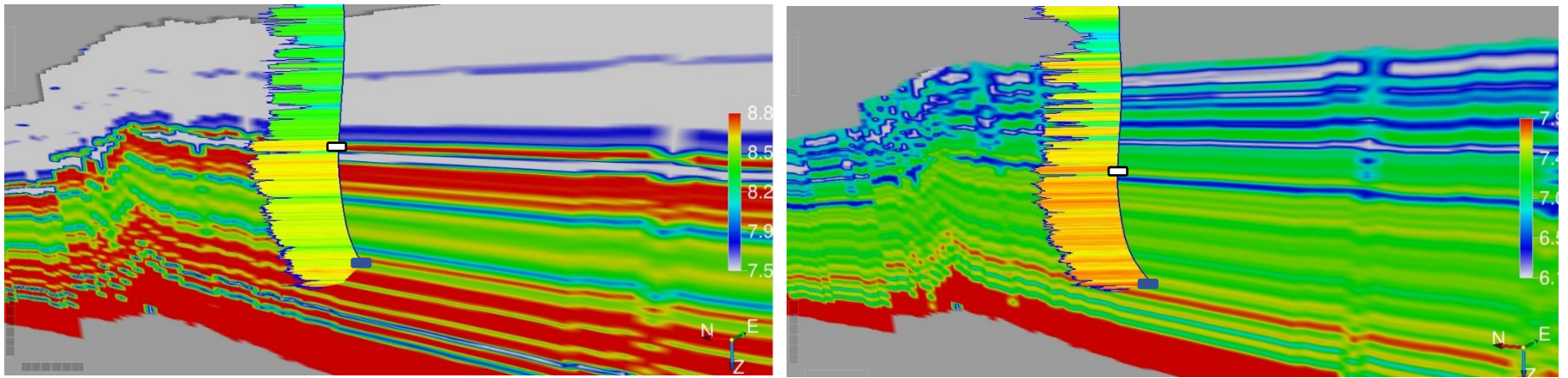


Figure 7-6: The AI and SI volumes applied on a vertical slice with PH-1 well logs. The white marker represents the top of the Upper Bowland Shale Formation, while the blue one is the marker for the top of the Lower Bowland Shale Formation.

7.3 Cross-plot analysis and sweet-spot identification

Figure 7-7 shows a $\lambda\rho - \mu\rho$ cross-plot analysis of the Upper and Lower Bowland Shale Formations as extracted from the inverted cubes. The $\lambda\rho$ and $\mu\rho$ values from the seismic inversion fall into the similar ranges to the well log data in Chapter 6. Figure 7-8 to 7-13 show the projections of the specific areas of the cross-plot on the Upper and Lower Bowland Shale horizons. The data are classified into 3 groups based on their richness and brittleness. Figure 7-8 represents the first group, or zones with the most superior reservoir quality of the Upper Bowland Shale Formation. They are mostly located near the existing wells: PH-1, GH-1z, TH-1, and PNR wells. There are some regions in-between these wells (labelled by the red ellipses in Figure 7-8) that have the similar reservoir quality, which might be considered as potential exploration locations. Figure 7-9 shows the second group of zones with high organic content, but less brittle. They appear to be either surrounding the first group of data or located randomly around the Upper Bowland Shale Formation. Figure 7-10 shows the areas with high brittleness, but low organic content. The data from this final group are mostly located in the chaotic zones. It should be noted that, since dense fracturing will also affect seismic velocities, the values obtained in these areas may represent more intensely fractured rocks around the major faults in this area, rather than a change in the lithological properties of the rock itself. A detailed study into the impacts of natural fractures on seismic properties within the Bowland Shale is beyond the scope of this thesis.

Figure 7-11 to 7-13 show the data from the cross-plot projected on their locations on the Lower Bowland Shale Formation. They are also classified into 3 groups like the Upper Bowland Shale Formation. The sweet spots in this formation are revealed in Figure 7-11 as they have relatively lower $\lambda\rho$ and $\mu\rho$ values. Similarly, they are mostly located near the already established

wells; however, there are some rich spots (labelled by the yellow ellipses in Figure 7-11) that are not associated with these wells. Figure 7-12 shows the second group with high organic content, but low brittleness. They seem to be randomly scattered around the Lower Bowland Shale Formation, but most of them are not found in the chaotic zones. The white ellipses in Figure 7-12 represents clusters of this second group that are located next to the sweet spots not associated with the established wells. These spots might be the potential prospective locations for further exploration. Figure 7-13 shows that the sweet spots in Figure 7-11 are also associated with the group with high brittleness but lower organic content, as both groups are located in similar positions.

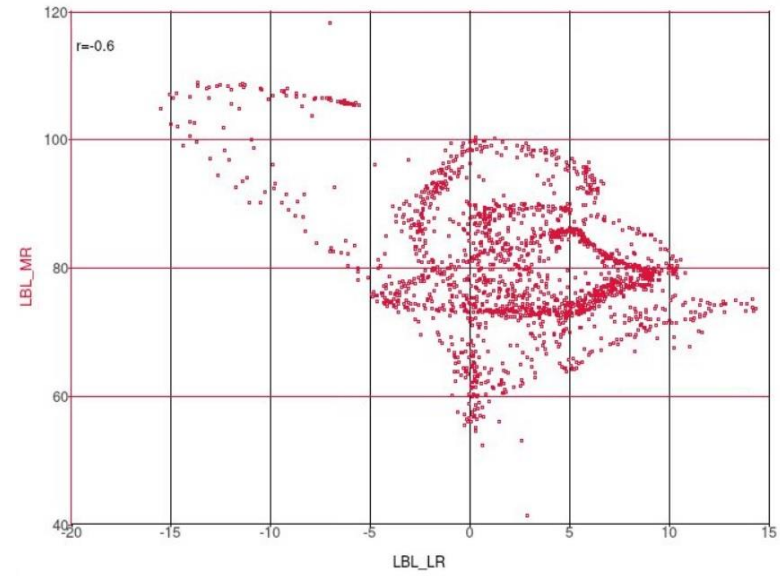
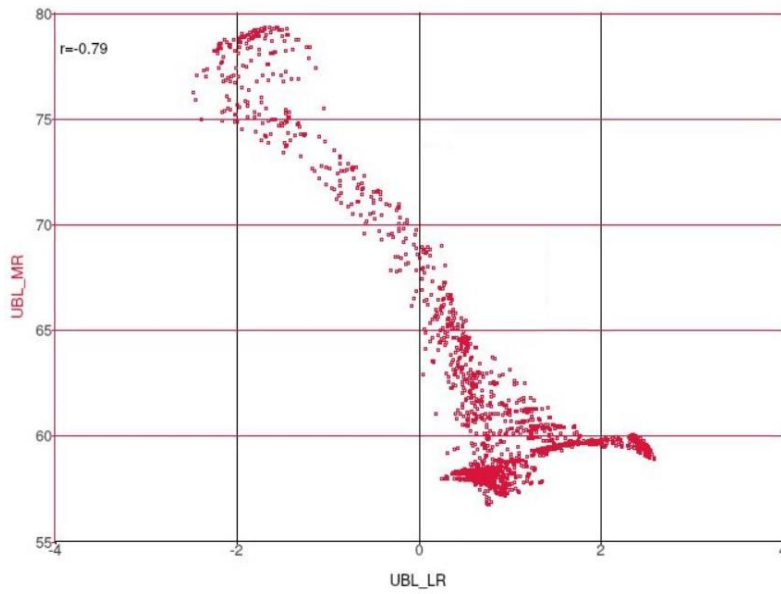


Figure 7-7: The $\lambda\rho - \mu\rho$ cross-plot of the top of the Upper and Lower Bowland Shale Formations. (a) represents the cross-plot of the Upper Bowland Shale Formation, while (b) shows the cross-plot of the Lower Bowland Shale Formation.

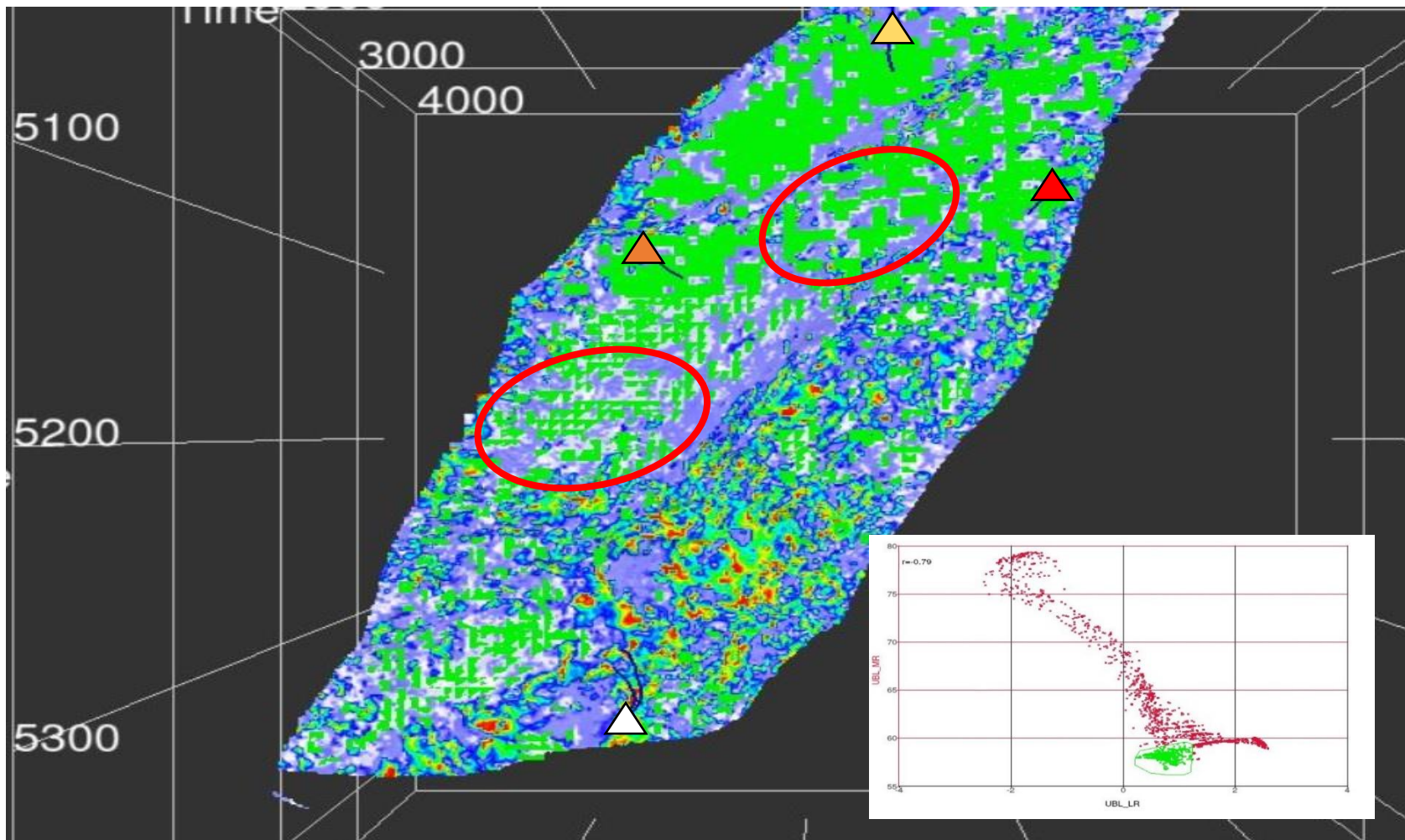


Figure 7-8: The classified first group of the data from the Upper Bowland Shale Formation projected on the top of the Upper Bowland Shale horizon. The yellow, orange, red, and white triangles represent the top of GH-1z, PH-1, TH-1, and PNR wells. The well tracked are marked with the dark blue lines. The red ellipses show the potential prospective locations.

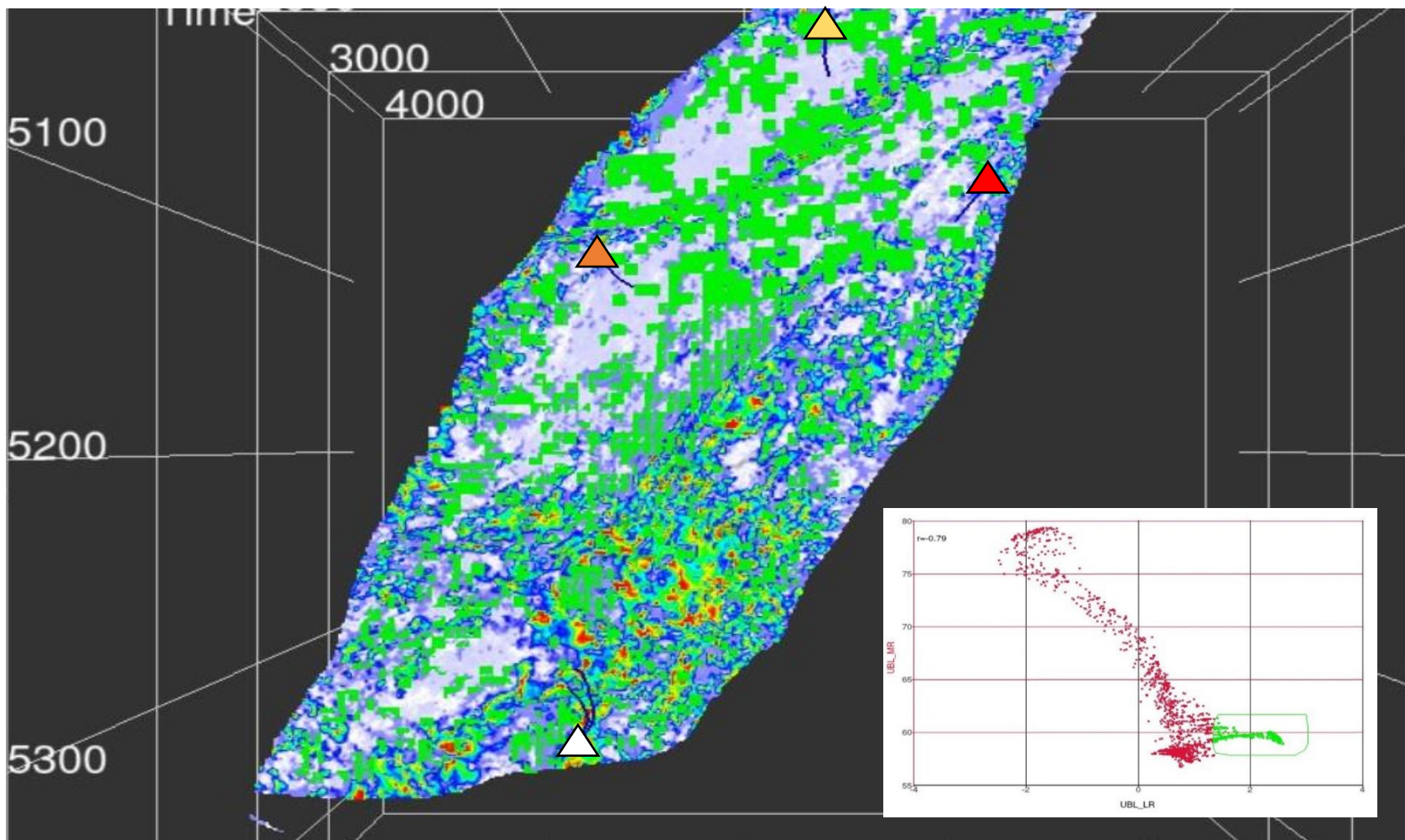


Figure 7-9: The second group of the data from the Upper Bowland Shale Formation projected on the top of the Upper Bowland Shale horizon. The yellow, orange, red, and white triangles represent the top of GH-1z, PH-1, TH-1, and PNR wells. The well tracked are marked with the dark blue lines.

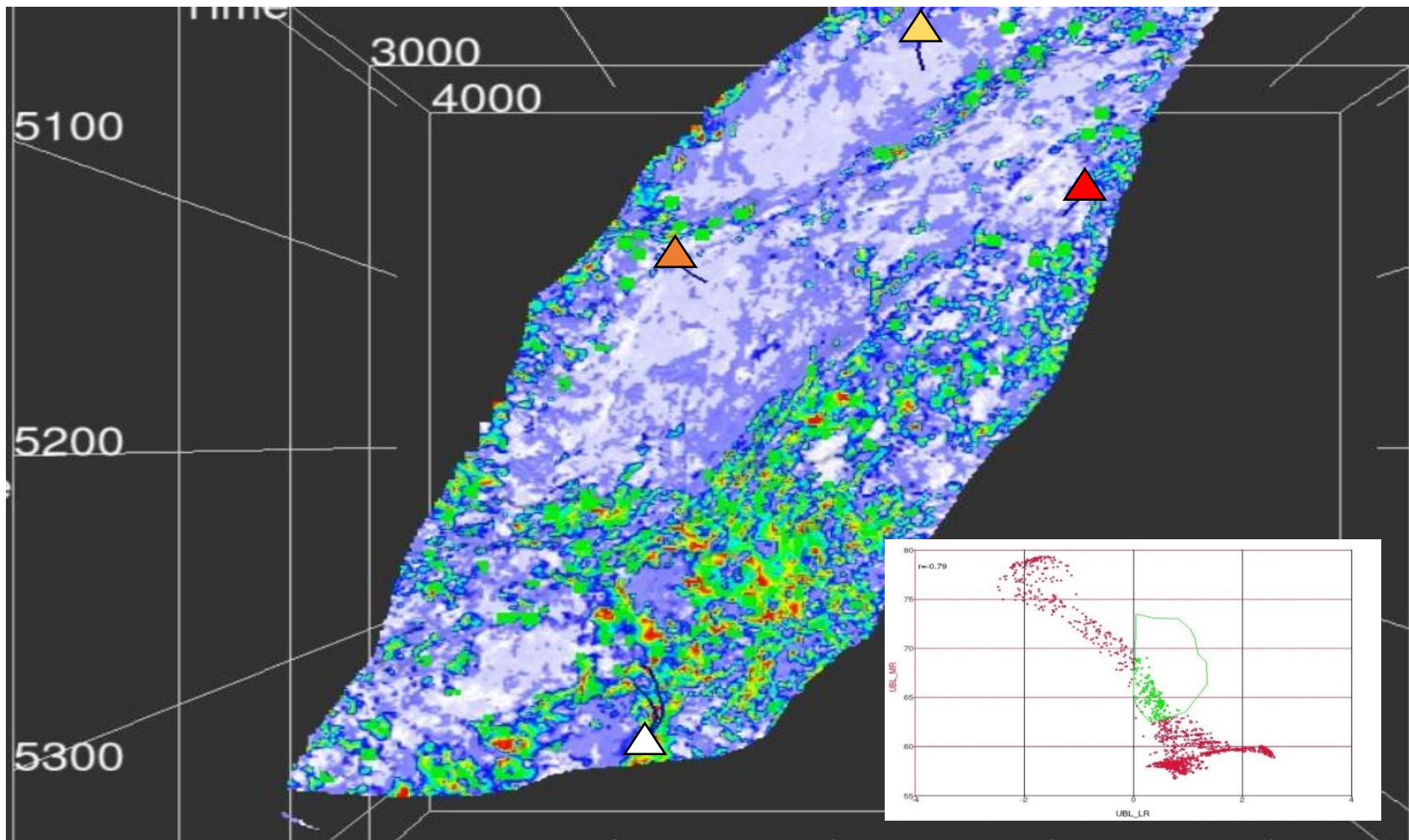


Figure 7-10: The third group of the data from the Upper Bowland Shale Formation projected on the top of the Upper Bowland Shale horizon. The yellow, orange, red, and white triangles represent the top of GH-1z, PH-1, TH-1, and PNR wells. The well tracked are marked with the dark blue lines.

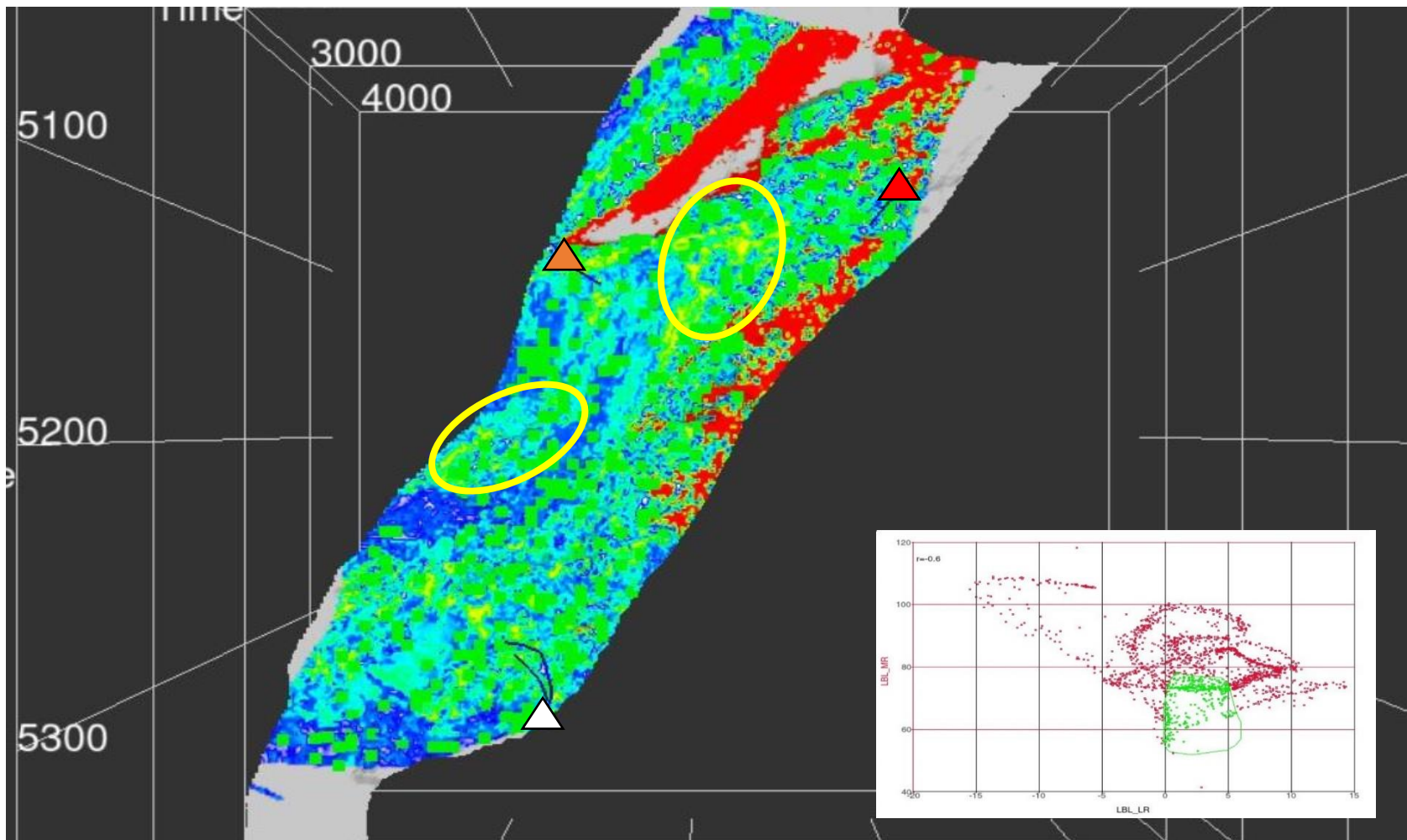


Figure 7-11: The first group of the data from the Lower Bowland Shale Formation projected on the top of the Lower Bowland Shale horizon. The orange, red, and white triangles represent the top of PH-1, TH-1, and PNR wells. The well tracked are marked with the dark blue lines. The yellow ellipses show the potential prospective locations.

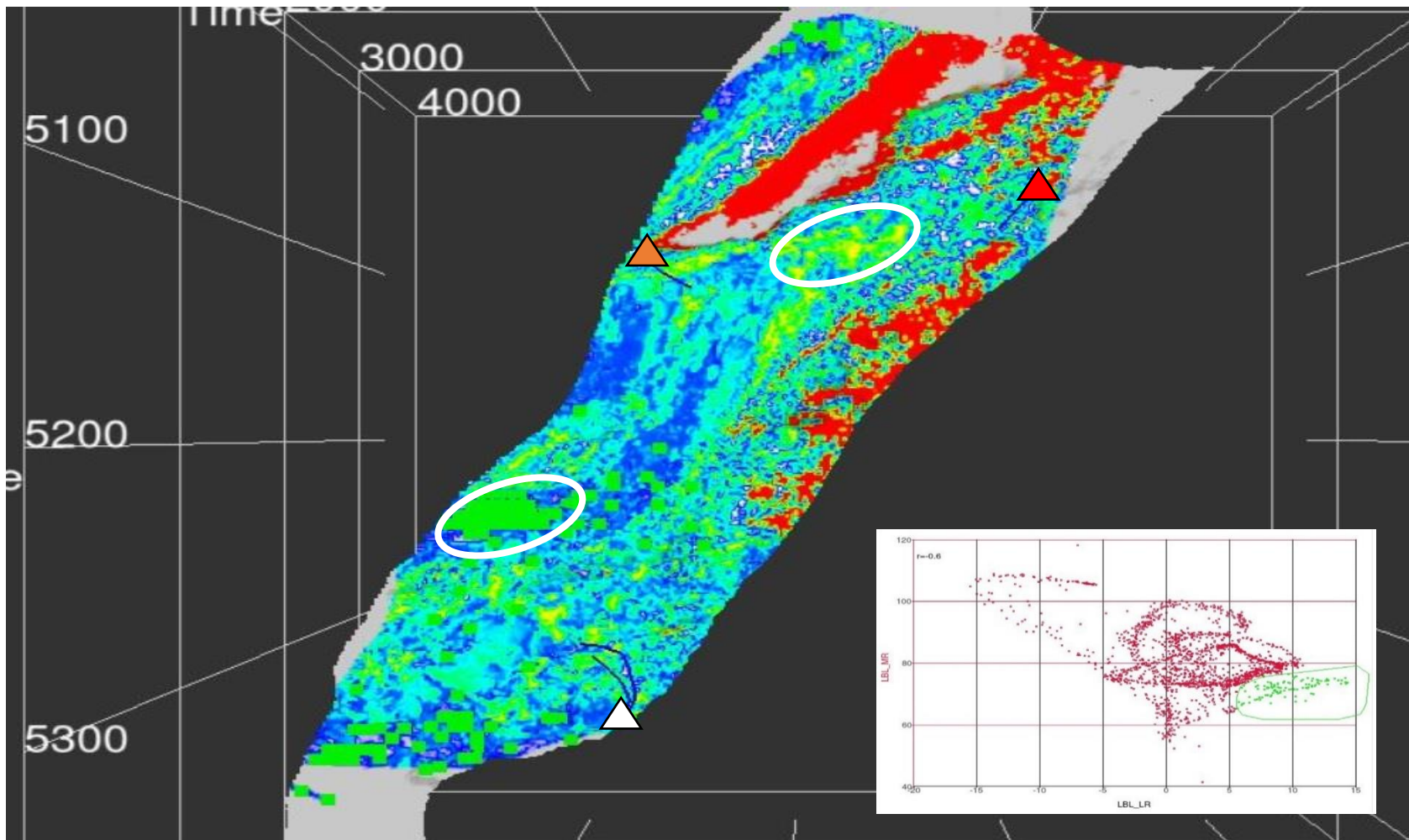


Figure 7-12: The second group of the data from the Lower Bowland Shale Formation projected on the top of the Lower Bowland Shale horizon. The orange, red, and white triangles represent the top of PH-1, TH-1, and PNR wells. The well tracked are marked with the dark blue lines. The white ellipses show the clusters of the data from the second group that are located near the sweet spots.

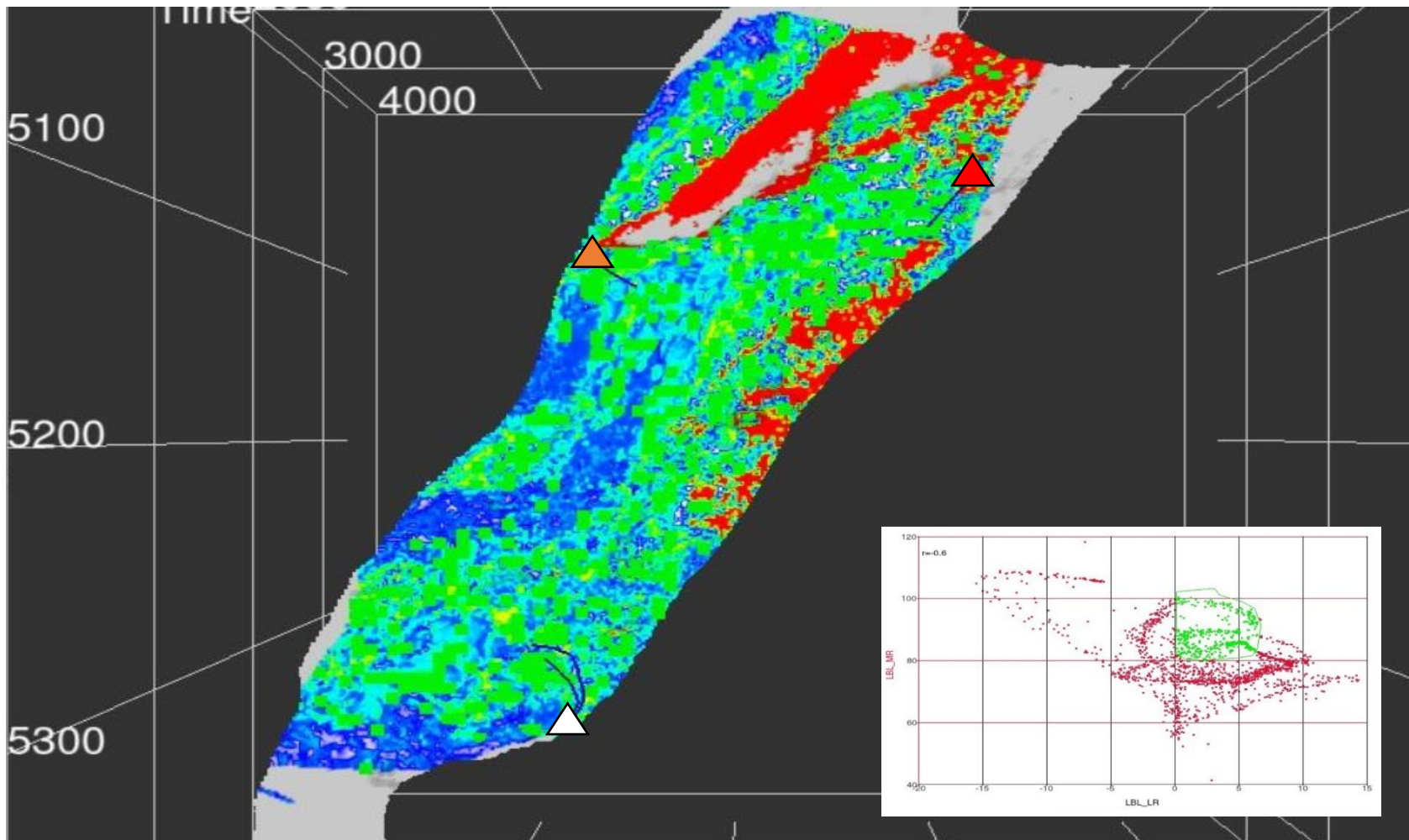


Figure 7-13: The third group of the data from the Lower Bowland Shale Formation projected on the top of the Lower Bowland Shale horizon. The orange, red, and white triangles represent the top of PH-1, TH-1, and PNR wells. The well tracked are marked with the dark blue lines

7.4 Conclusions

According to the seismic inversion results and cross-plots, the sweet spots in the Bowland Shale correspond to areas that have already been targeted by the existing wells (PH-1, GH-1z, TH-1, and PNR wells). These locations are likely to be optimal for gas extraction due to their high TOC and brittleness, as represented by low $\lambda\rho$ and $\mu\rho$ values. In addition, 2 undrilled sweet spots are found in this study. They are located between the PH-1 and PNR wells, and PH-1 and TH-1 wells as shown previously. However, they appear to have relatively higher proportions of rich, ductile shales (higher values of $\lambda\rho$). These spots have a potential to be prospective areas in the future, given the issues with induced seismicity in the Bowland Shale. Targeting more ductile portions of this unit may help mitigate this issue, since more ductile rocks are less likely to generate high levels of induced seismicity.

However, the results can be more accurate if the initial model is improved. The initial model used in this work, although can mostly represent geological features and horizon locations, does not reflect the influence of the large thrust fault near the PH-1 well on this region. This is shown by the black space in Figure 7-2, as mentioned before. This might affect the seismic inversion and potentially cause errors since the location of each horizon in the initial model and in the actual seismic data might not be the same. Some errors are observed in the seismic inversion results, for example, the areas with anomalously high AI, SI, and $\mu\rho$, and low $\lambda\rho$ in the upper part of the upper Bowland Shale horizon in Figure 7-5, 7-11, 7-12, and 7-13. The results would be more precise with the improved initial model that can reflect all of the geological features in the region. Therefore, a future work that creates an accurate initial model is necessary.

Chapter 8: Discussion

The well log analysis including PCA and the cross-plot analysis provides insights regarding the productivity and brittleness of the Bowland Shale Formation. It verifies that a large portion of the Bowland Shale Formation is suitable for unconventional exploration (Figure 6-6 and 6-7 in Chapter 6). The $\lambda\rho$ - $\mu\rho$ cross-plots from the PH-1 and PNR wells show that the Bowland Shale is both productive and brittle, comparable to the famous Barnett Shale of the USA (Figure 6-8 in Chapter 6). Thus, the further study of the Bowland Shale is important for gas exploration in the UK.

Additionally, this study also shows that there is a significant portion of the Bowland Shale that is more brittle than the Barnett Shale. There is no denying that the high brittleness facilitates the gas exploration of the Bowland Shale since brittle shales are easier to break down by hydraulic fracturing, allowing more gas to escape. However, the main problem with the highly brittle Bowland Shale is that there is a higher chance to trigger felt seismicity, which can cause damages to buildings and lives. Therefore, the 3D seismic data investigation for potential faults that can rupture is important.

The results from the fault investigation using the 3D reflection seismic data and the seismic attributes in Chapter 5 show only vague existences of the potential causative faults identified at the PNR wells. The lack of obvious presences of the reactivated faults in this study means that planning drilling locations for unconventional explorations should be taken more seriously since there is a possibility that faults do not show up on 3D seismic data or attributes, similar to this study. In addition, the Traffic Light Scheme (TLS) is still important for mitigating damages from induced seismicity. The TLS combined with the spontaneous seismic monitoring

allows operators to shut down the operation as soon as or before any large seismicity occur. However, using 3D reflection seismic data and seismic attributes to investigate drilling targets before actually drilling them should still be performed. This is because there is still a chance to find strike-slip faults using similar methods, as many studies have shown before (eg. Ma et al., 2019; Pico et al., 2014).

The future work for strike-slip investigation is still necessary for efficient explorations. One way to possibly improve the investigation is the application of multi-attribute. Analyzing multiple weighted attributes at the same time seems to improve the fault investigation, instead of analyzing only an individual seismic attribute (Kluesner & Brothers, 2016). The multi-attribute approach could distinguish different geological features such as faults, salt bodies, and gas chimneys (Kluesner & Brothers, 2016). Therefore, applying this multi-attribute analysis onto the Bowland Shale data set might help in the causative fault investigation. Additionally, multiple attributes can be blended to produce an improved attribute, which might provide a more integrated view of the 3D seismic data (Marfurt, 2015). This can be achieved by selecting attributes which are mathematically independent to each other, but they are correlated through the geology (Marfurt, 2015). This shows that there are still many possibilities for improving the strike-slip fault investigation.

Investigating targeting areas beforehand can also prevent severe damages from induced seismicity. The seismic inversion can indicate the productivity and brittleness of each locality in the Bowland Shale. It does not only reveal sweet spot within the Bowland Shale, but also detect any spots that are less likely to produce dangerous felt seismicity. These spots are productive enough but have slightly lower brittleness, which lowers the chances of inducing seismicity from hydraulic fracturing. Extracting resources from these spots will become the next challenge in the

future since they are slightly safer to drill, and most of the sweet spots in the Bowland Shale are already drilled. In addition, with the lower brittleness, fracking these spots to produce the highest amount of gas possible might become an interesting research topic in the future as well.

Chapter 9: Conclusions

Gas-bearing shales have become a targeted source of hydrocarbon, replacing production as other conventional sources have started to decline. The Carboniferous Bowland Shale Formation has proven to be one of the most potentially productive unconventional sources for extraction in the UK. It consists of 2 sub-units: the Upper and Lower Bowland Shale Formations, both of which have high brittleness and TOC. The Lower Bowland Shale Formation, in particular, is of more interest as it has higher expected gas volume and mostly undrilled. There is a significant amount of deformation in the study area, as a result from the Variscan Orogeny, thermal subsidence, and rifting. The repeated occurrence of induced seismicity has posed a major challenge for the development of this resource.

The 3D seismic data used in this study was acquired from the Fylde Peninsula in western Lancashire between Preston and Blackpool, UK. Analysing these 3D seismic data reveals geological horizons and structures that were heavily influenced by the Variscan orogeny. In this area, there are two main sets of faults with different senses of motion. The first group consists of thrust faults generated before or during the Variscan Orogeny, while the second group consists of normal faults that occurred during Carboniferous rifting, Pennsylvanian thermal subsidence, and Permian-Triassic basin subsidence. The overlying horizons from the surface to the Variscan unconformity are relatively flat. The Variscan unconformity is marked by the bottom of Manchester Marl, against which older horizons truncate. Below the unconformity, there is a distinct antiform associated with small faults near the PH-1 well. The signals from the area below this are relatively more chaotic as a result from faulting and other geological structures.

Bowland Shale exploration was disrupted due to induced seismicity in 2018 and 2019. This study shows that the faults that generated these events are not visible on the 3D seismic data. Therefore, I attempted to find these faults by using the seismic attributes including similarity, spectral decomposition, and curvature. This study was done to assess whether more advanced seismic attributes could be used to detect faults before they are reactivated, thereby mitigating felt-seismic events. Some attributes did identify the potential for hidden faults for the PNR site; however, without the data regarding the locations of the actual causative faults, it was difficult to distinguish them from noises and signals from small fractures. The results from this study indicate that the 3D seismic data and seismic attributes, including similarity, curvature, and spectral decomposition, alone cannot be relied upon to identify faults that could be reactivated, causing induced seismicity. This is most likely because the causative faults in this study are subtle transform faults, which do not cause obvious vertical displacement. Even though this study might not completely reflect other explorations in different regions, it still shows that there is a possibility that faults generating felt seismicity are not picked up by the seismic attributes. Therefore, the Traffic Light Scheme is still necessary in order to mitigate potential damages caused by unexpected induced seismicity.

I also combined well logs from PH-1 and PNR-1 wells with seismic observations to investigate the spatial variability in Bowland Shale properties. I examined various well log properties to assess the reservoir quality of the Bowland Shale Formation. The abrupt changes in these logs in response to the changes in lithologies are clearly shown as boundaries between different horizons. V_p/V_s ratios in the Bowland Shale Formation are relatively lower than the other units, suggesting the possibility that this unit is bearing a higher amount of gas. The non-homogenous nature of the Lower Bowland Shale is reflected by the highly variable log data,

compared to the upper unit. The $\lambda\rho - \mu\rho$ cross-plots of the PH-1 and PNR-1 well logs indicate that the reservoir quality of the Bowland Shale is mostly optimal for gas exploration and is comparable to North American shale plays such as the Barnett Shale and the West Canadian shale play. Application of statistical techniques such as PCC and PCA reveals that, for the entire PH-1 well log, most properties seem to have linear relationship to each other except for GR. The possible explanation for this is that other parameters vary with the changing depth, while GR only relates to the lithology. The PCC result for the PH-1 well log within the range of the Bowland Shale Formation shows a slight difference as only GR and RHOB that do not linearly correlate will with each other. The possible culprit is the presence of gas which can cause changes the RHOB log, but not as much in the GR log. The PCC result from PNR-1 well shows a much better correlation of GR to other parameters, as a result of the much smaller depth range compared to the PH-1 well data. The PCA results for the PH-1 and PNR-1 well logs show similar trends where the primary principal component is heavily dominated by GR and the secondary principal component is dominated by DT and DTS. This means that the deviations in these data can be explained mostly by the changes in GR logs, which reflects the changes in lithologies.

Combining PH-1 well data and the 3D seismic data cube, seismic inversion has been utilized in this study to reveal physical properties and locate potential sweet spots, which are the most productive spots with high brittleness, porosity, and TOC parameters, within the Bowland Shale Formation. I generated and analysed the Acoustic Impedance, Shear Impedance, and $\lambda\rho$, and $\mu\rho$ cubes, as products from the inversion. The results suggest that most sweet spots are already associated with the existing wells such as PH-1, GH-1z, and PNR wells. However, there are potentially high-yielded, undrilled zones as well. The most promising ones are located

between PH-1 and PNR wells, and between PH-1 and TH-1 wells. The reservoir quality in these areas can be compared to other sweet spots within the Bowland Shale, but they seem to have higher amount of ductile shale content associated with them. The existing wells, which have caused induced seismicity, have targeted some of the more brittle zones within the Bowland Shale. Since induced seismicity may be promoted by fracturing in more brittle rocks, exploration within more ductile portions of the Bowland Shale may in fact be more advantageous from the perspective of reducing the occurrence of induced seismicity, which so far has proven to be one of the major challenges for the development of this resource.

References

- Alzate, J. H., & Devegowda, D. (2013). Integration of surface seismic, microseismic, and production logs for shale gas characterization: Methodology and field application. *Interpretation*, 1(2). doi: 10.1190/int-2013-0025.1.
- Anderson, I. & Underhill., J. R. (2020). Structural Constraints on Lower Carboniferous Shale Gas Exploration in the Craven Basin, NW England. *Petroleum Geoscience*, 26(2):303. doi: 10.1144/petgeo2019-125.
- Andrews, I. J. (2013). The Carboniferous Bowland Shale gas study: geology and resource estimation. British Geological Survey for Department of Energy and Climate Change, London, UK.
- Bahorich, M. & Farmer, S. (1995). 3D Seismic Discontinuity for Faults and Stratigraphic Features: The Coherence Cube. *The Leading Edge*, 14, 1053-1058.
doi:10.1190/1.1437077
- Barbato, U. (2012). Fault Detection Using the Phase Spectra from Spectral Decomposition. The Faculty of the Department of Earth and Atmospheric Sciences. University of Houston
- Cheremisinoff, N. P., & Davletshin, A. R. (2015). *Hydraulic fracturing operations*. John Wiley and Sons.
- Chopra, S. & Marfurt, K. J. (2007). Seismic curvature attributes for mapping faults/fractures, and other stratigraphic features. *Recorder*, 32(9).
- Chopra, S. & Marfurt, K. J. (2008). Emerging and Future Trends in Seismic Attributes. *Society of Exploration Geophysicists*, 27(3). 281-440. doi: 10.1190/1.2896620.

- Chopra, S., Sharma, R. K., Keay, J., & Marfurt, K. J. (2012). Shale gas reservoir characterization workflows. *SEG Technical Program Expanded Abstracts 2012*. doi: 10.1190/segam2012-1344.1.
- Clarke, H., Eisner, L., Styles, P., & Turner, P. (2014). Felt seismicity associated with shale gas hydraulic fracturing: The first documented example in Europe. *Geophysical Research Letters*, *41*(23), 8308–8314. doi: 10.1002/2014gl062047.
- Clarke, H., Verdon, J. P., Kettlety, T., Baird, A. F., & Kendall, J. M. (2019). Real-Time Imaging, Forecasting, and Management of Human-Induced Seismicity at Preston New Road, Lancashire, England. *Seismological Research Letters*. doi: 10.1785/0220190110.
- Cuadrilla Bowland Ltd. (2014). Environmental Statement: Induced Seismicity. *Government of the UK: Environment Agency*.
- Eaton, D.W., N. Igonin, A. Poulin, R. Weir, H. Zhang, S. Pellegrino, G. Rodriguez, (2018). Induced seismicity characterization during hydraulic-fracture monitoring with a shallow-wellbore geophone array and broadband sensors: *Seismological Research Letters*, *89*, 1641-1651.
- Eyre, T.S., D.W. Eaton, M. Zecevic, D. D’Amico, D. Kolos, (2019). Microseismicity reveals fault activation before MW 4.1 hydraulic-fracturing induced earthquake: *Geophysical Journal International*, *218*, 534-546.
- Goodway, B., Chen, T., & Downton, J. (1997). Improved AVO fluid detection and lithology discrimination using Lamé petrophysical parameters; “ $\lambda\rho$ ”, “ $\mu\rho$ ”, & “ λ/μ fluid stack”, from P and S inversions. *SEG Technical Program Expanded Abstracts 1997*. doi: 10.1190/1.1885795.

- Goodway, B., Perez, M., Varsek, J., & Abaco, C. (2010). Seismic petrophysics and isotropic-anisotropic AVO methods for unconventional gas exploration. *The Leading Edge*, 29(12), 1500–1508. doi: 10.1190/1.3525367.
- Hamada, G.M. (2004). Reservoir Fluids Identification Using Vp/Vs Ratio. Oil & Gas Science and Technology-revue De L Institut Francais Du Petrole. *OIL GAS SCI TECHNOL*, 59, 649-654. 10.2516/ogst:2004046.
- Ladislaw, S., Nakano, J., Sieminski, A., & Stanley A. (2017). U.S. Natural Gas in the Global Economy, *Center for Strategic and International Studies*.
- Jahan, I., & Castagna, J. (2017). Spectral decomposition using time-frequency continuous wavelet transforms for fault detection in the Bakken Formation. *Society of Exploration Geophysicists*.
- Keranen, K. M., & Weingarten, M. (2018). Induced seismicity. *Annual Review of Earth and Planetary Sciences*, 46(1), 149–174. <https://doi.org/10.1146/annurev-earth-082517-010054>.
- Kettlety, T., J.P. Verdon, M.J. Werner, J-M. Kendall, J. Budge, (2019). Investigating the role of elastostatic stress transfer during hydraulic fracturing-induced fault reactivation: *Geophysical Journal International*, 217, 1200-1216.
- Kluesner, Jared & Brothers, Daniel. (2016). Seismic attribute detection of faults and fluid pathways within an active strike-slip shear zone: New insights from high-resolution 3D P-Cable™ seismic data along the Hosgri Fault, offshore California. *Interpretation*. 4. SB131-SB148. doi:10.1190/INT-2015-0143.1.

- Kurt J. Marfurt, (2015), "Techniques and best practices in multiattribute display," *Interpretation* 3: B1-B23.
- Ma, DB., Wu, GH., & Scarselli, N. (2019). Seismic damage zone and width–throw scaling along the strike-slip faults in the Ordovician carbonates in the Tarim Basin. *Pet. Sci.* 16, 752–762. <https://doi.org/10.1007/s12182-019-0352-4>
- Montgomery, C.T., Smith, M. B. (2010). Hydraulic Fracturing: History of an enduring technology. *NSI technologies*.
- Nash, K. M. (2010). Shale gas development (Ser. Energy science, engineering and technology). *Nova Science*.
- National Research Council (U.S.). (2013). Committee on Induced Seismicity Potential in Energy Technologies. Induced seismicity potential in energy technologies. *National Academy Press*.
- Norton, M., Hovdebo, W., Cho, D., Maxwell, S., & Jones, M. (2011). Integration of Surface seismic and microseismic for the characterization of a shale gas reservoir. Retrieved November 10, 2019, from <https://csegrecorder.com/articles/view/integration-of-surface-seismic-and-microseismic-for-shale-gas-reservoir>.
- Othman, A. A., Fathy, M., & Maher, A. (2016). Use of spectral decomposition technique for delineation of channels at Solar gas discovery, offshore West Nile Delta, Egypt. *Egyptian Journal of Petroleum*, 25(1), 45–51. doi: 10.1016/j.ejpe.2015.03.005.

- Perez, R., & Marfurt, K. (2013). Brittleness estimation from seismic measurements in unconventional reservoirs: Application to the Barnett Shale. *SEG Technical Program Expanded Abstracts 2013*. doi: 10.1190/segam2013-0006.1.
- Pico, A., Aboud, J., Parraga, F., Martinez, J., Lopez, G., & Pacific, R. (2014). Practical Analysis of Strike-Slip Faults Using Multi Attributes 3D seismic data: A case study in Eastern Colombia. 10.1190/segam2014-0871.1.
- Sena, A., Castillo, G., Chesser, K., Voisey, S., Estrada, J., Carcuz, J., Hodgkins, P. (2011). Seismic reservoir characterization in resource shale plays: Stress analysis and sweet spot discrimination. *The Leading Edge*, 30(7), 758–764. doi: 10.1190/1.3609090.
- Smith, N., Turner, P., & Williams, G. (2010). UK data and analysis for shale gas prospectivity. *Geological Society, London, Petroleum Geology Conference Series*, 7(1), 1087–1098. doi: 10.1144/0071087.
- Stephenson, B., Galan, E., Williams, W., Macdonald, J., Azad, A., Carduner, R., & Canada, S. (2018). Geometry and Failure Mechanisms from Microseismic in the Duvernay Shale to Explain Changes in Well Performance with Drilling Azimuth, 1–20.
- Tingdahl, K. & De Groot, P. (2003). Post-stack-dip- and azimuth processing. *Journal of Seismic Exploration*. 12. 113-126.
- Walsh, R., Zoback, M. D., Lele, S. P., Pais, D., Weingarten, M., & Tyrrell, T. (2018). FSP 2.0: A Program for Probabilistic Estimation of Fault Slip Potential Resulting from Fluid Injection. *Stanford University*.

- Weir, R. M., Eaton, D. W., Lines, L. R., Lawton, D. C., & Ekpo, E. (2018). Inversion and interpretation of seismic-derived rock properties in the Duvernay play. *Interpretation*, 6(2). doi: 10.1190/int-2017-0149.1.
- Wentworth, C. K. (1922). A scale of grade and class terms for clastic sediments. *The Journal of Geology*, 30(5), 377–392.
- Zalán, Pedro. (1987). Identification of strike-slip faults in Seismic section. *Society of Exploration Geophysicists*. 1987. doi:10.1190/1.1892142.
- Zendehboudi, S., & Bahadori, A. (2016). Shale oil and gas handbook: theory, technologies, and challenges. *Elsevier*.
- Zoback, M., & Kohli, A. (2019). Introduction in Unconventional Reservoir Geomechanics: Shale Gas, Tight Oil, and Induced Seismicity. Cambridge: *Cambridge University Press*. doi:10.1017/9781316091869.002.
- Zou, C. (2013). Unconventional petroleum geology (1st ed.). *Elsevier*. doi:10.1016/C2011-0-06250-6.